Technical Physics Letters, Vol. 27, No. 10, 2001, pp. 801–802. Translated from Pis'ma v Zhurnal Tekhnicheskoĭ Fiziki, Vol. 27, No. 19, 2001, pp. 1–4.

The Optical Characteristics of Laser-Erosion Silver Plasma

A. K. Shuaibov

Uzhgorod National University, Uzhgorod, Ukraine

e-mail: ishev@univ.uzhgorod.ua

Received April 14, 2001

Abstract—The near-threshold optical emission in the 220- to 600-nm wavelength range from laser-erosion silver plasma was studied. The plasma was generated by a pulsed laser radiation with $\lambda = 1.06$ μm and a beam power density of $(1–3) \times 10^8$ W cm^{-2} focused on the surface of a massive silver target. The main emission lines are due to the Ag(I) resonances with $\lambda = 328.1$ and 338.8 nm. A bottle-neck of the recombination flux populating the upper energy states of silver atoms in the $7d^2D_{5/2}$AgI level of Ag(I). The main flux of the recombination reaction $Ag^+ + 2e \longrightarrow Ag^* + e$ passes sequentially through the following levels of Ag(I): $7d \longrightarrow 6d \longrightarrow 5d \longrightarrow 5s$. The results can be used to increase the quality of thin silver films and to optimize the process of depositing films of complex compositions by laser erosion of the crystal targets of the AgGa(Al,In)S(Se)$_2$ type.

Silver is widely used in modern microelectronics in the form of thin metal films and is an important component of the polycrystalline compositions based on compounds of the AgGa(Al,In)S(Se)$_2$ type employed (as well as the CuInS(Se)$_2$ films [1]) in manufacturing solar cell elements by laser erosion. In order to obtain high-quality films of silver or multicomponent silver-containing compositions, it is important to select optimum parameters of the laser plasma. The emission spectra of multicomponent laser plasmas are rather complicated and still insufficiently studied, especially in the case of a near-threshold laser action upon the target [2, 3]. Solving this problem requires quantitative investigation of the optical characteristics of laser plasmas generated from individual components of the composite targets. The optical characteristics of the laser plasmas from Cu, Ga, and In targets were reported previously [4–6]. No such data were previously reported for the laser plasma of silver.

Reported below are the results of investigations of the laser-erosion silver plasma obtained with the aid of a YAG : Nd^{3+} laser operated at a power density of $(1–3) \times 10^8$ W cm^{-2} at the point of focusing and a laser pulse duration of 20 ns. The experimental method, instrumentation, and conditions were analogous to those used previously [4–6]. The plasma was generated by laser erosion of a massive target made of a special purity grade silver, mounted in a vacuum chamber with a residual air pressure of $P = 3–5$ Pa. The optical emission spectra were interpreted based on the published reference data [7–9].

The optical emission spectrum of a laser-erosion silver plasma is shown in the figure. The interpretation of this spectrum is presented in the table, where J/k_λ is the relative intensity of the emission lines, k_λ is the relative spectral sensitivity of a monochromator–photomultiplier system employed, and $\Delta J/k_\lambda$ is the ratio of the line intensity (with the continuous background subtracted) to the total intensity of all the registered spectral lines of silver. The review spectrum displayed only the spectral lines of atomic silver. The line emission from silver atoms in the laser plasma was observed on a weak continuous background (see the figure). The most intense emission lines corresponded to the Ag(I) resonances with $\lambda = 328.1$ and 338.3 nm. In the visible spectral range, the maximum intensity was observed for the spectral lines of Ag(I) with $\lambda = 520.9$ and 546.5 nm.

A considerable self-absorption of the Ag(I) resonance radiation makes it possible to perform diagnostics of the laser plasma of silver using well resolved and

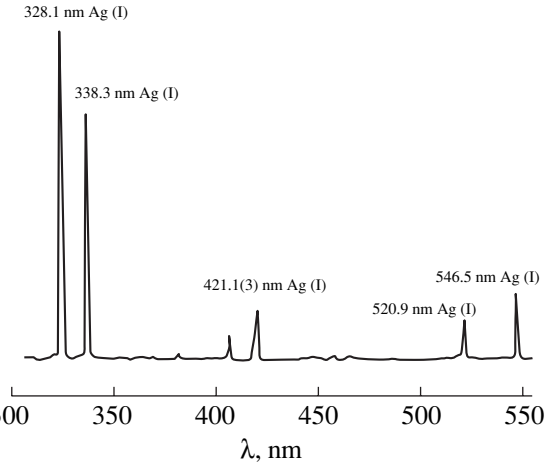

The optical emission spectrum of a laser erosion silver plasma measured from a point spaced by 1 mm from the target surface.

1063-7850/01/2710-0801$21.00

Optical emission intensity distribution in the spectrum of laser erosion silver plasma

λ, nm	Transition, Ag(I)	E_0, cm^{-1}	E_1, cm^{-1}	J/k_λ, a.u.	$\Delta J/k_\lambda$, %	Q, 10^{-18}, cm^2
328.1	$5s^2S_{1/2}$–$5p^2P_{3/2}$	0	30473	1.00	39	1020
338.3	$5s^2S_{1/2}$–$5p^2P_{3/2}$	0	29552	0.68	25	340
381.1	$5p^2P_{3/2}$–$7d^2D_{5/2}$	30473	56706	0.03	1	11.7
381.2	$5p^2P_{1/2}$–$7d^2D_{3/2}$	30473	56700			
405.5	$5p^2P_{1/2}$–$6d^2D_{3/2}$	29552	54203	0.07	3	5.8
421.1	$5p^2P_{3/2}$–$6d^2D_{5/2}$	30473	54214	0.15	6	9.2
421.3	$5p^2P_{3/2}$–$6d^2D_{3/2}$	30473	54203			
520.9	$5p^2P_{1/2}$–$5d^2D_{3/2}$	29552	48744	0.22	9	17.0
546.5	$5p^2P_{3/2}$–$5d^2D_{5/2}$	30473	48764	0.45	17	20.0

comparatively intense lines in the visible range. A comparison of the optical emission intensity distribution to the effective cross sections Q for the electron-impact excitation of Ag(I) [7] showed a lack of correlation. Similar to the case of the laser erosion plasmas of Al, Ga, and In [4–6], the most probable mechanism for population of the excited states in Ag(I) is the recombination reaction AgI ($Ag^+ + 2e \longrightarrow Ag^* + e$).

A bottle-neck of the recombination flux populating the upper energy states of silver atoms in the $7d^2D_{5/2}$ level of Ag(I). As can be seen from the table, the intensity of emission from Ag(I) gradually decreases with the energy of the upper excited state decreasing from the bottle-neck level to the resonance states of silver. Under the experimental conditions studied, the recombination flux passes sequentially through the following levels of Ag(I): $7d \longrightarrow 6d \longrightarrow 5d \longrightarrow 5s$.

Thus, it was demonstrated that the pulsed radiation of a neodymium laser with a power of $(1–3) \times 10^8$ W cm^{-2} acting upon a massive silver target in vacuum generates a silver plasma with the main contribution to the optical emission from the resonance Ag(I) lines. A bottle-neck of the recombination flux is the $7d^2D_{5/2}$ level of Ag(I) with an energy of $\varepsilon = 56706$ cm^{-1}. Diagnostics of the laser erosion silver plasma by emission spectroscopy can be performed using the visible spectral lines of Ag(I) atoms with $\lambda = 520.9$ and 546.5 nm.

Acknowledgments. The author is grateful to A.I. Dashchenko for his help in conducting experiments.

REFERENCES

1. N. Khare, G. Razzini, and P. Bicelli, Thin Solid Films **186**, 113 (1990).
2. B. K. Kotlyarchuk, D. I. Popovich, and V. Ya. Pentko, Zh. Tekh. Fiz. **57** (9), 1824 (1987) [Sov. Phys. Tech. Phys. **32**, 1091 (1987)].
3. I. E. Kacher, A. K. Shuaibov, A. I. Dashchenko, and M. Yu. Rigan, in *Abstracts of the V International Conference "Material Science and Material Properties for Infrared Optoelectronics", Kiev, Ukraine, 2000*, p. 103.
4. A. K. Shuaibov, A. I. Dashchenko, and I. V. Shevera, Pis'ma Zh. Tekh. Fiz. **26** (18), 57 (2000) [Tech. Phys. Lett. **26**, 832 (2000)].
5. A. K. Shuaibov, L. L. Shimon, A. J. Daschenko, and M. P. Chuchman, Uzh. Univ. Sci. Herald. Ser. Phys. **8** (2), 348 (2000).
6. A. K. Shuaibov, L. L. Shimon, A. I. Dashchenko, *et al.*, Fiz. Plazmy **27** (1), 85 (2001) [Plasma Phys. Rep. **27**, 82 (2001)].
7. A. Yu. Krasavin, A. N. Kuchenev, and Yu. M. Smirnov, Opt. Spektrosk. **54** (1), 20 (1983) [Opt. Spectrosc. **54**, 11 (1983)].
8. A. N. Zaĭdel', V. K. Prokof'ev, S. M. Raĭskiĭ, *et al.*, *Tables of Spectral Lines* (Nauka, Moscow, 1969; Plenum, New York, 1970).
9. Yu. M. Smirnov, Zh. Tekh. Fiz. **69** (2), 6 (1999) [Tech. Phys. **44**, 137 (1999)].

Translated by P. Pozdeev

Technical Physics Letters, Vol. 27, No. 10, 2001, pp. 803–805. Translated from Pis'ma v Zhurnal Tekhnicheskoĭ Fiziki, Vol. 27, No. 19, 2001, pp. 5–10.

Microwave Pulses Compressed in a Quasi-Optical Resonator with Corrugated Mirror

Yu. Yu. Danilov[a, *], S. V. Kuzikov[a], V. G. Pavel'ev[a], Yu. I. Koshurinov[a], and S. M. Leshchinsky[b]

[a] *Institute of Applied Physics, Russian Academy of Sciences, Nizhni Novgorod, Russia*
[b] *Nizhni Novgorod State University, Nizhni Novgorod, Russia*
**e-mail: danilov@appl.sci-nnov.ru*
Received April 5, 2001

Abstract—A microwave pulse compressor, representing a three-mirror resonator supplied with a radiation beam reflected from a corrugated mirror, was constructed and experimentally tested. A fivefold compression of microwave pulses with a 70% efficiency was obtained in a 9-mm wavelength range. © *2001 MAIK "Nauka/Interperiodica".*

Introduction. On going to a short microwave range in linear accelerators, limitations related to the microwave breakdown in the accelerating structure are removed and the use of accelerating electric fields reaching hundreds megaelectronvolts per meter becomes possible, which allows the accelerator length to be significantly reduced [1]. Using microwave pulse compressors makes the accelerator design cheaper as compared to the case when the pulsed power is supplied to the accelerating region directly from the chain of microwave amplifiers [1]. The most widely used means of compressing phase-modulated microwave pulses in accelerators is based on using ring-shaped resonators [2–4].

A decrease in the working wavelength, at a retained level of energy stored in a resonator and the same resonator size on the wavelength scale, is accompanied by an increase in the electric field strength in the resonator that may lead to the microwave breakdown development. Aimed at avoiding the microwave breakdown, an increase in the resonator volume leads to an increase in the ohmic losses in the resonator walls and results in broadening of the resonance curves of the intrinsic resonator modes. As a result, using closed resonators in the millimeter wave range becomes inexpedient and mirror resonators should be preferred.

A possible method of the mirror resonator coupling to the beam transport line is using a corrugated mirror (Fig. 1). The field over such a mirror represents the sum of waves diffracted in various orders. The corrugation period is selected so as to provide that, upon scattering from the corrugated mirror, only wave fluxes of the 0th and (–1)st orders for both the exciting wave and the intrinsic resonator mode would propagate far from this mirror. The wave flux of the (–1)st order is used for the resonator coupling to the beam transport line (Fig. 1).

Resonator design. Initial parameters for the microwave pulse compressor were taken close to the values characteristic of a prototype of the next-generation linear accelerator (with energies up to 5 TeV) [5]: frequency, ~34 GHz; input pulse duration, 80 ns; compression factor (input to output pulse duration ratio), 5. The main task in creating this compressor was to obtain a maximum compression efficiency (input to output pulsed energy ratio). According to the results of calculations, an acceptable compression efficiency level (70% or above) is reached with an external ≈70% of ~4000 and an intrinsic Q of not less than 50000.

Taking into account the above restrictions and the modeling results, we selected an equilateral three-mirror resonator scheme (Fig. 1) comprising two spherical mirrors and a flat mirror with a sinusoidal corrugation pattern on the surface. The resonator parameters are listed in the table. The working mode was a high-electric-strength mode with an electric field parallel to the corrugation groves.

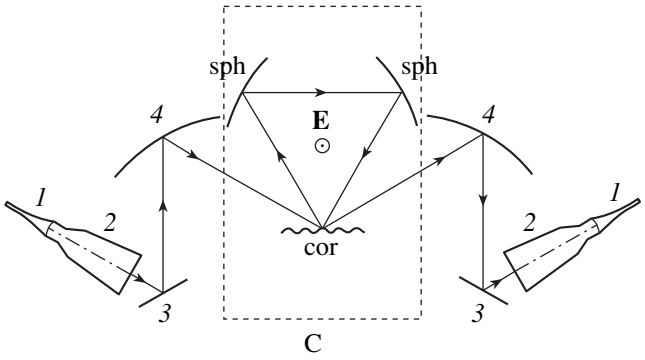

Fig. 1. Schematic diagram of the energy input/output scheme for a ring resonator (C) using two spherical mirrors (sph) and a corrugated mirror (cor).

1063-7850/01/2710-0803$21.00 © 2001 MAIK "Nauka/Interperiodica"

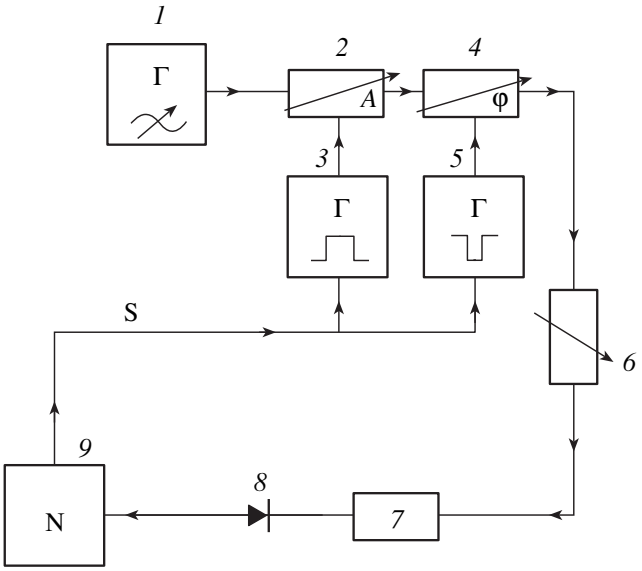

Fig. 2. Schematic diagram of the experimental setup. S is the synchronizing signal (for other notations see the text).

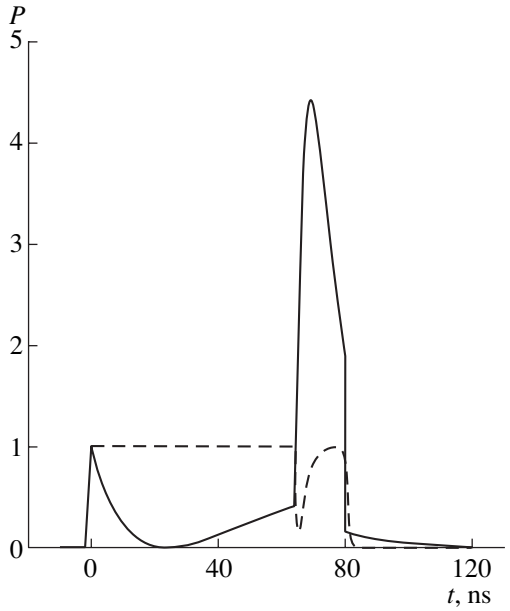

Fig. 3. Typical oscillograms of the (dashed) input and (solid) output microwave power pulses.

A system for the energy input from a microwave generator to the resonator was designed proceeding from a given diameter of the spot of intrinsic mode on the corrugated mirror surface. This scheme included (Fig. 1) junction *1* between a rectangular waveguide with the working wave H_{10} and a circular waveguide with the working wave H_{11}, horn *2* (consisting of expanding cone-shaped circular waveguide sections [6]) converting the H_{11} wave into a Gaussian beam, a cylindrical mirror *3*, and a spherical mirror *4*. The energy output scheme was identical to the input system (Fig. 1).

Experimental setup and results. Figure 2 shows a schematic diagram of the experimental setup including the following elements: (*1*) microwave generator; (*2*) electric-field-controlled amplitude modulator forming rectangular input microwave pulses; (*3*) supply pulse generator; (*4*) electrically controlled phase-rotating circuit with a characteristic 180° rotation time of 2 ns; (*5*) supply pulse generator; (*6*) high-precision attenuator; (*7*) mirror resonator with input/output system (Fig. 1); (*8*) detector; and (*9*) oscillograph.

Resonator parameters (||, in plane of Fig. 1; ⊥, in the perpendicular plane)

Spherical mirror size, mm	|| – 180, ⊥ – 196
Spherical mirror curvature radius, mm	1380
Corrugated mirror size, mm	|| – 181, ⊥ – 156
Corrugation period, mm	6.46
Corrugation height, mm	1.11
Distance between mirror centers, mm	296
Working frequency (experiment), GHz	33.96
Loaded *Q* (experiment)	3400
Intrinsic *Q* (experiment)	65000

Figure 3 shows typical oscillograms of the input and output pulses. For an input pulse duration of 80 ns and a fivefold pulse compression, the system showed a compression efficiency of ~70% and a power gain (a product of the compression factor by the efficiency) of ~3.5 (for an output pulse peak power of 4.4). These values agree well with the results of model calculations using the parameters taken from experimental data for the resonator. The oscillogram of the output pulse deviates from the calculated curve by no more than 5%.

Conclusion. The results of the experiment described above showed the possibility of compressing microwave pulses using the proposed quasi-optical resonator with an efficiency comparable to that of the best alternative schemes [2–4]. We believe that this compression method can be used in the wavelength range from 1 cm to 1 mm for supplying particle accelerators with the energies of up to ~1 TeV and above.

Acknowledgments. The authors are grateful to M.I. Petelin for his permanent interest in this study.

This work was supported by the Russian Foundation for Basic Research (project nos. 96-02-17779 and

99-02-17781) and by the International Science Foundation (grant nos. NOT000 and NOT300).

REFERENCES

1. A. N. Lebedev and É. A. Perel'shteĭn, in *Relativistic High-Frequency Electronics*, Ed. by A. V. Gaponov-Grekhov (Inst. Prikl. Fiz. Akad. Nauk SSSR, Gorki, 1990), Vol. 6, pp. 217–255.
2. Z. D. Farcas, H. A. Hogg, G. A. Loew, and P. B. Wilson, in *Proceedings of the 9th Conference on High Energy Accelerator, SLAC, Stanford, 1974*, p. 576.
3. V. E. Balakin and I. V. Syrachev, in *Proceedings of the III European Particle Accelerator Conference, Berlin, 1992*, p. 1173.
4. Yu. Yu. Danilov, S. V. Kuzikov, V. G. Pavel'ev, and Yu. I. Koshurinov, Pis'ma Zh. Tekh. Fiz. **27** (6), 59 (2001) [Tech. Phys. Lett. **27**, 245 (2001)].
5. P. B. Wilson, SLAC-PUB-7944 (April 1997).
6. G. G. Denisov and S. V. Kuzikov, in *Conference Digest of 20th International Conference on Infrared and Millimeter Waves, Orlando, 1995*, p. 297.

Translated by P. Pozdeev

Technical Physics Letters, Vol. 27, No. 10, 2001, pp. 806–809. Translated from Pis'ma v Zhurnal Tekhnicheskoĭ Fiziki, Vol. 27, No. 19, 2001, pp. 11–18.

The Effect of Fullerene C_{60} on the Thermooxidative Degradation of a Free-Radical PMMA Studied by Thermogravimetry and Calorimetry

B. M. Ginzburg[a], V. L. Ugolkov[a], L. A. Shibaev[a], and V. P. Bulatov[b]

[a] *Institute of Machine Science, Russian Academy of Sciences, St. Petersburg, Russia*

[b] *Institute of Macromolecular Compounds, Russian Academy of Sciences, St. Petersburg, 194021 Russia*

Received April 18, 2001

Abstract—Thermogravimetric and calorimetric study of the effect of fullerene C_{60} on the thermooxidative degradation of free-radical poly(methyl methacrylate) revealed three stages in the process. © *2001 MAIK "Nauka/Interperiodica".*

Previously [1], we studied the role of weak bonds in the thermal degradation of free-radical poly(methyl methacrylate) (PMMA) by differential thermogravimetry (DTG) technique. Heating a sample in N_2 was accompanied by three peaks in the thermogram (Fig. 1a, curve *1*): peak I (~165°C) was attributed to the degradation initiated by the chain defects of the head-to-head type (H–H bonds); peak II (~270°C) was assigned to the degradation caused by the unsaturated terminal groups; the most intense peak III (~360°C) was explained by the random degradation of the PMMA backbone. Then we studied the effect of C_{60} on the process of thermal degradation in the free-radical PMMA by mass-spectrometric thermal analysis (MTA) in vacuum [2]. The MTA curve of the pure PMMA sample also displayed three peaks at approximately the same temperatures (Fig. 1b, curve *1*). After adding a small amount of C_{60}, peak I disappeared and peak II significantly decreased in intensity (Fig. 1b, curve *2*), from which we concluded that fullerene C_{60} acts as a trap of free radicals formed as a result of PMMA degradation in the regions of peaks I and II. At the same time, the intensity of peak III increased in the presence of C_{60} and shifted by ~15 K toward higher temperatures. Therefore, the fullerene inhibits the degradation of free-radical PMMA at both low and high temperatures.

There is one circumstance that was previously not interpreted. The widths of peaks I and II (related to the rupture of weak bonds by a certain mechanism) were significantly smaller than the width of peak III determined by the random breakage of intramolecular bonds. The introduction of fullerene also reduced the width of MTA peaks (Fig. 1b). Apparently, the spectrum of degradation pathways became narrower, being determined by the PMMA degradation products attached to C_{60}. Numerical estimates of the ratio of the amounts of C_{60} molecules and PMMA radicals showed approximately equal amounts of PMMA molecules (with a given molecular mass) and C_{60} (at a 1% initial concentration) per unit sample mass. Since each C_{60} molecule can attach at least six radicals, the initial amount of C_{60} was sufficient for tapping all PMMA radicals formed in the system. However, this does not actually take place. Estimates of the relative areas under the MTA peaks before introducing C_{60} (Fig. 1) gave $S_I = 0.10$, $S_{II} = 0.30$, and $S_{III} = 0.60$ in agreement with the DTG data [1]. Therefore, the fraction of degradation products due to the weak bond rupture amounts to ~0.40. Analogous data determined upon the introduction of C_{60} allowed us to estimate the fraction of PMMA molecules trapped by the fullerene as $S_{Fu} = S_I + (S_{II} - S'_{II})$, where S'_{II} is the fraction of peak II after C_{60} introduction. It was found that $S_{Fu} \approx 0.20$, which implies that only ~20% of the C_{60} molecules trapped the pairs of PMMA radicals formed upon chain breakage or 40% of the C_{60} molecules trapped one such radical. It seems that the true fraction of bound fullerene molecules is closer to 20%, since the ends of two radicals formed upon the PMMA chain breakage are localized virtually at one point and both these radicals are more probably attached to the same C_{60} molecule, should such a molecule appear at the site. The remaining 80% of the fullerene are free. This result is important for the adequate interpretation of experimental data, indicating that the system contains the C_{60} molecules of at least two types, bound and not bound to PMMA.

A process no less interesting, especially from the standpoint of applications, is offered by the thermooxidative degradation of PMMA in air. In the presence of

oxygen (similar to the case of fullerene), peak I disappears (Fig. 1a, curve *2*) and a new intense peak D appears instead at ~300°C (between peaks II and III) [1]. Therefore, oxygen (unlike C_{60}) plays a twofold role increasing stability of the system at lower temperatures and promoting degradation at higher temperatures [1].

It is naturally suggested that the manifestations of chain degradation observed by DTG and MTA may be accompanied by thermal effects. In particular, the thermooxidative degradation taking place in an open system must involve at least three components: (i) endothermal process of chain breakage, (ii) exothermal oxidation of chains and thermal degradation products, and (iii) endothermal process of sublimation or evaporation of the degradation products. The purpose of this work was to study the effect of C_{60} on the thermooxidative degradation of free-radical PMMA using a combination of thermogravimetric analysis (TGA) and differential scanning calorimetry (DSC).

The experiments were performed with fullerene C_{60} (99.7%) and powdered free-radical PMMA with a molecular mass of 8.5×10^4. Fullerene C_{60} and PMMA were separately dissolved in toluene and these solutions were poured together in proportions selected so as to provide a desired C_{60}/PMMA ratio (1 or 10%). The samples were prepared by casting films from solutions. The thermal decomposition was studied on an STA 429 thermal analyzer (Netzsch, Germany) by heating the samples in air at a rate of 5 K/min and measuring variations of the temperature and mass and the thermal effects. The sample weight was 5 mg.

For all C_{60}-containing samples, the curve of the weight loss is ~30–60°C higher as compared to that for pure PMMA (Fig. 2). This result indicates that C_{60} also plays a stabilizing role with respect to the thermooxidative degradation of free-radical PMMA. Simultaneously measured DTG curves (not depicted in Fig. 2) showed a significant narrowing of the peaks (~1.5 times) upon the fullerene introduction into PMMA, which is explained by the PMMA radical attachment to C_{60} leading to a decrease in the set of possible reactions in the course of subsequent degradation.

All DSC thermograms (Fig. 2) exhibit an endothermal peak, the intensity of which decreases with increasing fullerene content. A joint analysis of the TGA and DSC data suggests a following scheme of the process of thermooxidative degradation of free-radical PMMA, which can be conditionally subdivided into three stages. In the first stage (preceding the endothermal peak), pure PMMA features oxidation of the degradation products formed as a result of the chain breakage at the weak binding sites. In this stage, the system loses only ~28% of the initial mass (which is much smaller as compared to ~40% of the total mass lost in the first two peaks). From this we infer that either not all of the degradation products were oxidized or not all of them could leave the system. Nevertheless, this stage is characterized by evolution of the major part (~90%) of thermal energy. The introduction of fullerene leads to a decrease in the yield of degradation products in the first stage (to ~15 and 23% upon adding 1 and 10% C_{60}, respectively).

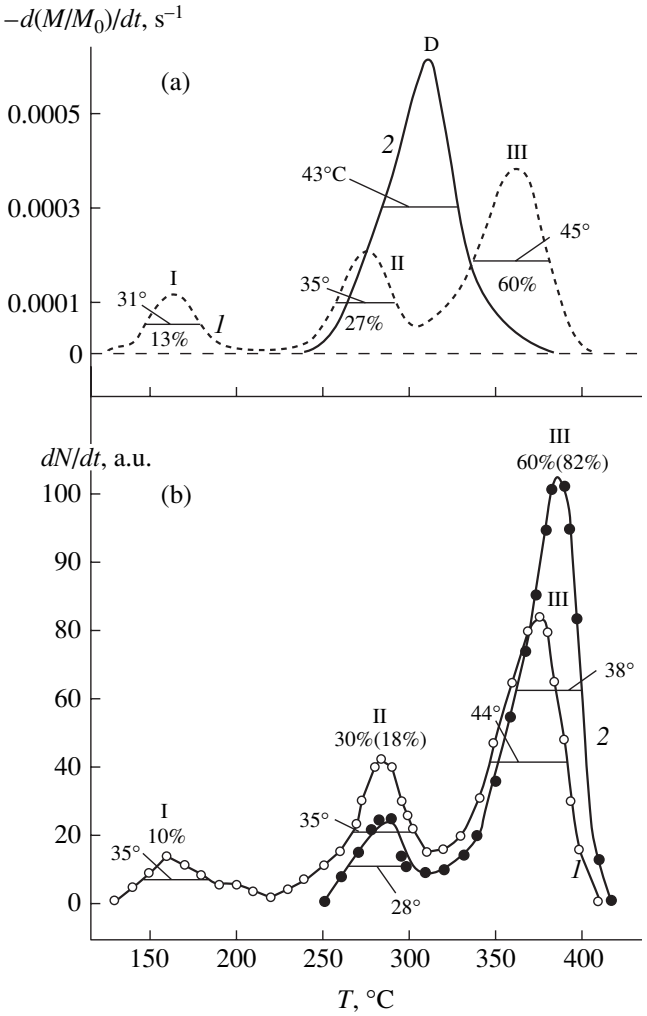

Fig. 1. Temperature variation of the yield of thermal degradation products from free-radial PMMA [1]. Figures at the peaks indicate their relative areas before and (in parentheses) after adding C_{60}, as well as half-widths: (a) DTG thermograms showing the rate of weight loss $d(\Delta M/M_0)/dt$ on heating in (*1*) N_2 and (*2*) in air; (b) MTA thermograms showing the rate of monomer yield dN/dt (*1*) from pure PMMA and (*2*) from a PMMA–C_{60} mixture [2].

Apparently, the effect of C_{60} upon the thermooxidative degradation of free-radical PMMA may proceed by two pathways. The first involves the attachment of PMMA radicals to C_{60} molecules, whereby fullerene competes with oxygen and partly displaces this oxidizing agent from reaction with PMMA (effectively shifting the degradation of products toward higher temperatures—to the third stage). The second pathway is related to a possible direct interaction of C_{60} with oxygen, which leads to a deficit in oxygen for the PMMA

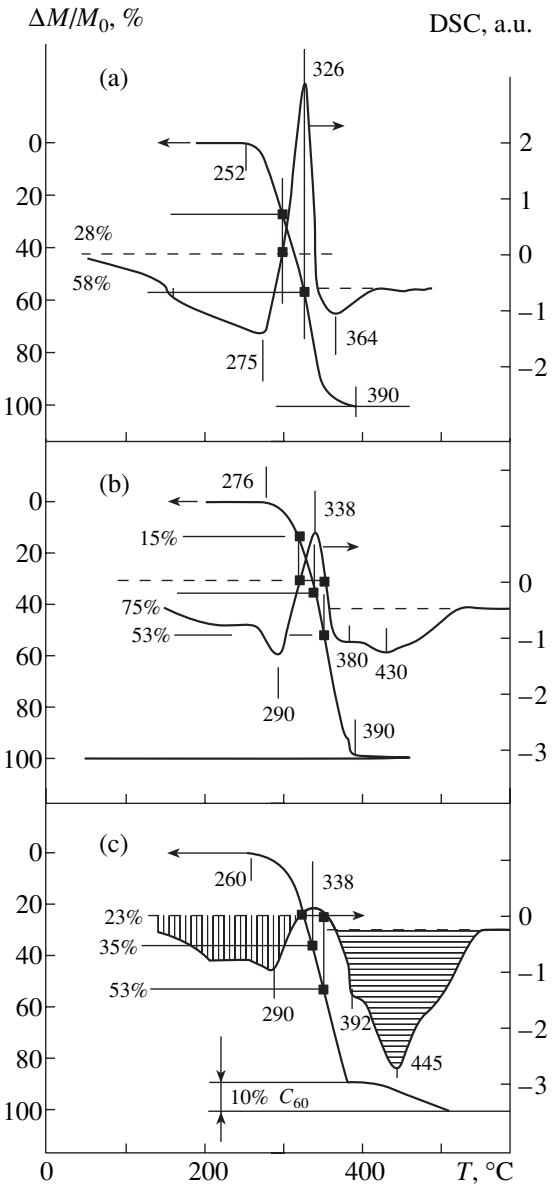

Fig. 2. Thermooxidative degradation of free-radical PMMA in air studied by TGA ($\Delta M/M_0$ is the relative sample mass variation) and DSC (thermal flux): (a) pure PMMA; (b) PMMA + 1% C_{60}; (c) PMMA + 10% C_{60}. Dashed lines indicate the base level. Figures at the curves indicate the values of temperature characterizing the PMMA degradation process.

oxidation and to the yield of unoxidized products of thermooxidative degradation of PMMA from the system. Probably, the second mechanism accounts for the fact that an increase in the C_{60} concentration from 1 to 10% is accompanied by some growth in the yield of the PMMA degradation products in the first stage. Note that the temperature corresponding to the onset of the thermooxidative degradation is somewhat decreases on the passage from 1 to 10% C_{60}. The introduction of C_{60} is accompanied by a decrease in the amount of heat liberated in the corresponding weight loss peaks (the areas of exothermal peaks in Figs. 2b and 2c decrease 1.2 and 1.5 times, respectively).

This behavior is consistent with the hypothesis that C_{60} prevents the oxidation of polymer by attaching PMMA radicals and competitively displacing oxygen. For a rough estimate, let us assume that ~20% of PMMA is oxidized in the first stage upon the introduction of C_{60}. This amounts to half of the total weight loss corresponding to peaks I and II. The other half is apparently attached to fullerene. This estimate agrees with the above value obtained from the MTA data for the polymer fraction trapped by fullerene. It should be emphasized that the beginning of exothermal processes is detected in most cases much earlier than the onset of the corresponding weight loss. Thus, a latent degradation takes place, whereby the PMMA chain is broken but the C_{60} molecules bound to the degradation products keep them from leaving the system.

In the second stage (from beginning to peak of the endothermicity), the degradation products are volatilized with the heat uptake. These products may include both the unoxidized degradation products and the fragments of chains or radicals oxidized previously and exhibiting subsequent degradation without additional oxidation. In the case of pure PMMA, the fraction of these products amounts to ~30% of the total sample mass, while adding fullerene decreases this fraction to ~20% (for 1% C_{60}) and ~12% (for 10% C_{60}), which is also an evidence of the "holding" effect of C_{60}. A decrease in intensity of the endothermal peak with increasing C_{60} content indicates that a total heat of the chain degradation and the degradation product sublimation significantly decreases upon the introduction of fullerene.

The third oxidation stage (past the endothermal peak) in pure PMMA begins at ~326°C. Here, C_{60} prevents the bound products from oxidation up to ~ 338°C (Figs. 2b and 2c) but their subsequent degradation is accompanied by the evolution of a greater amount of heat as compared to that in pure PMMA. This heat is liberated in two steps, which corresponds to the peaks at 380 and 430°C (for 1% C_{60}) and 392 and 445°C (for 10% C_{60}). These peaks can naturally be attributed to the oxidation of fullerene, since the accompanying weight losses corresponds with a high precision to the amounts of fullerene introduced into PMMA. The presence of two peaks in the DSC thermograms agrees with the fact that there are two types of C_{60} molecules—bound and not bound to PMMA. Past the endothermal peak, the sample containing 1% C_{60} liberates the amount of heat ~5 times that evolved from pure PMMA. On the other hand, the amount of heat evolved from the sample containing 10% C_{60} increases only by a factor of ~3.3, which indicates that not less that half of C_{60} molecules is volatilized without oxidation.

The evolution of heat and the weight losses during the oxidative degradation of pure C_{60} take place at temperatures (~570°C) much higher as compared to those observed for C_{60} in the PMMA matrix. Evidently, not only does C_{60} affect the behavior of PMMA, but the polymer also influences the thermal properties of fullerene as well, which was also observed previously [3, 4].

REFERENCES

1. T. Kashiwagi, A. Inaba, J. E. Brown, *et al.*, Macromolecules **19** (8), 2160 (1986).
2. L. A. Shibaev, T. A. Antonova, L. V. Vinogradova, *et al.*, Pis'ma Zh. Tekh. Fiz. **23** (18), 81 (1997) [Tech. Phys. Lett. **23**, 730 (1997)].
3. A. O. Pozdnyakov, O. F. Pozdnyakov, B. P. Redkov, *et al.*, Pis'ma Zh. Tekh. Fiz. **22** (18), 57 (1996) [Tech. Phys. Lett. **22**, 759 (1996)].
4. A. O. Pozdnyakov, B. M. Ginzburg, O. F. Pozdnyakov, and B. P. Redkov, Zh. Prikl. Khim. (St. Petersburg) **73** (1), 134 (2000).

Translated by P. Pozdeev

Technical Physics Letters, Vol. 27, No. 10, 2001, pp. 810–812. Translated from Pis'ma v Zhurnal Tekhnicheskoĭ Fiziki, Vol. 27, No. 19, 2001, pp. 19–24.

General Equations with Small Parameter for the Theory of Current Synthesis on Arbitrary Nonclosed Surfaces

S. I. Éminov

Novgorod State University, Novgorod, 173003 Russia

e-mail: vav@novsu.ac.ru

Received April 11, 2001

Abstract—The inverse problem of restoring the space of currents on an arbitrary perfectly conducting surface is solved in the most general form. General equations with small parameter describing the synthesis of currents on arbitrary unclosed surfaces are derived. © *2001 MAIK "Nauka/Interperiodica".*

Formulation of the problem. Consider a perfectly conducting finite surface S coinciding with part of the coordinate surface in an orthogonal curvilinear coordinate system. Denote the surface current density by

$$\mathbf{j}(q_1, q_2) = \mathbf{t}_1 j_1(q_1, q_2) + \mathbf{t}_2 j_2(q_1, q_2), \quad (1)$$

where $\mathbf{t}_1$ and $\mathbf{t}_2$ are the unit vectors of coordinate lines.

A relation between the radiation pattern $\mathbf{F}$ and the current $\mathbf{j}$ is given by the expressions

$$F_\theta(\theta, \varphi) = \mathbf{i}_\theta \iint_S \mathbf{j} \exp(ik\rho\cos(\gamma))dS, \quad (2)$$

$$F_\varphi(\theta, \varphi) = \mathbf{i}_\varphi \iint_S \mathbf{j} \exp(ik\rho\cos(\gamma))dS, \quad (3)$$

where $\mathbf{i}_\theta$ and $\mathbf{i}_\varphi$ are the unit vectors of the spherical coordinate system (r, θ, φ) at the observation point, ρ is the distance between the origin and the radiation point on surface S, and γ is the angle between straight lines drawn from the origin to the observation and radiation points.

If the radiation pattern is known, relationships (2) and (3) form a system of integral equations for an unknown current:

$$\begin{cases} K_{11}j_1 + K_{12}j_2 = F_\theta, \\ K_{21}j_1 + K_{22}j_2 = F_\varphi, \end{cases} \quad (4)$$

where

$$K_{11}j_1 = \iint_S j_1(\mathbf{i}_\theta \cdot \mathbf{t}_1)\exp(ik\rho\cos(\gamma))dS,$$

$$K_{12}j_2 = \iint_S j_2(\mathbf{i}_\theta \cdot \mathbf{t}_2)\exp(ik\rho\cos(\gamma))dS,$$

$$K_{21}j_1 = \iint_S j_1(\mathbf{i}_\varphi \cdot \mathbf{t}_1)\exp(ik\rho\cos(\gamma))dS,$$

$$K_{22}j_2 = \iint_S j_2(\mathbf{i}_\varphi \cdot \mathbf{t}_2)\exp(ik\rho\cos(\gamma))dS.$$

The purpose of this study was to develop solution methods for system (4). Previous results [1] are extended here to the case of arbitrary surfaces.

Variational problem reduced to an operator equation. Let us introduce spaces required for the analysis. The vector pattern $\mathbf{F}(F_\theta, F_\varphi)$ belongs to a direct sum of spaces L_2. Components j_n $(n = 1, 2)$ of the surface current belong to the Hilbert spaces H_n. The current density $\mathbf{j}$ belongs to a direct sum of these spaces, $\mathbf{j} \in H = H_1 \oplus H_2$. Assume that the space H can be specified by a positive symmetric operator A, which will be defined below.

Taking into account above definitions, we can rewrite system (4) representing the initial synthesis equations as a single operator equation

$$K\mathbf{j} = \mathbf{F}, \quad (5)$$

where

$$K = \begin{pmatrix} K_{11} & K_{12} \\ K_{21} & K_{22} \end{pmatrix}.$$

Since not every specified pattern $\mathbf{F}$ is realizable, we will seek a current $\mathbf{j}$ that simultaneously forms a pattern close to the specified one and has a minimum possible norm. In other words, we minimize the functional

$$N(\mathbf{j}) = \alpha[\mathbf{j}]^2 + (K\mathbf{j} - \mathbf{F}, K\mathbf{j} - \mathbf{F}), \quad (6)$$

where α is a small parameter, $(\cdot, \cdot)$ is the inner product in space $L_2 \oplus L_2$, and $[\cdot, \cdot]$ is the inner product in space H. The following theorem is valid.

Theorem 1. The functional $N(\mathbf{j})$ reaches a maximum on solutions to the equation

$$\alpha A\mathbf{j} + K^*K\mathbf{j} = K^*\mathbf{F}, \tag{7}$$

where K^* is the adjoint operator defined by the formula

$$K^* = \begin{pmatrix} K_{11}^* & K_{21}^* \\ K_{12}^* & K_{22}^* \end{pmatrix}$$

acting from the space $L_2 \oplus L_2$ of radiation patterns to the space H of surface currents.

Proof. Let $\mathbf{j}$ be a solution to Eq. (7) and $\mathbf{h}$ be an arbitrary element in space H. Consider the difference

$$\begin{aligned} N(\mathbf{j}+\mathbf{h}) - N(\mathbf{j}) &= \alpha[\mathbf{j}+\mathbf{h}, \mathbf{j}+\mathbf{h}] \\ &+ (K\mathbf{j} + K\mathbf{h} - \mathbf{F}, K\mathbf{j} + K\mathbf{h} - \mathbf{F}) \\ &- \alpha[\mathbf{j}, \mathbf{j}] - (K\mathbf{j} - \mathbf{F}, K\mathbf{j} - \mathbf{F}) \end{aligned} \tag{8}$$

that can be transformed, with account of the definition of adjoint operator, to

$$\begin{aligned} N(\mathbf{j}+\mathbf{h}) - N(\mathbf{j}) &= \alpha[\mathbf{h}, \mathbf{h}] + (K\mathbf{h}, K\mathbf{h}) \\ &+ (\mathbf{h}, \alpha A\mathbf{j} + K^*K\mathbf{j} - K^*\mathbf{F}) \\ &+ (\alpha A\mathbf{j} + K^*K\mathbf{j} - K^*\mathbf{F}, \mathbf{h}). \end{aligned} \tag{9}$$

Taking into account that the current satisfies Eq. (7), we obtain from (9) that

$$N(\mathbf{j}+\mathbf{h}) = N(\mathbf{j}) + \alpha[\mathbf{h}]^2 + (K\mathbf{h}, K\mathbf{h}). \tag{10}$$

Since the second and third terms in (10) are nonnegative quantities, the functional $N(\mathbf{j})$ reaches maximum on a solution to Eq. (7). The theorem is proven.

Multiplying both sides of Eq. (7) by A^{-1}, we obtain

$$\alpha\mathbf{j} + A^{-1}K^*K\mathbf{j} = A^{-1}K^*\mathbf{F}. \tag{11}$$

Since

$$\begin{aligned} [A^{-1}K^*K\mathbf{j}, \mathbf{j}] &= (AA^{-1}K^*K\mathbf{j}, \mathbf{j}) \\ &= (K^*K\mathbf{j}, \mathbf{j}) = (K\mathbf{j}, K\mathbf{j}), \end{aligned}$$

Eq. (11) is the Fredholm equation of the second kind with positive operator. As a result, the following theorem is valid.

Theorem 2. For an arbitrary pattern $\mathbf{F}$, Eqs. (11) and (7) have a unique solution $\mathbf{j}$ minimizing the functional $N(\mathbf{j})$.

Note that the theory of second-kind Fredholm equations with small parameter is developed in sufficient detail. Results of this theory can be applied to Eqs. (11) and (7). There are two important propositions [2].

Proposition 1. For any $\varepsilon > 0$ and an arbitrary pattern $\mathbf{F}$, there exists a unique current $\mathbf{j}_0$ from the class

$$[\mathbf{j}]^2 \le \varepsilon$$

which minimizes the functional

$$P(\mathbf{j}) = (K\mathbf{j} - \mathbf{F}, K\mathbf{j} - \mathbf{F}),$$

and thus creates a radiation pattern closest to the specified one.

Proposition 2. For any $\varepsilon > 0$ and an arbitrary pattern $\mathbf{F}$, there exists a unique current $\mathbf{j}_0$ from the class of currents satisfying the condition

$$P(\mathbf{j}) \le \varepsilon$$

that has the minimum norm.

These propositions can readily be proved using the results obtained in [2]. Thus, an arbitrary pattern $\mathbf{F}$ can be approached to with in any prescribed accuracy; there exists a unique current with minimum norm that ensures the approximation of the specified pattern; this current can be found from Eq. (7).

Analysis equation and the space of currents. It only remains to choose the space of currents. This can be done using two methods. According to the first method, the space is chosen from the condition of a limited field in the near zone [1]. However, the space of currents can also be determined from the analysis equation. Both approaches were found to yield identical results. Below, we use the second approach.

The analysis equation has the form [3]

$$\begin{aligned} &\left[\operatorname{grad}_P \iint_S \left(\operatorname{grad}_Q \frac{\exp(-ikR)}{4\pi R}, \mathbf{j}\right) dS \right. \\ &\left. - k^2 \iint_S \mathbf{j} \frac{\exp(-ikR)}{4\pi R} dS, \mathbf{n}\right] = i\omega\varepsilon[\mathbf{E}^0, \mathbf{n}], \end{aligned} \tag{12}$$

where $\mathbf{E}^0$ is the primary electric field, $\mathbf{n}$ is the normal to the surface S, R is the distance from the radiation point Q to the observation point P, ω is the circular frequency, and ε is the absolute permittivity of medium.

Upon the analysis of Eq. (12), we can express the main singular operator in the form

$$\begin{aligned} A\mathbf{j} &= -\operatorname{grad}_\tau, \operatorname{div} \iint_S \mathbf{j} \frac{\exp(-R)}{R} dS \\ &+ \mathbf{t}_1 \iint_S j_1 \frac{\exp(-R)}{R} dS + \mathbf{t}_2 \iint_S j_2 \frac{\exp(-R)}{R} dS. \end{aligned} \tag{13}$$

Here, the subscript τ denotes the tangent component.

Theorem 3. The operator A is symmetric and positive.

Proof. Let us prove first that the second term in (13),

$$A_1 j_1 = \iint_S j_1 \frac{\exp(-R)}{R} dS, \tag{14}$$

is a symmetric and positive operator. For this purpose, we use the well-known Fourier integral expansion of the Green function:

$$\frac{\exp(-R)}{R} = \frac{1}{2\pi^3}$$

$$\times \iiint_{R^3} \frac{\exp[-i\chi_1(x-x') - i\chi_2(y-y') - i\chi_3(z-z')]}{\chi_1^2 + \chi_2^2 + \chi_3^2} \quad (15)$$

$$\times d\chi_1 d\chi_2 d\chi_3,$$

where $x = x(q_1, q_2)$, $y = y(q_1, q_2)$, and $z = z(q_1, q_2)$ are the coordinates of the observation point located on the surface S and $x' = x'(q_1', q_2')$, $y' = y'(q_1', q_2')$, and $z' = z'(q_1', q_2')$ are the coordinates of the radiation point on the surface S.

From (14) and (15), we obtain

$$(A_1 j_1, j_1) = \frac{1}{2\pi^3} \iiint_{R^3} \frac{|\tilde{j}_1|^2}{\chi_1^2 + \chi_2^2 + \chi_3^2} d\chi_1 d\chi_2 d\chi_3, \quad (16)$$

where

$$\tilde{j}_1 = \iint_S j_1 (i\chi_1 x' + i\chi_2 y' + i\chi_3 z') dS.$$

Formula (16) shows that the second operator in (13) is positive and symmetric.

The first term in (13) is, generally, an unbounded operator. Therefore, we should consider this operator on a dense set of functions vanishing at the boundary. Performing integration by parts and using representation (15) for the Green function, we can prove that this operator is symmetric and positive. Therefore, the whole operator (13) is symmetric and positive. The theorem is proven.

Synthesis equation with small parameter. Thus, we have derived a new equation with small parameter:

$$\alpha A\mathbf{j} + K^*K\mathbf{j} = K^*\mathbf{F}, \quad (17)$$

where the integrodifferential operator A is given by the formula

$$A\mathbf{j} = -\mathrm{grad}_\tau \mathrm{div} \iint_S \mathbf{j} \frac{\exp(-R)}{R} dS$$

$$+ \mathbf{t}_1 \iint_S j_1 \frac{\exp(-R)}{R} dS + \mathbf{t}_2 \iint_S j_2 \frac{\exp(-R)}{R} dS.$$

The operator A is symmetric and positive. The current $\mathbf{j}$ determined from (17) is an element of the energy space of operator A. The current demonstrates a correct behavior near the surface edge, because the operator A contains the information on the properties of the surface current.

REFERENCES

1. S. I. Éminov, Pis'ma Zh. Tekh. Fiz. **26** (14), 97 (2000) [Tech. Phys. Lett. **26**, 637 (2000)].
2. L. A. Sakhnovich, Usp. Mat. Nauk **35** (4), 69 (1980).
3. A. G. Davydov, E. V. Zakharov, and Yu. V. Pimnov, Dokl. Akad. Nauk SSSR **276** (1), 96 (1984) [Sov. Phys. Dokl. **29**, 380 (1984)].

Translated by A. Kondrat'ev

Technical Physics Letters, Vol. 27, No. 10, 2001, pp. 813–815. Translated from Pis'ma v Zhurnal Tekhnicheskoĭ Fiziki, Vol. 27, No. 19, 2001, pp. 25–31.

Styrene Vapor Decomposition in Air under the Action of a Pulsed Electron Beam

G. A. Mesyats, Yu. N. Novoselov, and I. E. Filatov

Institute of Electrophysics, Ural Division, Russian Academy of Sciences, Yekaterinburg, Russia

e-mail: nov@iep.uran.ru

Received June 24, 2001

Abstract—The results of experiments on the removal of styrene vapors from air with the aid of nanosecond electron beam pulses and a non-self-sustained volume discharge are reported. The macrokinetic equations based on these results allow the experimental data to be systematized and extrapolated beyond the range of vapor concentrations and deposited energies studied. © *2001 MAIK "Nauka/Interperiodica".*

Contamination of the air with styrene vapors takes place in the production of related plastics and during the fabrication of articles from these materials. In the case of a low concentration of styrene vapors, their removal from air by traditional chemical methods (e.g., catalytical burning) is not very effective. In such cases, methods employing electron beams and various electric discharges may be advantageous [1].

For example, it was demonstrated (see, e.g., [2, 3]) that styrene vapors can be removed from air with the aid of a pulsed discharge of the streamer crown type, but this process was characterized by a relatively high energy consumption. Recently [4], it was found that the use of electron beams allows organic impurities (in particular, acrolein vapors) to be removed at the expense of lower deposited energies. Below, we present the results of experiments on the removal of styrene vapors from air with the aid of a pulsed electron beam and a non-self-sustained volume discharge.

The experiments were performed in a setup analogous to that described previously [4], based on a nanosecond-pulsed electron accelerator. The accelerator produced a beam of electrons with the following parameters: energy, 180 keV; total current, 800 A; input cross section, 1 cm^2; pulse duration, 5 ns; pulse repetition rate, 10 s^{-1}. The irradiated gas volume with a length of 1 cm and a volume of 4 cm^3 was confined between a grid electrode (through which the electron beam was injected into the gas flow) and a continuous metal electrode connected to a capacitor bank with a total capacitance of 13 nF charged to a voltage variable from 0 to 10 kV. The energy deposited by the electron beam in the irradiated gas volume was 4.2×10^{-3} J per pulse, as determined by a standard method employing film dose monitors. Under non-self-sustained discharge conditions, the energy supplied from the capacitor bank was also taken into account.

A ventilator mounted in the working chamber (with a total volume of 3 dm^3) created a gas flow (at an average velocity of 0.5 m/s) through the irradiated discharge gap. This experimental scheme allowed a multistep purification process to be modeled, in which the gas flow was subjected to repeated irradiation cycles. In addition, averaging of the vapor concentration in the air increased the reproducibility of the results and reduced the error of determination of the concentration of volatile organic compounds. The experiments were performed with model nitrogen–oxygen mixtures (N_2–O_2, 80 : 20) at atmospheric pressure and room temperature, which the concentration of styrene vapors was varied from 50 to 1000 ppm.

The flowing gas mixture was treated by series of 1500 pulses. The organic impurity concentration was measured in a gas sample taken after each series. The samples were analyzed for styrene and its conversion products by gas chromatography [5]. The error of determination of the impurity concentration did not exceed 5% in the 100- to 1000-ppm range and 12% in the 10- to 100-ppm range. The results were expressed by the total amount of removed molecules $\Delta C = C_0 - C$ per unit volume [cm^{-3}], the degree of the gas purification from impurity $\eta = \Delta C/C_0$, and the energy consumed per one styrene molecule removed $\varepsilon = (W_b + W_d)/(e\Delta C)$ [eV/molecule] (C_0 and C are the initial and current impurity concentrations, respectively; W_b and W_d are the energies deposited in the gas phase by the pulsed electron beam and by the volume discharge, respectively; and e is the electron charge).

Variation of the impurity concentration C with the number of electron beam pulses is described by characteristic descending curves analogous to those reported in [3] for the streamer crown discharge. In the region of small impurity concentrations (from 50 to ~300 ppm), variation of the C value obeys the exponential law. The same character of variation of the current impurity con-

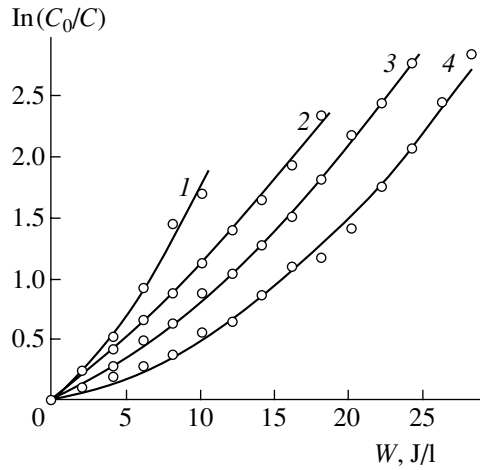

Fig. 1. The plots of $\ln(C_0/C)$ versus specific energy W deposited in the gas for various initial impurity (styrene) concentrations C_0 = 75 (*1*); 310 (*2*); 460 (*3*); 520 ppm (*4*).

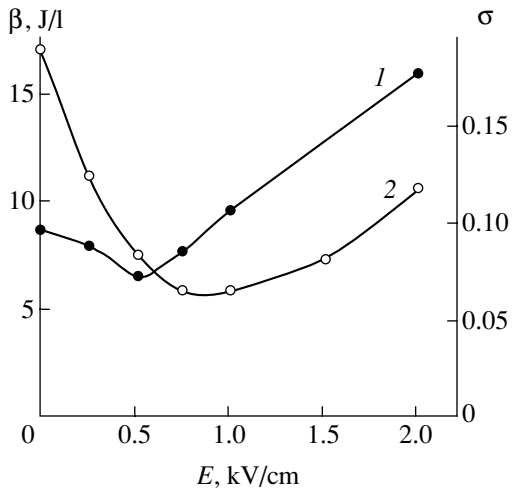

Fig. 2. The plots of parameters (*1*) β and (*2*) σ versus electric field strength E.

centration was observed for the non-self-sustained volume discharge, with the slope of the curves depending on the discharge energy deposited in the gas.

Figure 1 shows typical plots of the logarithm of the initial to current impurity concentration ratio $\ln(C_0/C)$ versus deposited energy W for a styrene-containing gas mixture irradiated by a pulsed electron beam. The energy W was determined as a total energy deposited in a series of the electron beam pulses. As is seen, the right-hand wings of the curves in Fig. 1 corresponding to small initial impurity concentrations can be approximated by straight lines. The slope of these lines can be considered as a characteristic coefficient β [measured in J/l] relating the efficiency of the purification process to the energy consumption:

$$\ln(C_0/C) = W/\beta. \quad (1)$$

The physical meaning of this coefficient is that the β value indicates the amount of energy that has to be deposited in the gas in order to reduce the impurity concentration by a factor of e.

It must be noted that strict validity of the relationship (1) would imply the pseudo-first-order macrokinetics of the styrene vapor removal reaction (with $K[R_i]$ = const, where K is a constant factor):

$$dC/dW \cong dC/dt = -K[R_i]C. \quad (2)$$

This is possible only provided that the concentration $[R_i]$ of all reactive particles involved in the process of styrene removal is almost constant (in other words, these particles are in considerable excess relative to the impurity concentration C). The major part of energy deposited in the gas is spent for generating the active particles, while the fraction spent for the styrene decomposition is small. Since $[R_i] \gg C$ the concentration of the active particles changes mostly in their reactions with other components of the gas mixture.

As can be seen from Fig. 1, the slope of the curves (and, hence, the coefficient β) strongly depends on the initial impurity concentration C_0. The curves significantly deviate from linearity when $\ln(C/C_0)$ is smaller than unity. This fact indicates that styrene molecules present in a sufficiently large amount begin to influence (decrease) the concentration of reactive particles. In this case, we can no longer assume that $[R_i] \gg C_0$ and, therefore, the second order of reaction (2) is manifested at large C_0 values. We may suggest that, at very large impurity concentrations, equation (2) will describe a process of the zero order with respect to the removed component (i.e., the amount of removed molecules will be proportional to the deposited energy). Of course, this assumption is valid only if an increase in the concentration does not lead to a change in the mechanism of impurity removal.

Using the energy coefficient β, one may evaluate the degree of purification η and the energy spent ε per removed impurity molecule from the following relationships:

$$\eta \equiv (1 - [C][C_0]^{-1}) = 1 - \exp(-W\beta^{-1}), \quad (3)$$

$$\varepsilon = 235.5\beta\eta^{-1}[C_0]^{-1}\ln(1-\eta)^{-1}. \quad (4)$$

Formula (4), representing a special form of the general equation (1), shows that the energy spent to remove one impurity molecule depends on the initial impurity concentration and, hence, is not a constant parameter.

Application of an external electric field to the gap irradiated by the pulsed electron beam induces a non-self-sustained volume discharge in the gap. Figure 2 shows an experimental plot of the parameter β versus field strength E (curve *1*) in the discharge column for C_0 = 300 ppm. As is seen from these data, a minimum in the consumed energy is observed for $E \sim 500$ V/cm.

A major contribution to the process of styrene vapor removal from air is due to reactions involving active

oxygen species [2, 3]. Indeed, styrene is virtually not removed from an oxygen-free gas mixture. Reacting with styrene molecules, the active oxygen species, such as atomic and singlet oxygen, ozone, and negative and positive oxygen ions, initiate the polymerization and oxidation reactions. The final products of these reactions in our experiments had the form of a thin polystyrene film containing a certain amount of oxygen, which was deposited on the chamber walls and discharge gap electrodes. A probable mechanism of the polystyrene film formation includes the production of active oxygen species in the gas volume, interaction of these species with styrene molecules and migration of the products toward the walls, activation of the wall surface, and growth of the polymer film on this activated surface.

Another reaction product detected in our experiments was benzaldehyde that is probably formed as a result of the interaction of styrene with ozone generated by the electron beam and discharge. The concentration of benzaldehyde (C_{BA}) observed in our experiments was significantly lower compared to the initial styrene concentration C_0. In order to evaluate the content of benzaldehyde in the gas phase after the irradiation and discharge treatment, we used the parameter $\sigma = (C_0 - C)/C_{BA}$ representing the amount of benzaldehyde molecules per removed styrene molecule. The process of benzaldehyde formation depended on the external electric field strength in the gap. This is illustrated in Fig. 2 by a plot of the parameter σ versus field strength E (curve *2*) for $N \sim 5 \times 10^3$ pulses. As is seen, there is an optimum electric field strength at which the amount of produced benzaldehyde decreases several times as compared to that observed in the absence of applied electric field. For a gas mixture with an initial styrene concentration of 300 ppm irradiated with $N \sim 5 \times 10^3$ pulses at a field strength of 0.8–1.0 kV/cm in the discharge column, the benzaldehyde parameter decreases to $\sigma = 0.06$. This regime can be recommended for development of the corresponding technology of the waste gas purification. The above relationships between the parameters ε, β, and σ together with formulas (3) and (4) provide estimates of the energy characteristics of the process of air purification from styrene vapors.

Acknowledgments. This study was supported by the Russian Foundation for Basic Research, project no. 01-02-96416.

REFERENCES

1. *Non-Thermal Plasma Techniques for Pollution Control*, Ed. by B. M. Penetrante and S. E. Schultheis (Springer-Verlag, Berlin, 1993), Part A.
2. E. J. M. van Heesch, A. J. M. Pemen, Y. Kering, *et al.*, in *Proceedings of the 12th IEEE International Pulsed Power Conference, Monterey, 1999.*
3. Yu. N. Novoselov, Yu. S. Surkov, and I. E. Filatov, Pis'ma Zh. Tekh. Fiz. **26** (13), 23 (2000) [Tech. Phys. Lett. **26**, 550 (2000)].
4. Yu. N. Novoselov and I. E. Filatov, Pis'ma Zh. Tekh. Fiz. **24** (16), 35 (1998) [Tech. Phys. Lett. **24**, 638 (1998)].
5. V. G. Berezkin and V. S. Tatarinskiĭ, *Gas-Chromatographic Methods of Impurity Analysis* (Nauka, Moscow, 1970).

Translated by P. Pozdeev

Technical Physics Letters, Vol. 27, No. 10, 2001, pp. 816–818. Translated from Pis'ma v Zhurnal Tekhnicheskoĭ Fiziki, Vol. 27, No. 19, 2001, pp. 32–38.

Nanometer-Range Modification of Materials Using the Electrodynamic Localization of Optical Radiation

V. A. Kozlov[a], S. V. Obolensky[a]*, and M. A. Kitaev[b]

[a] *Nizhni Novgorod State University, Nizhni Novgorod, Russia*

**e-mail: obolensk@rf.unn.runnet.ru*

[b] *Institute for Physics of Microstructures, Russian Academy of Sciences, Nizhni Novgorod, Russia*

Received June 24, 2001

Abstract—A method based on the electrodynamic localization of optical radiation with the aid of sharp metal objects is proposed, which allows the properties of materials to be modified over a range significantly smaller than the radiation wavelength. © *2001 MAIK "Nauka/Interperiodica".*

The general trend of decreasing the size of elements (e.g., in microelectronics) down to a nanometer range, based on the application of usual optical principles, requires that the radiation wavelength accordingly decrease so as to be smaller than the object dimensions. Obeying this requirement meets large difficulties and leads to considerable expenditures. We suggest to use an electrodynamic method for localization of the optical radiation within a region significantly smaller compared to the radiation wavelength, by analogy with the situation realized with the aid of antennas.

The role of a metal object capable of localizing the optical radiation was played by the gate of a GaAs-based metal–oxide–semiconductor field-effect transistor (MOSFET). The quanta of radiation of a neodymium laser had an energy of about 1.3 eV (1.06 μm), which is smaller than the GaAs bandgap width. This circumstance allowed the samples to be irradiated both from the front side, on which the MOSFET structures were fabricated, and from the rear side (i.e., through the substrate). The gate section [1] had a rhombic shape (0.3×0.5 μm) and the lower rhombus vertex was rounded with a radius of 15 nm. The gate size in the third coordinate could vary within 50–300 μm.

In the case of illumination through the substrate, the optical field in the material under the gate can be presented as a sum of the fields of the incident radiation, that reflected from the radiation wedge sides, and a cylindrical wave radiated from the wedge rib. The field superposition near the wedge rib leads to a local increase in the field component perpendicular to the metal surface within a range determined by the size and shape of the sharp objects rather than by the radiation wavelength.

Objects localizing the radiation were modeled by a wedge formed by the lower gate surface and a strongly elongated ellipsoid roughly approximating the gate shape. In the case of diffraction on the wedge, the laser radiation field can be described by the following expression [2]:

$$V(r, \psi) = \frac{1}{2\gamma}\int_C e^{-ikr\cos\xi}\frac{d\xi}{1 - e^{-i\pi(\xi + \psi)/\gamma}},$$

where C is an integration contour C in the ξ plane comprising two loops with ends at the infinity; r and ψ are the radial and azimuthal cylindrical coordinates, respectively. The current in a source producing a cylindrical wave is proportional to $r^{-1/2}$; that is, it exhibits a singularity at $r \longrightarrow 0$ (where r is the distance to the wedge rib) [3, 4]. In the case of a rounded wedge, r is naturally taken equal to the radius of rounding. For the gate modeled by an elongated ellipsoid, we employed the classical Abraham solution for this electrodynamic problem (see [5]), which allowed resonance properties of the object producing localization of the radiation to be taken into account (these properties are determined by the object geometry).

In the above considerations, it was assumed that the metal is ideal and the radiation does not penetrate into the object. However, the scale of the problem under consideration (hundreds nanometers) is comparable to the skin layer thickness. Nevertheless, a sharp boundary between the gate metal and semiconductor provides for a sharp change in the permittivity. The size of the region featuring a local field amplification remains the same, although the field strength at the singular point decreases. The skin layer thickness was evaluated using a formula for the normal skin effect, because electrons cannot travel through the whole free path length during the period of the field oscillation and the radiation frequency is lower than the plasma frequency [6]. According to the experimental data [7], the skin layer thickness in Au is about 24 nm.

It was assumed that the heat evolution takes place over a laser pulse duration and is localized at the axis of a cylinder corresponding to the wedge rib, with a diam-

eter of 15 nm comparable with the rib radius. The characteristic dimensions of the region of field localization and the pulse duration required for the aerial modification were determined from a solution to the thermal conductivity (written in the cylindrical coordinates with the cylinder axis directed along the wedge rib).

Modification of a given material as a result of the local power deposition takes place upon exceeding a certain threshold determined by the material properties under the conditions of a rapid quasi-adiabatic energy evolution, whereby the spreading heat losses due to the thermal conductivity are small. The first condition determines the radiation source power, while the second condition poses limitations on the laser pulse duration. The smaller the volume of a region to be modified, the more stringent the limitations because a decrease in size leads to increase in the surface to volume ratio. Calculations showed that, with a threshold temperature of 500°C for the defect formation, the modification takes place in a region with dimensions on the order of 60 nm. Figure 1 shows time variation of the temperature in a modified region for layers situated at various depths under the gate vertex. In the case of instantaneous energy deposition on the metal wedge surface, the time during which the temperature exceeds the modification threshold is on the order of 300 ps.

For research purposes, we fabricated GaAs MOSFETs with the gate lengths 10, 1, 05, and 0.25 μm, the last was V-shaped [1]. The gate metallization thickness was 0.5 μm. The substrate thickness for all samples was 100 μm. The gate–drain (source) spacing was varied from 1.5 to 3 μm. The lateral metallization size of the drain and source was 40 μm.

The experiments were performed with a neodymium laser producing pulsed radiation with an energy of 30 mJ/pulse, a single pulse duration of 5–10 ns, and a spot diameter of 2 mm. The inhomogeneity of intensity in the spot reached 200%. After each exposure to laser pulses, the samples were characterized by measuring the current–voltage and capacitance–voltage curves.

1. Transistors with the gate length greater than or comparable with the radiation wavelength. The study of the effect of laser radiation on the MOSFETs with the gate length from 10 to 0.5 μm showed analogous patterns of changes in the characteristics for the samples irradiated from either front or rear sides. This is explained by a small coefficient of the irradiation absorption in GaAs and by a smooth optical field structure varying on the wavelength scale. A change in the shape of characteristics is related to the thermostimulated diffusion of atoms over distances comparable to the MOSFET channel thickness and to the charge carrier trapping on the thermogenerated traps appearing during the laser irradiation. A change in the rate of variation of the MOSFET characteristics depending on the radiation power exhibits a threshold character. As the radiation energy power decreases to 2 mJ/pulse, the MOSFET characteristics remained unchanged to within the accuracy of measurements.

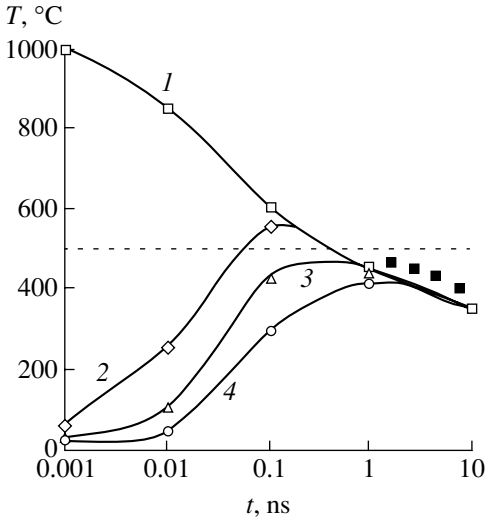

Fig. 1. Time variation of the temperature in the laser-modified region (*1*) at the gate vertex and (*2–4*) at a distance of 45, 75, and 105 nm from the vertex, respectively. Dashed line indicates the modification threshold; black squares show the results of measurements.

Solving the thermal conductivity equation revealed two characteristic time intervals related to spreading of the evolved heat. During the laser pulse (10 ns), the metal contacts heat up to 800–1000°C, after which the sample cools down to 100°C during a time period of about 1 μs.

The conditions of heat removal from a crystal were improved with the aid of glycerin, which possesses sufficiently high insulating properties and does not impair the MOSFET operation. Our experiments showed that the transistor parameters remained unchanged when the samples were irradiated from the rear (substrate) side and the heat was removed from the front side (on which the MOSFET structure was formed). This is explained by a rapid heat removal through a thin metallization layer on the transistor contacts.

2. Transistors with the gate length smaller than the radiation wavelength. In contrast to the case of long-gate MOSFETs, the laser irradiation of transistors with short V-shaped gates leads to different effects depending on the side of exposure. For the samples irradiated from the front side, the device characteristics remained virtually unchanged over a series of ten laser pulses, whereas the samples irradiated from the rear side showed a significant degradation of the characteristics after the first 4–6 pulses (Fig. 2). This is evidence that the gate vertex plays the role of a "concentrator" of the laser radiation field in the working region of the transistor channel. No such concentration takes place during exposure of the front side, and hence, the radiation effect is much less pronounced.

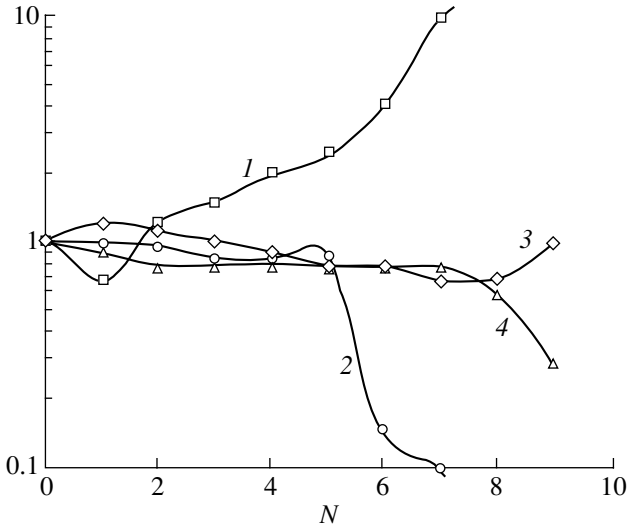

Fig. 2. Relative changes in the parameters of a MOSFET structure with a short V-shaped gate in the course of irradiation with neodymium laser from the rear (substrate) side: (*1*) input resistance; (*2*) drain current; (*3*) gate–drain breakdown voltage; (*4*) drain–source breakdown voltage. *N* are the numbers of sequential laser pulses.

In order to confirm a local character of the material heating under the action of the laser radiation, we conducted experiments in which the rate of heat removal from the front side of MOSFETs was varied during their irradiation from the rear side. When the conditions of heat removal were improved with the aid of glycerin, the modification effect was still observed, showing evidence of the quasi-adiabatic character of processes responsible for the change in MOSFET characteristics.

An analysis of the current–voltage and capacitance–voltage curves of the samples showed that a modified region was located under the gate and had a size not exceeding 100 nm, while the resistance of deeper layers remained unchanged. By measuring variation of the drain current immediately during the irradiation, we evaluated a change in the MOSFET channel temperature with time and established that this behavior was consistent with the results of calculations (Fig. 1).

The results of our experiments show possibility of a local modification of the properties of materials due to the laser radiation field concentrated at a preset site with the aid of sharp metal objects.

Acknowledgments. This study was supported by the Ministry of Science and Technology of the Russian Federation within the framework of the "Physics of Solid State Structures" program (project no. 99-1142) and the SfP grant No. 973799.

REFERENCES

1. S. V. Obolenskiĭ and M. A. Kitaev, Pis'ma Zh. Tekh. Fiz. **26** (10), 13 (2000) [Tech. Phys. Lett. **26**, 408 (2000)].
2. L. D. Landau and E. M. Lifshitz, *Course of Theoretical Physics*, Vol. 8: *Electrodynamics of Continuous Media* (Nauka, Moscow, 1982; Pergamon, New York, 1984).
3. R. B. Vaganov and B. É. Katsenelenbaum, *Foundations of Diffraction Theory* (Nauka, Moscow, 1982).
4. L. B. Felsen and N. Marcuvitz, *Radiation and Scattering of Waves* (Prentice-Hall, Englewood Cliffs, 1973; Mir, Moscow, 1978).
5. L. I. Mandel'shtam, *Lectures on the Theory of Oscillations* (Nauka, Moscow, 1972).
6. V. L. Ginzburg and G. P. Motulevich, Usp. Fiz. Nauk **55** (3), 469 (1955).
7. *Handbook of Optical Constants of Solids*, Ed. by E. Palik (Academic, New York, 1985).

Translated by P. Pozdeev

Technical Physics Letters, Vol. 27, No. 10, 2001, pp. 819–820. Translated from Pis'ma v Zhurnal Tekhnicheskoĭ Fiziki, Vol. 27, No. 19, 2001, pp. 39–43.

Anomalous Electron-Beam-Induced Excitation of Argon in Pulsed Supersonic Streams of Ar + CH_4, Ar + SiH_4, and Ar + CH_4 + SiH_4 Mixtures

V. Zh. Madirbaev, A. E. Zarvin*, N. G. Korobeĭshchikov, and R. G. Sharafutdinov

Novosibirsk State University, Novosibirsk, Russia

**e-mail: zarvin@phys.nsu.ru*

Received March 29, 2001

Abstract—The energy exchange in supersonic streams of argon mixtures with methane and monosilane activated by an electron beam was studied. In the initial condensation stage, the stream features a selective excitation of the atomic energy levels of argon. The threshold values of parameters were determined, for which the anomalous optical emission from the electron-beam-excited mixtures is observed. © *2001 MAIK "Nauka/Interperiodica".*

Development of highly effective plasmachemical flow technologies, widely used for the deposition of coatings, conversion of hydrocarbons, and utilization of industrial waste gases, stimulates the study of energy exchange processes occurring in the condensing gas flows activated by electron beam plasmas [1]. In this context, we have studied the process of anomalous excitation of the radiative states of argon atoms in supersonic streams of argon mixtures with methane and monosilane activated by an electron beam under condensation conditions.

The experiments were performed on the LEMPUS complex setup [2] at Novosibirsk State University. The optical emission spectra excited by an electron beam [3] in pulsed supersonic streams of 5% SiH_4 + 95% Ar, 5% CH_4 + 95% Ar, and 5% SiH_4 + 5% CH_4 + 90% Ar were measured in the range of retarding pressures P_0 = 0–1500 kPa at a temperature of T_0 = 295 K. The measurements were performed at a distance of $x/d_* = 30$ from the supersonic nozzle edge, where $d_* = 0.55$ mm is the nozzle edge diameter. The intensities of the resonance emission lines of argon atom ($\lambda = 549.6$ nm) and ion ($\lambda = 461.0$ nm) were studied as functions of the retarding pressure.

The phenomenon of anomalous increase in the intensity of certain emission lines of argon atoms in the mixtures with monosilane activated by electron beams was originally observed and reported in [4], where the effect was interpreted in terms of the flow condensation process. However, the use of a stationary method for the gas stream production limited the range of retarding pressures studied in that work. Application of a pulsed method allowed this range to be significantly extended, so as to determine the boundary parameters of the stream at which the effect is observed. In addition, it was found that the anomalous optical emission can be observed in argon diluted with methane and in a ternary Ar–SiH_4–CH_4 mixture.

The experimental data presented in Fig. 1 show that the intensity of the argon ion line ($\lambda = 461.0$ nm) always increases linearly with the pressure P_0. For the atomic emission line ($\lambda = 549.6$ nm), the intensity exhibits a short initial portion fitting to the same linear growth, then increases more sharply, and eventually returns to the line approximating the initial portion (solid line in Fig. 1). Both the deviation from and return to the linear

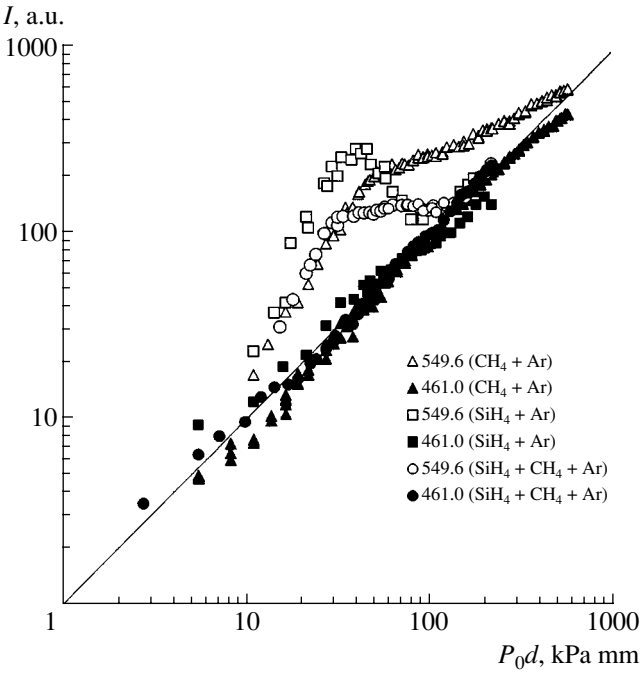

Fig. 1. Intensity of the resonance emission lines of argon atom ($\lambda = 549.6$ nm) and ion versus the retarding pressure.

1063-7850/01/2710-0819$21.00

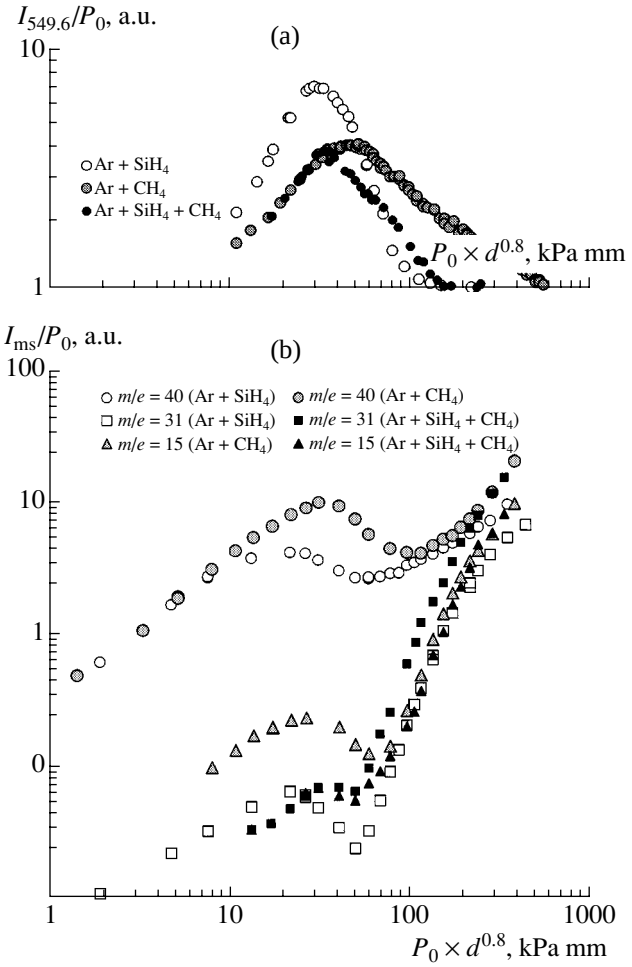

Fig. 2. A comparison of the results of (a) spectroscopic and (b) mass-spectrometric measurements in electron-beam-activated pulsed argon gas streams.

approximation took place at different retarding pressures depending on the mixture composition. The boundaries of the pressure range featuring the nonlinear growth can be seen in Fig. 2a, showing the intensity of the atomic emission line normalized to the retarding pressure (with a coefficient equating the normalized intensity to unity at small P_0 values). With this normalization, it is possible to determine the boundaries of the effect and to compare contributions to the radiative atomic state excitation due to the secondary process (leading to the anomalous intensity increase) and the direct electron impact. Since the $Ar + SiH_4$ mixture exhibits an eightfold increase in the atomic emission line intensity (against fourfold growth for the other mixtures), we may conclude that this secondary process involves a highly efficient excitation channel related to an anomalously large cross section of the collision interaction.

A comparison of the curves showing the optical emission intensity variation to the results of our previous mass-spectrometric measurements [5] for the same gas mixtures (Fig. 2b) shows that the onset of the anomalous excitation process correlates with the initial stage of condensation in the flow, while termination of the former process corresponds to the formation of large (including mixed) clusters [6]. For convenience, the results of the spectral and mass-spectrometric measurements are plotted versus the similarity parameter $P_0^* d^{0.8}$ widely used in the condensation theory.

The observed features of the anomalous argon excitation process (correlation with the mass-spectrometric data, linear dependence on the beam current [4], large cross section of the energy exchange process, and large lifetime of the intermediate excited states) suggest that the atomic argon is energy pumped due to an ion–cluster interaction initiated by the electron beam plasma in the stream. This process results in the formation of long-living excited complexes including atoms of both the carrier gas and the admixture. The excitation transfer to the radiative states of argon is apparently followed by ejection of the excited argon atom from the cluster and by the emission event.

Thus, the effect of the anomalous excitation of argon atoms in the gas mixtures is observed in the range of retardation parameters determined by the conditions of cluster formation and is probably caused by a selective energy exchange in the ion–cluster interaction. The maximum manifestation of the effect corresponds to the region of growing intensity of small clusters [6] detected by methods of the molecular-beam mass spectrometry.

Acknowledgments. This study was supported by the Russian Foundation for Basic Research (project no. 00-03-33021), the Ministry of Education within the framework of the Natural Sciences Program (project no. E00-3.2-150), and the Ministry of Science and Technology of the Russian Federation (project no. 06-05).

REFERENCES

1. A. I. Babariotskii, M. A. Deminskii, A. I. Demkin, *et al.*, High Energy Chem. **33** (1), 45 (1999).
2. A. E. Zarvin, N. G. Korobeĭshchikov, V. Zh. Madirbaev, *et al.*, Prib. Tekh. Éksp., No. 5, 64 (2000).
3. G. G. Gartvich, A. E. Zarvin, V. V. Kalyada, and V. Zh. Madirbaev, Zh. Prikl. Mekh. Tekh. Fiz. **34** (5), 150 (1993).
4. S. Ya. Khmel and R. G. Sharafutdinov, in *Abstracts of Invited Lectures and Contributed Papers of 15th European Sectional Conference on the Atomic and Molecular Physics of Ionized Gases, ESCAMPIG, Hungary, 2000*, Vol. 24A, p. 384.
5. V. Zh. Madirbaev, V. V. Gagachev, A. E. Zarvin, *et al.*, in *Proceedings of the XVIII International Workshop "Gas and Plasma Flows in Nozzles, Jets, and Tracks," St. Petersburg, 2000*, p. 124.
6. R. G. Sharafutdinov, A. E. Zarvin, N. G. Korobeĭshchikov, *et al.*, Pis'ma Zh. Tekh. Fiz. **25** (21), 47 (1999) [Tech. Phys. Lett. **25**, 865 (1999)].

Translated by P. Pozdeev

Technical Physics Letters, Vol. 27, No. 10, 2001, pp. 821–822. Translated from Pis'ma v Zhurnal Tekhnicheskoĭ Fiziki, Vol. 27, No. 19, 2001, pp. 44–48.

The Angular Distribution of Light Ions Past a Thin Carbon Foil

P. Yu. Babenko*, S. S. Kozlovskii, V. I. Afanas'ev, M. I. Mironov, S. Ya. Petrov, A. V. Khudoleev, and F. V. Chernyshev

Ioffe Physicotechnical Institute, Russian Academy of Sciences, St. Petersburg, 194021 Russia

St. Petersburg State Technical University, St. Petersburg, Russia

**e-mail: babenko@npd.ioffe.rssi.ru*

Received May 8, 2001

Abstract—The scattering angles of ions formed upon the transmission of a monoenergetic beam of hydrogen (5–230 keV), deuterium (5–25 keV), or helium-4 (52–230 keV) atoms through a thin (2.7 μg/cm^2) carbon foil were measured. The experimental data are compared to the results of calculations using an SRIM-2000 numerical modeling program. For hydrogen, the isotope effect (i.e., dependence of the angular distribution on the isotope mass) is estimated. *© 2001 MAIK "Nauka/Interperiodica".*

A promising approach to the diagnostics of thermonuclear plasma is based on the analysis of a flux of hydrogen, deuterium, tritium, and helium atoms emitted from the plasma [1]. At present, such an analysis is considered as the main method for determining the isotope composition of a deuterium–tritium fuel mixture in a future tokamak reactor [2]. In the neutral particle analyzers used to monitor the flux of atoms ejected from the plasma, the stripping of atoms is frequently effected by thin-foil targets, after which the flux of secondary ions is analyzed with respect to mass and energy in electric and magnetic field [3]. For optimizing the electric and magnetic field configuration and providing for the most complete particle collection, it is necessary to take into account the scattering of ions in the stripping foil. From this standpoint, the most important energy range of the primary atoms extends from a few units to several hundred kiloelectronvolts.

The purpose of this study was to measure the angular distributions of ions formed upon the transmission of a monoenergetic beam of hydrogen (5–230 keV), deuterium (5–25 keV), or helium-4 (52–230 keV) atoms through a thin (2.7 μg/cm^2) carbon foil and to evaluate the isotope effect (i.e., the dependence of the angular distribution on the isotope mass) for hydrogen ions.

The experiments were performed with a monoenergetic beam of ions that was converted into an equivalent atomic beam upon recharge in a gas target. The atomic beam collimated with a 2-mm diaphragm was directed onto a thin carbon foil oriented perpendicularly to the beam axis. The scattered ions were detected by a channeltron with a 2-mm input hole moved in the plane perpendicular to the beam axis. The distance from the foil target to detector was 390 mm. By measuring the signal from detector as a function of the distance from the beam axis, it is possible to study the angular distribution of the scattered ions and evaluate the angular beam scatter with an allowance for the real experimental geometry.

The experimental data were compared to the results of theoretical calculations of the angular distributions of scattered ions performed using an SRIM-2000 numerical modeling program. The SRIM (Stopping Range of Ions in Matter) code is a program package for calculating the stopping and range of ions in substances in the energy range from 10 eV/amu to 2 GeV/amu) [4]. Using this software, it is possible to calculate the final three-dimensional distribution of ions and the events accompanying the ion energy losses, including the target fracture, sputtering ionization, and phonon generation.

Figure 1 shows the typical angular distributions of ions formed upon the transmission of a monoenergetic beam of 5- and 25-keV hydrogen atoms through a carbon foil with a mass thickness of 2.7 μg/cm^2.

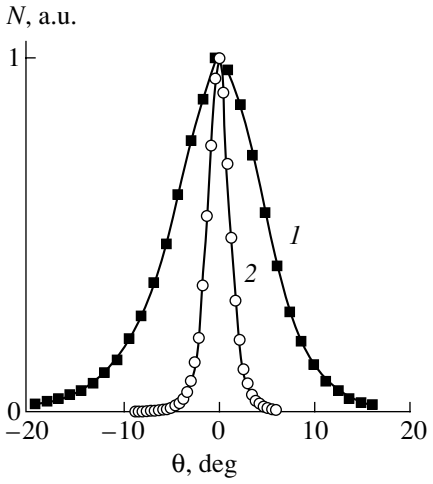

Fig. 1. The experimental angular distributions of ions formed upon the transmission of a monoenergetic beam of (*1*) 5-keV and (*2*) 25-keV hydrogen atoms through carbon foil with a mass thickness of 2.7 μg/cm^2.

1063-7850/01/2710-0821$21.00 © 2001 MAIK "Nauka/Interperiodica"

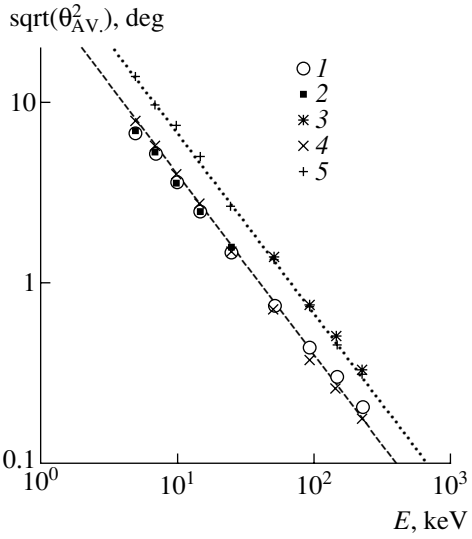

Fig. 2. A plot of the angular scatter versus initial particle energy by experimental data for (*1*) hydrogen, (*2*) deuterium, and (*3*) helium-4 and the results of calculations for (*4*) hydrogen and (*5*) helium-4.

Figure 2 presents the experimental data on the angular scatter of hydrogen, deuterium, and helium ions of various primary energies in comparison to the theoretical energy dependence calculated for hydrogen and helium ions. Here, the ordinate is the square root of the mean-square deviation (this parameter was introduced by Williams in the theory of small-angle multiple scattering [5]). A comparison of the experimental data shows that the angular scatter of hydrogen and deuterium beams in the 5- to 25-keV energy range coincide to within 5%. A conclusion of the absence of a significant isotope effect for hydrogen atoms scattered in thin carbon foils was also made in [6], where analogous measurements were performed in the energy range from 3 to 54 keV. A comparison of the calculated and measured values for hydrogen and helium shows a coincidence to within 20 and 15%, respectively, in the energy range up to 230 keV.

A good agreement of the results of experimental measurements and numerical modeling allow us to consider the scattering data calculated for other elements as reliable as well. In particular, we may use the theoretical data for tritium, which are necessary for the development of a diagnostic equipment for deuterium–tritium plasmas, since the experiments with tritium beams are difficult and expensive.

An analysis of data on the angular scatter of hydrogen, deuterium, and tritium ions depending on the primary atomic beam energy showed that the results coincide for all three hydrogen isotopes to within a 12% accuracy.

The results of our investigation led to the following conclusions.

(i) A comparison of the experimental data on the angular scatter of hydrogen and deuterium ions formed upon the transmission of monoenergetic atomic beams through a thin carbon foil showed that no isotope effect takes place in the energy range from 5 to 25 keV. This result agrees with the theoretical predictions based on the SRIM-2000 model calculations.

(ii) A comparative analysis of the experimental and calculated data for hydrogen, deuterium, and helium ions indicates a good agreement between the results of measurements and computer simulation. This coincidence allows a difficult experiment with tritium to be replaced by the model calculation.

(iii) A comparison of the calculated vales of the angular scatter of hydrogen, deuterium, and tritium ions shows that no isotope scattering effect takes place in the energy range from 5 to 230 keV.

Acknowledgments. The authors are grateful to I.T. Serenkov, V.I. Sakharov, and É.M. Sergun'ko for their help in conducting the experiment, and to M.P. Petrov and A.I. Kislyakov for fruitful discussion of results.

REFERENCES

1. A. B. Izvozchikov and M. P. Petrov, Fiz. Plazmy **2** (2), 212 (1976) [Sov. J. Plasma Phys. **2**, 117 (1976)].
2. ITER Physics Expert Group on Diagnostics, Nucl. Fusion **39**, 2541 (1999).
3. A. V. Khudoleev, V. I. Afanas'ev, A. I. Kislyakov, *et al.*, Fiz. Plazmy **24** (2), 1 (1998) [Plasma Phys. Rep. **24**, 140 (1998)].
4. J. F. Ziegler, J. P. Biersack, and U. Littmark, *The Stopping and Range of Ions in Solids* (Pergamon, New York, 1985).
5. E. J. Williams, Proc. R. Soc. London **169**, 531 (1938).
6. G. Hogberg, H. Norden, and H. G. Berry, Nucl. Instrum. Methods **90**, 283 (1970).

Translated by P. Pozdeev

Technical Physics Letters, Vol. 27, No. 10, 2001, pp. 823–824. Translated from Pis'ma v Zhurnal Tekhnicheskoĭ Fiziki, Vol. 27, No. 19, 2001, pp. 49–52.

The Microstructure of Diamond-Like Films on Silicon Studied with a Laser Microprojector

A. P. Savintsev, V. A. Sozaev, and Kh. T. Shidov

Kabardino-Balkarian State University, Nal'chik, Kabardino-Balkaria, Russia

Received April 20, 2001

Abstract—The microstructure of diamond-like films on silicon substrates was studied using a laser microprojector with the image brightness enhancer. © *2001 MAIK "Nauka/Interperiodica".*

In recent years, the interest in obtaining diamond films on silicon and diamond substrates has grown in connection with the development of a large class of high-temperature and radiation resistant devices such as microwave semiconductor diodes, transistors, optoelectronic devices, etc.

Despite certain progress in the technology of diamond films, the problem of the instability of such films [1], related both to the diamond–carbon phase transition and with a considerable mismatch between the lattice constants of diamond and carbon (0.367 versus 0.755 nm, respectively), is still unsolved. An important role in the development of methods for the low-temperature deposition of diamond-like films belongs to the application of new techniques for monitoring the film microstructure.

We deposited diamond-like films from a carbon-containing gas mixture (3% methane in hydrogen) onto (111)-oriented silicon wafers with the aid of a 1-kW microwave generator. A silicon substrate was mounted in a working chamber on a heated molybdenum table to which a positive voltage was applied from a universal power supply unit. The microwave generator inductor was situated above the substrate. The sample temperature was monitored by a chromel–alumel thermocouple connected to a KSP-4 recording potentiometer. The working gas mixture was admitted to the chamber via needle leak valves.

The influence of the gas phase composition and pressure and the substrate temperature on the shape and size of diamond nuclei formed in the deposits was studied using a laser microprojector with the image brightness enhancer [2, 3]. The image brightness enhancement was provided by a laser light amplifier. The use of laser light amplifiers in optical schemes is effectively implemented with a copper vapor based active element [4]. Such amplifiers can be employed in the optical data transfer systems, in the technological complexes of material processing for microelectronics [3], and some other applications [4].

Although laser microprojectors with the image brightness enhancers feature large light fluxes, the use of an effective laser light enhancer and the selection of a proper optical scheme allow the intensity of irradiation to be reduced to a level producing no damage to the sample surface. For this reason, the study of some objects with a laser microprojector is highly effective, especially with the aid of additional techniques such as the dark-field, bright-field, phase contrast, and polarization methods, etc. The image monitoring can be facilitated by real-time display on screen or in other external readout devices.

Our experimental scheme was based on a Jena-Mikroscope 250-CF instrument equipped with a standard set of planachromatic objective lenses (3.2/0.10; 10/0.25; 20/40; 40/65) and a microobjective lens (5.5/0.16). The entrance and exit pupils of the system coincided with the objective lens barrel, while the exit port coincided with the rear side of the active element. The images were observed and photographed on the screen. The image scale was varied up to 10000. The optical scheme reliably resolved a diffraction grating of 1200 lines/mm.

The laser light amplifier implemented a copper vapor based active element with a GL-202 tube (discharge channel length, 102 cm; diameter, 12 mm) operating at a wavelength of 510.6 and 578.2 nm [5]. The

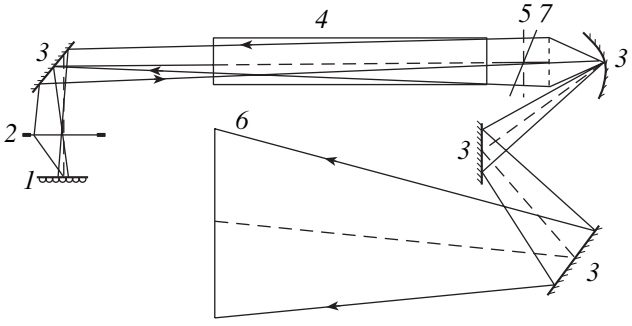

Fig. 1. The optical scheme of a laser microprojector with the image brightness enhancer: (*1*) object; (*2*) microobjective lens; (*3*) mirrors; (*4*) laser light amplifier; (*5*) optical filter; (*6*) screen; (*7*) image.

1063-7850/01/2710-0823$21.00 © 2001 MAIK "Nauka/Interperiodica"

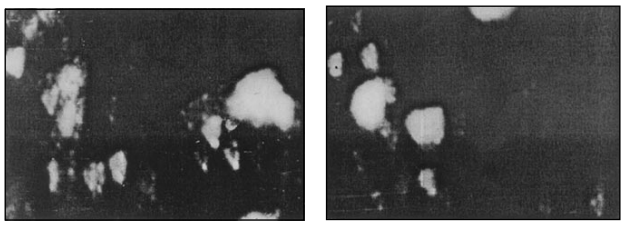

Fig. 2. Typical photographs of diamond-like films on silicon obtained with the aid of a laser microprojector (magnification, ×300).

output light pulses had a duration of 20 ns and were repeated at a rate variable from 8.5 to 11.5 kHz. We have selected an optimum regime for the GL-202 tube operating in the laser microprojector scheme [6]. It was found that the most favorable image observation was provided at a rectifier output power of 2.5 kW (the maximum output power was obtained at a pulse repetition rate of 8.5 kHz). The aforementioned additional techniques (imaging modes) were specially selected for each particular case. The green line (510.6 nm) was separated with the aid of an optical filter possessing a single transmission band with a peak at 490 nm and a halfwidth of 100 nm.

The method described above was used to study the microstructure of diamond-like films on silicon. Figure 2 shows typical photographs of the sample structure made from the screen, which clearly reveal triangular nuclei of the diamond phase in a diamond-like film grown for 1.5 h on a silicon substrate heated to 100°C.

The proposed laser microprojector method has some advantages over scanning electron microscopy: (i) the absence of the film charging effects inherent in the electron microscopy (the laser images are free of the fog typical of the electron-microscopic images); (ii) thin diamond-like films do not degrade in the laser microprojector (in contrast to what takes place in a scanning electron microscope); (iii) no high-vacuum conditions are required for investigation of the sample surface structure.

REFERENCES

1. Yu. A. Kontsevoĭ, Materialovedenie, No. 1, 49 (1997).
2. A. P. Savintsev and A. I. Temrokov, in *Extended Abstracts of the International Conference on Applied Optics-96, St. Petersburg, 1996*, p. 239.
3. K. I. Zemskov and M. A. Kazaryan, Prib. Tekh. Éksp., No. 6, 207 (1978).
4. G. G. Petrash, Vestn. Akad. Nauk SSSR, No. 2, 66 (1987).
5. V. P. Belyaev, V. V. Zubov, M. A. Lesnoĭ, *et al.*, Élektron. Prom-st **5–6**, 82 (1981).
6. A. P. Savintsev, in *Proceedings of the All-Union Conference "Inverse Population and Lasing on Atomic and Molecular Transitions," Tomsk, 1986*, Part 1, p. 131.

Translated by P. Pozdeev

Technical Physics Letters, Vol. 27, No. 10, 2001, pp. 825–826. Translated from Pis'ma v Zhurnal Tekhnicheskoĭ Fiziki, Vol. 27, No. 19, 2001, pp. 53–57.

The Mechanism of Mechanoelectric Transformations in Composite Materials

T. V. Fursa, N. N. Khorsov, and D. B. Romanov

Tomsk Polytechnical University, Tomsk, Russia

Received April 17, 2001

Abstract—The electromagnetic response to impact excitation in high-ohmic composite materials may contain three components. The first component is determined by a change in the dipole moment induced by a striker approaching the surface of a sample possessing a random (surface or bulk) charge; the second component is due to the electrization of a sample material at the point of impact; and the third component is determined by mechanoelectric transformations at the matrix–filler phase boundary. *© 2001 MAIK "Nauka/Interperiodica".*

As is known, the mechanical excitation of dielectric materials gives rise to an electromagnetic response signal [1]. Previously [2, 3], we reported on the results of experimental and theoretical investigation devoted to of the main laws, sources, and mechanisms of mechanoelectric transformations in concretes. A relationship between the electromagnetic response and the material strength was demonstrated in [4]. On the other hand, it was established that not all components of the response signal are determined by the strength. From the standpoint of a signal used for the strength determination, these components of the response appear as noise impairing the measurement algorithm.

Below, we present some new experimental results of our investigations devoted at establishing the mechanisms of the mechanoelectric transformations in composite materials under impact excitation conditions. This research is aimed at refining the algorithm of a nondestructive electromagnetic method developed for the material strength monitoring.

The experiment was conducted as follows. An electromechanical device produced a single dynamic impact on the sample surface. The exciting impact load was normalized in strength and had a pulse duration of 3×10^{-5} s at a striker velocity of about of 2 m/s. The electromagnetic response was detected by an instrument of the EMISSION type [5], which also provided controlled operation of the impact device and performed digitization of the electromagnetic response measured. During the experiments, the arrangement of signal detectors and impact device was always the same.

The results of investigations performed on various heterogeneous materials showed that the electromagnetic response observed upon the impact excitation of some composites, such as silicate ceramics, certain natural minerals, and certain asphalt concretes, differs in shape from the analogous signals detected during the experiments on concretes. Figure 1 shows the shapes of typical electromagnetic signals observed upon the impact excitation of concrete and ceramics. As can be seen, the response of the ceramic sample exhibits a leading front less steep as compared to that in the case of concrete. It was previously established that the process of mechanoelectric transformations in concretes involves two stages: (i) electrization of a sample at the point of impact and (i) mechanoelectric transformations at the matrix–filler phase boundary [6]. The relatively slowly increasing leading front of the response signal from high-ohmic ceramic materials can be related to the presence of uncompensated charge on the

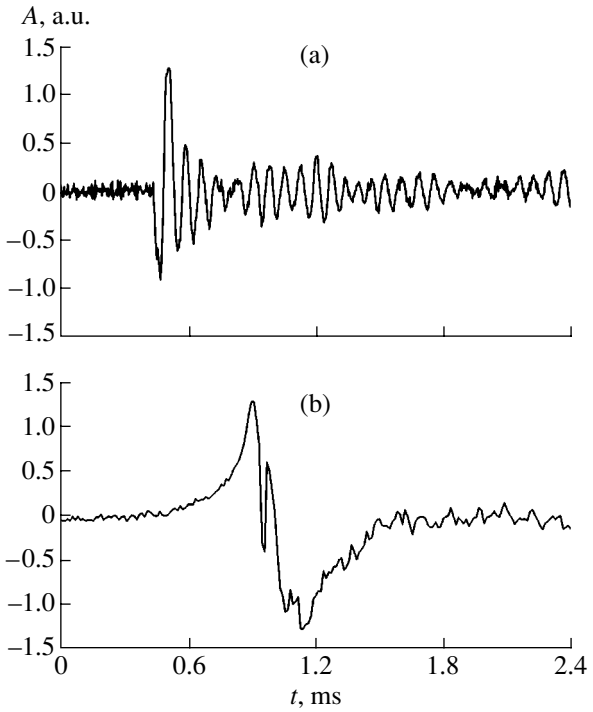

Fig. 1. Typical shapes of the electromagnetic response observed upon the impact excitation of (a) concrete and (b) ceramic samples.

1063-7850/01/2710-0825$21.00 © 2001 MAIK "Nauka/Interperiodica"

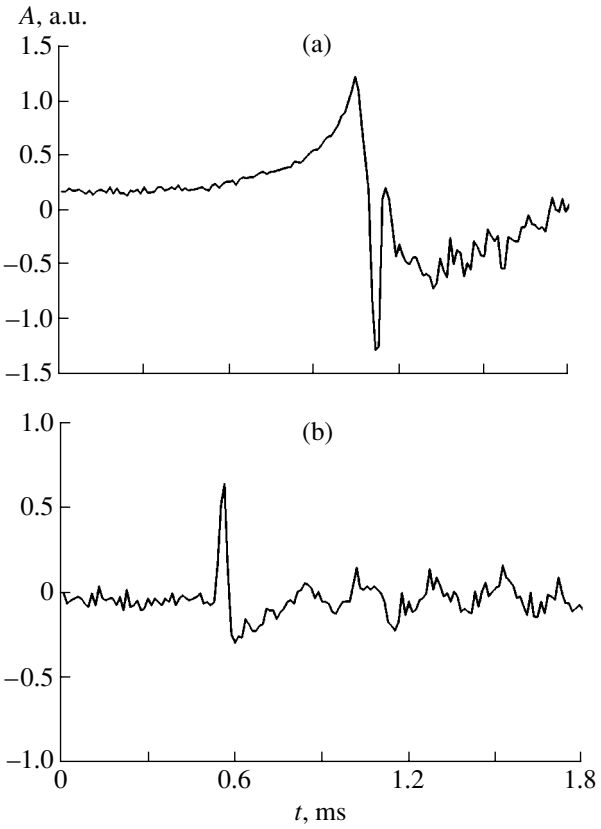

Fig. 2. Typical shapes of the electromagnetic response observed upon the impact excitation of a ceramic sample (a) without and (b) with electrode.

surface or in the volume of these materials. A change in the dipole moment induced by a striker approaching the charged sample surface may give rise to an electric current in the measuring circuit. An evidence for this suggestion is an exponential character of the signal kinetics observed when the striker approaches the sample surface.

In order to check for the validity of this mechanism, we conducted the following experiment. A grounded electrode layer was deposited onto the sample surface, and then the electromagnetic signal was measured in response to the impact. Figure 2 shows the shapes of the electromagnetic signals observed upon the impact excitation of the same sample with and without such a grounded electrode. As is seen, the character of variation of the leading front of the electromagnetic response in the two cases exhibits significant distinctions. The response signal observed upon impact on the sample with electrode exhibits a steeper leading front as compared to that of the signal from a sample without grounded electrode. Direct measurements of the charge values in the ceramic and concrete samples by means of a vibrating electrode technique [7] showed that the ceramic sample bears a surface charge with a density of $\sim 10^{-12}$ C/cm^2, whereas no such charge was detected in the concrete sample.

Thus, the impact excitation of a dielectric material with the aid of a special electromechanical device equipped with a moving metal striker gives rise to a noise component in the response signal when the sample bears a surface or bulk electric charge. This kind of noise can be excluded by applying a grounded electrode layer on the sample surface.

REFERENCES

1. V. F. Gordeev, Yu. P. Malyshkov, V. L. Chakhlov, *et al.*, Zh. Tekh. Fiz. **64** (4), 57 (1994) [Tech. Phys. **39**, 379 (1994)].
2. T. V. Fursa, V. V. Lasukov, Yu. P. Malyshkov, *et al.*, Izv. Vyssh. Uchebn. Zaved., Ser. Stroit., No. 10, 127 (1997).
3. T. V. Fursa, N. N. Khorsov, and E. A. Baturin, Zh. Tekh. Fiz. **69** (10), 51 (1999) [Tech. Phys. **44**, 1175 (1999)].
4. V. L. Chakhlov, Yu. P. Malyshkov, V. F. Gordeev, *et al.*, Izv. Vyssh. Uchebn. Zaved., Ser. Stroit., Nos. 5–6, 54 (1995).
5. V. F. Gordeev, V. P. Eliseev, Yu. P. Malyshkov, *et al.*, Defektoskopiya, No. 4, 48 (1994).
6. T. V. Fursa, Zh. Tekh. Fiz. **71** (7), 53 (2001) [Tech. Phys. **46**, 840 (2001)].
7. C. W. Reedyk and M. M. Pelman, J. Electrochem. Soc. **115** (1), 49 (1968).

Translated by P. Pozdeev

Technical Physics Letters, Vol. 27, No. 10, 2001, pp. 827–829. Translated from Pis'ma v Zhurnal Tekhnicheskoĭ Fiziki, Vol. 27, No. 19, 2001, pp. 58–65.

The Mechanism of Photoluminescence Quenching in Porous Silicon by Electron Irradiation of Various Intensity

B. M. Kostishko* and Yu. S. Nagornov

Ul'yanovsk State University, Ul'yanovsk, Russia

**e-mail: kost@sv.uven.ru*

Received April 13, 2001

Abstract—The charged particle density in an electron beam irradiating porous silicon (por-Si) affects the kinetics of desorption of the surface complexes from por-Si and, accordingly, the degree of photoluminescence quenching in this material. Electron irradiation at a beam density above 5.5×10^{13} cm^{-2} s^{-1} leads to charging of the por-Si surface and to a decrease in the adsorption capacity for the donor molecular groups. © *2001 MAIK "Nauka/Interperiodica".*

In the past decade, porous silicon (por-Si) has become an object of the extensive investigation in many research groups. This interest was inspired by Canham [1], who suggested a quantum character of the photoluminescence (PL) effect in por-Si. At present, the fact that the visible PL in por-Si is related to the nanocrystalline silicon grains with a transverse size of 2–12 nm is reliably established and almost commonly recognized [2, 3], although particular mechanisms of the radiative recombination are still subject to discussion [2, 4]. Most actively developed in the past years was the PL model according to which the light-emitting properties of por-Si are explained by the presence of various molecular groups on the surface of quantum-sized silicon crystal grains [4–7].

Previously [5, 6], the dependence of the PL in por-Si on the electron fluence was studied and it was demonstrated that irradiation of the por-Si surface with medium-energy (2–4 keV) electrons also leads to decomposition of the adsorbed complexes and to a decrease in PL intensity. The degree of the PL quenching by electrons significantly depends on both energy and fluence of the charged particles. The effect of the electron beam intensity was not taken into account and until now has not been studied. However, it is evident that the density of the incident charged particle beam must also influence the kinetics of decomposition of the surface molecular groups. In order to obtain the most complete information about processes occurring on the por-Si surface during electron irradiation, we have studied the effect of the electron beam density on the PL in this material.

The samples were prepared using (100)-oriented *n*-Si single crystal wafers with a resistivity of 32 Ω cm, in which a por-Si layer was formed by a standard procedure of electrochemical etching in a mixed HF–C_2H_5OH (1 : 1) electrolyte. The etching was carried out for 40 min at a current density of 15 mA/cm^2 under illumination with a halogen lamp. The por-Si samples were irradiated with electrons in the analytical chamber of an Auger electron spectrometer (09IOS-10-005 type) at a residual gas pressure below 10^{-7} Pa. The irradiation was performed at an electron energy of $E = 3$ keV to a total dose of $D = 6.25 \times 10^{15}$ cm^{-2}. According to previous results [6], the electron irradiation under these conditions leads to virtually complete decomposition of mono- and dihydride groups passivating walls in the pores, while the radiation defects are not accumulated in any significant amount. The density of charged particles j_{el} in the primary electron beam could be varied from 2.4×10^{13} to 8.3×10^{13} cm^{-2} s^{-1}, this interval being determined only by the characteristics of the available electron gun. For the total fluence to remain constant, the irradiation time was varied from 78 to 260 s. Immediately after irradiation, the samples were brought into contact with air and time variation of the integral laser-excited PL intensity in por-Si was measured. The PL was excited by UV radiation ($\lambda = 325$ nm) of a He–Cd laser operating at a beam power density of $P <$ 80 mW/cm^2.

Figure 1 shows the curves representing the PL degradation in electron-irradiated por-Si prepared and measured as described above. As can be seen from these data, the density of the electron beam used for the preliminary irradiation of por-Si samples significantly affects both intensity and kinetics of the photostimulated surface processes in por-Si. Following the model developed in a number of works [4, 5, 7], the electron-induced degradation of PL excited by the laser radiation is related to decomposition of the hydrogen- and carbon-containing molecular groups, which is manifested by two characteristic times τ_H and τ_C in the PL decay. According to this, each curve in Fig. 1 can be approximated by an equation of the type

$$I_{PL} = A_0 + A_H \exp(-t/\tau_H) + A_C \exp(-t/\tau_C), \quad (1)$$

1063-7850/01/2710-0827$21.00

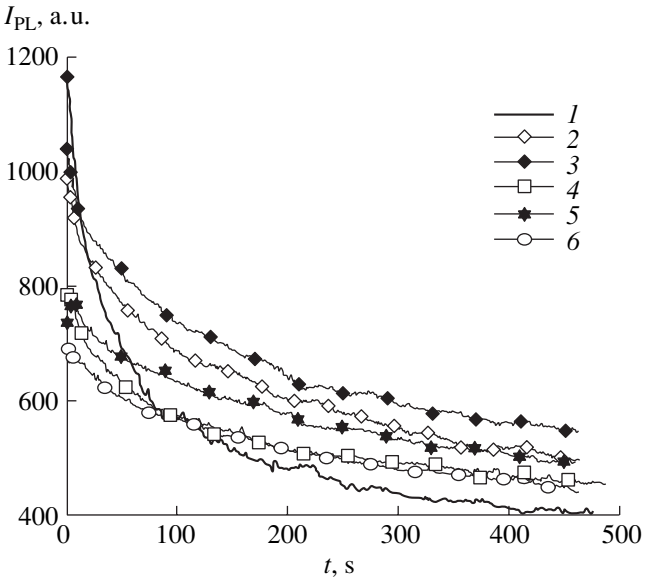

Fig. 1. PL Degradation in various regions of the same por-Si (*1*) unirradiated and (*2–6*) preliminarily irradiated with electrons to a constant dose of $D = 6.25 \times 10^{15}$ cm^{-2} using a beam of variable intensity $j_{el} = 2.4 \times 10^{13}$ cm^{-2} s^{-1} (*2*); $j_{el} = 3.9 \times 10^{13}$ cm^{-2} s^{-1} (*3*); $j_{el} = 5.3 \times 10^{13}$ cm^{-2} s^{-1} (*4*); $j_{el} = 6.6 \times 10^{13}$ cm^{-2} s^{-1} (*5*); $j_{el} = 8.0 \times 10^{13}$ cm^{-2} s^{-1} (*6*).

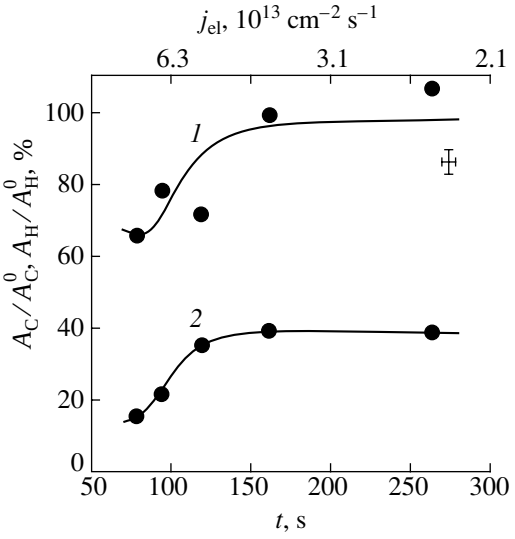

Fig. 2. Plots of the normalized coefficients (*1*) A_C/A_C^0 and (*2*) A_H/A_H^0 in Eq. (1) versus exposure time and electron beam density for por-S irradiated to a constant dose; points present the experimental data, while solid lines show the results of approximation in terms of Eqs. (2).

where A_0 is the PL saturation constant; τ_H and τ_C are the characteristic times of decomposition of the hydrogen- and carbon-containing molecular groups, respectively; and the preexponential factors A_H and A_C are functions of the initial concentrations of these surface groups and the characteristic decomposition times.

Preliminary calculations showed that, under the experimental conditions employed, the τ_H and τ_C values in Eq. (1) fall within the intervals 15–27 and 145–267 s, respectively. Figure 2 shows the plots of A_H and A_C as functions of the electron beam density during the irradiation. The curves are normalized to the values calculated for the por-Si surface not irradiated with electrons (A_H^0, A_C^0). This normalization reveals variation of the concentrations of hydrogen- (A_H/A_H^0) and carbon-containing (A_C/A_C^0) centers in por-Si as a result of the preliminary electron irradiation in vacuum.

The obtained experimental results can be interpreted within the framework of a model taking into account several possible channels for variation in the concentration of chemisorbed complexes on the surface of quantum filaments. The concentration of these surface complexes decreases in as a result of the electron-stimulated desorption [5, 6, 8] and increases due to the adsorption from atmosphere in the pores, which is accompanied by the transfer of desorbed species to the vacuum chamber. Since hydrogen atoms and carbon-containing molecules diffuse in the pores independently of each other, the continuity equations describing variation of the concentrations of these species on the surface and in the volume of pores can be written in the following form:

$$\begin{cases} \partial G_G/\partial t = D_{Kn}\partial^2 C_G/\partial x^2 - \partial C_S/\partial t \\ \partial C_S/\partial t = k_c C_G(C^0 - C_S) - k_d C_S \end{cases}, \qquad (2)$$

where C_S and C_G are the concentrations of hydrogen atoms or carbon-containing molecules on the surface and in the volume of pores, respectively; C^0 is the total concentration of the adsorption centers; k_c and k_d are the coefficients of adsorption and desorption of the surface complexes; x is the pore depth coordinate (a maximum electron penetration depth was take equal to 0.5 μm [5, 6]); and D_{Kn} is the Knudsen diffusion coefficient [5] of the corresponding desorption products.

Thus, a por-Si sample features three fluxes of species in the course of the electron irradiation—diffusion, adsorption, and desorption—proportional to the corresponding coefficients D_{Kn}, k_c, and k_d in system (2). The diffusion coefficient in Eqs. (2) was varied from 0 to 1.28×10^{-8} cm^2/s (the diffusion coefficient of molecular hydrogen in the gas phase [9]).

Numerical calculations showed that the adsorption and desorption fluxes are in equilibrium in the initial irradiation stage (very small irradiation times $t < 1$ s). Then the diffusion flux begins to gradually remove the desorption products, thus controlling the kinetics of decomposition of the surface complexes. For the irradiation times $t < 100$ s, the diffusion flux is insufficient to remove all desorbed products, so that we may expect a decay in the A_H/A_H^0 and A_C/A_C^0 values with time followed by attaining certain constant levels. For the max-

imum electron irradiation time (t = 150 s), the attaining of a constant level observed for the hydrogen-containing PL centers (A_H/A_H^0 in Fig. 2) is possible only for the hydrogen diffusion coefficients exceeding $D_{Kn} = 10^{-12}$ cm^2/s. This value determines the lower boundary of this diffusion coefficient and agrees with the room-temperature value of $D_{Kn} = 8 \times 10^{-12}$ cm^2/s reported previously [6].

The experimental results showed anomalous behavior (Fig. 2), which was manifested by a growth in the A_H/A_H^0 and A_C/A_C^0 values instead of the expected decay. This fact required a more detailed consideration of processes accompanying the electron irradiation and a more thorough analysis of the parameters of system (2). In this context, we have numerically estimated the contributions to the removal of electrons from the sample surface due to secondary emission, diffusion through a high-ohmic [10] porous layer, and drift current. The obtained estimates showed that the surface of quantum filaments must be charged when the por-Si samples are irradiated with electrons at a beam density above 10^{12} cm^{-2} s^{-1}. The surface charging of por-Si up to a level corresponding to a surface charge carrier density of 10^{11} cm^{-2} under the action of 1.2–5 eV light quanta was observed in [11]. In addition, it is known that the adsorption capacity of a sample surface in the course of charging varies with the accumulated potential according to the exponential law [12]. Taking into account that the experiment shows accumulation of the negative charge and that a decrease in the adsorption capacity (and the corresponding adsorption flux) is possible only for donorlike particles [12], we may conclude that the hydrogen- and carbon-containing molecular groups behave as the donor-like centers. With an allowance for all possible processes, the coefficients k_d and k_c were taken in the following form [12]:

$$\begin{cases} k_d = \sigma_0 j_{el}, \\ k_c = k_{c0}\left(1 + \exp\dfrac{m(j_{el} - j_0)}{j_0}\right)^{-1}, \end{cases} \qquad (3)$$

where σ_0 is the interaction cross section, $m \approx 10$ is a dimensionless coefficient, k_{c0} is the coefficient of adsorption of the uncharged surface, and j_0 is the electron beam density for which the surface charging becomes a factor significant for the adsorption capacity.

Approximation of the experimental A_H/A_H^0 and A_C/A_C^0 values (Fig. 2) by smooth lines according to Eq. (2) shows that an allowance for the surface charging provided for a sufficiently adequate description of the experiment. The results of calculations showed that the adsorption coefficient k_c decreases by half for an electron beam density of $j_0 = 5 \times 10^{13}$ cm^{-2} s^{-1}. Figure 2 (curve *1*) indicates that there is a certain discrepancy between theory and experiment for the carbon-containing surface complexes; in addition, no clearly pronounced saturation is observed for the electron beam intensities below 5×10^{13} cm^{-2} s^{-1} and the experimental A_C/A_C^0 value exceeds the level of 100%. In our opinion, this fact can be explained by assuming that an electron-stimulated adsorption of carbon on the surface of quantum filaments (also observed in [13]) rather than desorption takes place in our samples.

Thus, we have studied the influence of the electron irradiation intensity on the PL in por-Si. The experimental data were adequately explained in terms of the desorption and adsorption of hydrogen- and carbon-containing groups, their diffusion removal from pores in the course of electron irradiation, and charging of the sample surface.

Acknowledgments. This work was supported by the Federal "Russian Universities–Fundamental Research" Program and by the Russian Foundation for Basic Research (project nos. 99-02-17903 and 01-02-06154).

REFERENCES

1. L. T. Canham, Appl. Phys. Lett. **57**, 1046 (1990).
2. A. G. Cullis, L. T. Canham, and P. D. J. Calcott, J. Appl. Phys. **82** (3), 909 (1997).
3. M. Cruz, M. R. Beltran, *et al.*, Phys. Rev. B **59** (23), 15381 (1999).
4. K. N. El'tsov, V. A. Karavanskiĭ, *et al.*, Pis'ma Zh. Éksp. Teor. Fiz. **63** (2), 106 (1996) [JETP Lett. **63**, 119 (1996)].
5. B. M. Kostishko and A. M. Orlov, Zh. Tekh. Fiz. **68** (3), 58 (1998) [Tech. Phys. **43**, 318 (1998)].
6. B. M. Kostishko, M. B. Guseva, *et al.*, Phys. Low-Dimens. Struct. **7/8**, 9 (1999).
7. I. M. Chang, G. S. Chuo, *et al.*, J. Appl. Phys. **77** (10), 5365 (1995).
8. S. P. Zimin, D. S. Zimin, *et al.*, Phys. Status Solidi A **182**, 221 (2000).
9. *Handbook of Physical Quantities*, Ed. by I. S. Grigoriev and E. Z. Meilikhov (Énergoatomizdat, Moscow, 1991; CRC Press, Boca Raton, 1997).
10. S. P. Zimin, Fiz. Tekh. Poluprovodn. (St. Petersburg) **34** (3), 359 (2000) [Semiconductors **34**, 353 (2000)].
11. A. V. Petrov and A. G. Petrukhin, Fiz. Tekh. Poluprovodn. (St. Petersburg) **28** (1), 82 (1994) [Semiconductors **28**, 49 (1994)].
12. F. F. Vol'kenshteĭn, *Electron Processes on Semiconductor Surface during Chemisorption* (Nauka, Moscow, 1987).
13. B. M. Kostishko, Sh. R. Atazhanov, *et al.*, Izv. Vyssh. Uchebn. Zaved., Élektron., No. 6, 5 (1999).

Translated by P. Pozdeev

Technical Physics Letters, Vol. 27, No. 10, 2001, pp. 830–833. Translated from Pis'ma v Zhurnal Tekhnicheskoĭ Fiziki, Vol. 27, No. 19, 2001, pp. 66–75.

A Model of Coupled Resonators for Calculating the Electromagnetic Wave Diffraction on Planar One-Dimensional Bragg Gratings

P. V. Petrov

Institute of Technical Physics, State Nuclear Research Center of the Russian Federation, Snezhinsk, Russia
e-mail: p.v.petrov@vniift.ru

Received February 12, 2001

Abstract—The problem of excitation of a one-dimensional planar Bragg grating is studied. A model of coupled resonators is proposed for investigating the diffraction of electromagnetic waves on a waveguide surface with arbitrary corrugation profile. The model is based on the strict relationships derived from a solution to a two-dimensional boundary problem for the Helmholtz equation. A particular form of equations is presented for the case of a rectangular corrugation of plates in the grating. *© 2001 MAIK "Nauka/Interperiodica".*

A promising approach to the creation of electrodynamic systems for free-electron masers is based on the use of Bragg resonators [1–4], implementing distributed feedback and providing for a spatially coherent radiation. The Bragg resonators for such systems represent waveguide sections with one- and two-period corrugation (Bragg gratings) [1, 5].

The mathematical models used in descriptions [1–5] of the mode spectra and reflection coefficients of the Bragg gratings are based on the theory of coupled modes [1] in which deformation of the waveguide surface $l(\mathbf{r}) = 0$ (determined by the corrugation) is replaced by an "equivalent" boundary condition on the nonperturbed surface of a regular waveguide (Fig. 1) [6]:

$$\mathbf{E}_\tau = \nabla(l(\mathbf{r})\mathbf{E}\cdot\mathbf{n}) - i\frac{\omega}{c}l(\mathbf{r})[\mathbf{n},\mathbf{H}], \qquad (1)$$

where $\mathbf{n}$ is the outward normal to the waveguide surface; $\mathbf{E}$, $\mathbf{H} \propto \exp(-i\omega t)$ are the electric and magnetic fields in the regular waveguide; and ω is the circular frequency of the radiation.

Conditions for the applicability of this approximation [6] are (i) the smallness of deformation (corrugation depth must be much smaller compared to the wavelength of the incident radiation and to the corrugation period) and (ii) the smallness of the angle of intersection between deformed and nondeformed surfaces.

Almost all experiments with the Bragg resonators employ the gratings with rectangular corrugation [1–5], which satisfy the condition of small deformations and fail to obey the condition smallness of the intersection angle. Therefore, it is very important to develop a physical–mathematical model adequately describing the diffraction of electromagnetic waves on one- and two-dimensional Bragg gratings without using the perturbation theory. Below, we present the model of coupled resonators for calculating the diffraction of electromagnetic waves on a one-dimensional planar Bragg grating.

Let us consider a planar waveguide with perfectly conducting (metal) walls, which is infinite in the OY direction, symmetric relative to the OX axis, and bears a finite number of corrugations described by the functions $x = l_q(z)$ ($0 \le z \le L$; $q = 1, \ldots, M$), determined so that the surface of a nonperturbed (regular) waveguide corresponds to $x = l_0(z) = \pm L_x$ (Fig. 1). The consideration will be restricted to the case of excitation of the TM modes, in which only the E_x, E_z, H_y components are nonzero. Let the Bragg grating be excited by a TEM mode of the nonperturbed waveguide from the side of negative z. In this case, the initial vector problem of determining the electromagnetic waves reduces to a boundary problem for the scalar Helmholtz equation relative to the magnetic field component $H \equiv H_y(x, z)$:

$$\left(\frac{\partial^2}{\partial x^2} + \frac{\partial^2}{\partial z^2} + k^2\right)H = 0,$$
$$(x, z) \in \Omega = \bigcup_{q=1}^{M}\Omega_q \bigcup \Omega_0, \qquad (2)$$

where $\Omega_0 = \{0 < x < L_x, -\infty < z < \infty\}$ is the regular waveguide region; $\Omega_q = \{L_x < x < l_q(z), 0 < z < L\}$ is the region of the qth corrugation; $q = 1, \ldots, M$. The Helmholtz equation is solved with the following boundary conditions.

(i) Conditions on the metal surface and in the OZ symmetry plane:

$$\left.\frac{\partial H}{\partial \mathbf{n}}\right|_{S = \bigcup\limits_q \{x = l_q(z)\} \bigcup \{x = 0\}} = 0; \qquad (3)$$

(ii) a condition of the TM mode excitation at $z = 0$:

$$\frac{\partial H}{\partial z} + ikH = 2ik; \tag{4}$$

and (iii) a condition of the free wave escape from the system at $z = L$:

$$\frac{\partial H}{\partial z} - ikH = 0. \tag{5}$$

A solution to Eq. (2) with the boundary conditions (3)–(5) will be obtained separately for each qth corrugation and for the regular waveguide region (in the latter region, the solution is presented as a sum of the incident and scattered fields):

$$H = \begin{cases} H_0 + H_s, & \mathbf{r} \in \Omega_0, \\ H_q, & \mathbf{r} \in \Omega_q. \end{cases} \tag{6}$$

Taking into account the condition of continuity of the tangential field components at the regular waveguide boundary $x = l_0(z) = L_x$, we obtain the relationship

$$H_q(z) = H_0(z) + H_s(z). \tag{7}$$

Assuming that, at the boundary between corrugated and regular waveguide regions, the electric field component along OZ is determined by a certain function $E_z(x = L_x, z) = E_\tau(z)$, we obtain the following boundary problem for determining H_s in the Ω_0 region:

$$\left(\frac{\partial^2}{\partial x^2} + \frac{\partial^2}{\partial z^2} + k^2\right)H_s = 0, \quad \left[\pm\frac{\partial H_s}{\partial z} + ikH_s\right]\Big|_{z = 0, L} = 0,$$
$$\frac{\partial H_s}{\partial x}\Big|_{x = 0} = 0, \quad \frac{\partial H_s}{\partial x}\Big|_{x = L_x} = -ikE_\tau(z). \tag{8}$$

A solution to this problem can be presented in terms of the Green function [7]:

$$H_s(x, z) = -\frac{ik}{4\pi}\int_0^L dz' G_k(x, z, L_x, z')E_\tau(z'), \tag{9}$$

$$G_k(x, z, x', z') = \frac{2\pi i}{L_x}\sum_{\nu = 0}^{\infty}\varepsilon_\nu \cos(g_\nu x)\cos(g_\nu x')\frac{e^{i|z - z'|h_\nu}}{h_\nu},$$
$$g_\nu = \frac{\pi\nu}{L_x}, \quad h_\nu = \sqrt{k^2 - g_\nu^2}, \quad \varepsilon_\nu = \begin{cases} 2, & \nu = 0, \\ 1, & \nu \neq 0. \end{cases} \tag{10}$$

On the regular waveguide surface, expression (9) for $H_s^s(z) \equiv H_s(x = L_x, z)$ can be conveniently written in a more compact form:

$$H_s^s = -ik\hat{G}_R E_\tau,$$
$$\hat{G}_R = \frac{i}{2L_x}\sum_{\nu = 0}^{\infty}\frac{\varepsilon_\nu}{h_\nu}\int_0^L dz' \exp(ih_\nu|z - z'|). \tag{11}$$

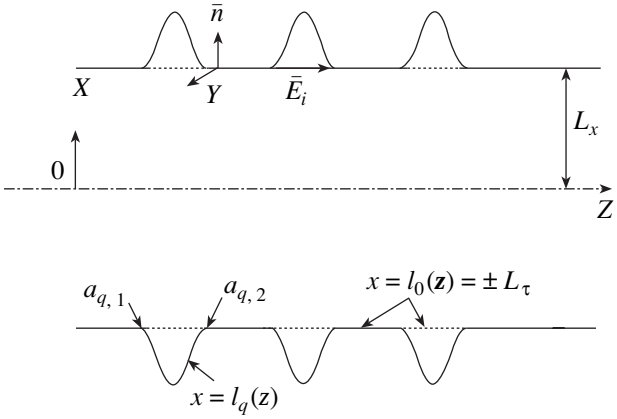

Fig. 1. Schematic diagram of a planar Bragg grating.

Let us find a relationship between the electric field $E_\tau(z)$ and the magnetic field H_q at the boundary of the qth corrugation Ω_q and the regular waveguide $x = l_0(z)$, $a_{q,1} \le z \le a_{q,2}$. In the region of $\Omega_q = \{a_{q,1} \le z \le a_{q,2}, L \le x \le l_q(z)\}$, the magnetic field $H_q(x, z)$ is a solution to Eq. (2) with the homogeneous Neiman conditions (3) on the metal corrugation surface $x = l_q(z)$ and condition (7) on the boundary with the regular waveguide surface $x = l_0(z)$. Using the Green function [7], the magnetic field $H_q(x, z)$ can be expressed through the values of the field on the boundary of the qth corrugation $S_q = \{x = l_q(z)\} \cup \{x = l_0(z)\}$, $a_{q,1} \le z \le a_{q,2}$:

$$H_q(x, z) = \oint_{S_q} d\mathbf{S}_q H(\mathbf{r}_s')G_q(x, z, \mathbf{r}_s')$$
$$= \int_{a_{q,1}}^{a_{q,2}} dz'(H_0^s(z') + H_s^s(z'))G_q(x, z, z'), \tag{12}$$

where G_q is the surface Green function for the Helmholtz equation in the Ω_q region, which satisfies the same boundary conditions on S_q as does the $H_q(x, z)$ field to be determined. Accordingly, the electric field $E_z^q(x, z)$ in the region of the qth corrugation is

$$E_z^q(x, z) = -\frac{1}{ik}\frac{\partial H_q(x, z)}{\partial x}$$
$$= -\frac{1}{ik}\int_{a_{q,1}}^{q_{q,2}} dz'(H_0^s(z') + H_s^s(z'))\frac{\partial}{\partial x}G_q(x, z, z'). \tag{13}$$

Taking into account the mutual arrangement of corrugations, the expression for $E_\tau(z)$ on the entire regular waveguide surface $z \in [0, L]$ can be written in terms of

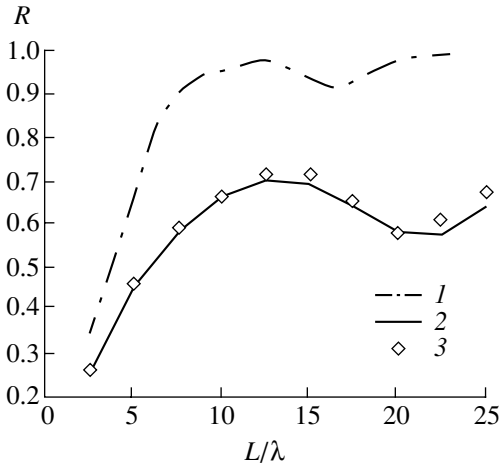

Fig. 2. The reflection coefficient of a TEM wave in the Bragg resonance ($h_\nu + h_0 \approx h$, ν = 75 GHz) as a function of the length of a one-dimensional Bragg grating with a period of 0.2 cm bearing a rectangular corrugation with the width a = 0.1 cm and the depth d = 0.03 cm calculated by methods of (*1*) coupled modes, (*2*) coupled resonators, and (*3*) finite elements.

the Heaviside function $\eta(x) = \{0, x < 0; 1, x > 0\}$ in the operator form

$$E_\tau(z) = -\frac{1}{ik}\hat{G}_{in}(H_0^s + H_s^s),$$
$$\hat{G}_{in} = \sum_{q=1}^{M}(\eta(z - a_{q,1}) - \eta(z - a_{q,2}))\hat{G}_{in}^q, \quad (14)$$

$$\hat{G}_{in}^q = \int_{a_{q,1}}^{a_{q,2}} dz' \frac{\partial}{\partial x} G_q(x, z, z')|_{x = L_x}. \quad (15)$$

Using relationships (11) and (14), we obtain the following Fredholm equation of the first kind for determining $H_s^s(z)$:

$$H_s^s - \hat{G}_R\hat{G}_{in}H_s^s = \hat{G}_R\hat{G}_{in}H_0^s. \quad (16)$$

The solution to this equation can be written as

$$H_s^s = (\hat{I} - \hat{G}_R\hat{G}_{in})^{-1}\hat{G}_R\hat{G}_{in}H_0^s. \quad (17)$$

Using this $H_s^s(z)$ function, we can determine $E_\tau(z)$ from relationship (14) and then calculate $H_y(x, z)$ according to expression (9) at any point of the electrodynamic structure.

Based on the obtained expression, we may derive some qualitative conclusions about the behavior of the solution; in particular, we can approximately determine the region of resonance scattering. If the corrugation is described by a periodic function of the type $\hat{G}_{in} \sim \cos(hz)$ with $h = 2\pi/b$ and $\hat{G}_R \sim \exp(ih_\nu|z - z'|)$, the scattered field in the region $z < 0$ is

$$H_s \sim \hat{G}_R\hat{G}_{in}H_0 \propto \exp(-ih_\nu z)\int dz'(\exp(i(h_\nu + h_0 + h)z') - \exp(i(h_\nu + h_0 - h)z')). \quad (18)$$

This relationship indicates that the resonance scattering of a wave with the longitudinal wavenumber h_0 into a wave with the wavenumber h_ν takes place when the sum of these wavevectors is close to the corrugation wavevector (the Bragg resonance condition):

$$h_\nu + h_0 \approx h. \quad (19)$$

The operator $\hat{G}_{in}$ determines the influence of the corrugation profile on the diffraction field. The simplest example is offered by a rectangular corrugation profile with a width a, a depth $d = \max(l_q(z))$ ($z \in [0, L]$), and a period b on the surface of a plane waveguide. Using an explicit expression for the Green function in the form of a series for the Helmholtz equation (2) in a rectangular region with the homogeneous Neiman conditions on three boundaries and an inhomogeneous Dirichlet condition on the fourth boundary, we obtain a formula for the operator $\hat{G}_{in}$:

$$\hat{G}_{in}(z, z') = -\frac{2}{a}\sum_{q=0}^{M-1}[\eta(z_q) - \eta(z_q - a)] \times\left(\sum_n \gamma_n \cos(\chi_n z_q)\int_{z_q}^{z_q + a} dz' \cos(\chi_n(z' - bq))\right),$$
$$\gamma_n = \frac{\beta_n}{\varepsilon_n}\tanh(\beta_n d), \quad \chi_n = \frac{\pi n}{a}, \quad (20)$$
$$\beta_n = \sqrt{\chi_n^2 - k^2}, \quad z_q = z - qb.$$

Since practical applications of the Bragg gratings are mostly related to their reflection properties, it is interesting to determine the region of highly effective and selective reflection of electromagnetic waves depending on the corrugation length and the incident radiation frequency for a given corrugation period and depth. We determined the reflection properties of a one-dimensional Bragg grating for a planar waveguide with the plate spacing $2L_x$ = 1 cm, a rectangular corrugation profile with a period of 0.2 cm and a width of a = 0.1 cm.

Figure 2 shows the results of calculations of the reflection coefficient for a TEM mode with the frequency ν = 75 GHz satisfying the Bragg resonance condition (19). The reflection coefficient was calculated as a function of the corrugation length using the model of coupled resonators (CR) through numerical solution of Eq. (17) with operator $\hat{G}_{in}$ in the form (20). For comparison, Fig. 2 presents the reflection coefficients calcu-

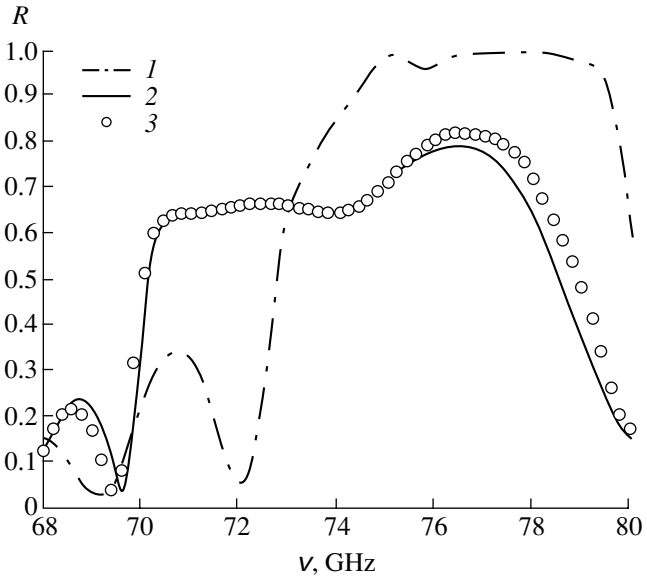

Fig. 3. The reflection coefficient of a TEM wave versus frequency for a one-dimensional Bragg grating with the length $L = 5$ cm bearing a rectangular corrugation with the period 0.2 cm, the width $a = 0.1$ cm and the depth $d = 0.03$ cm calculated by methods of (*1*) coupled modes, (*2*) coupled resonators, and (*3*) finite elements.

lated using the theory of coupled modes (CM) [1, 5] and the method of finite elements (FE) [8].

Figure 3 presents the total reflection coefficient as a function of the TEM mode frequency for a Bragg grating with the length $L = 5$ cm calculated by various numerical methods. As can be seen, the region of wave reflection is determined by the Bragg resonance condition (19): TEM to TEM for the frequency $\nu = 75$ GHz and TEM to TM_{02} for $\nu = 78$ GHz. However, the reflection coefficients determined by the FE and CR methods significantly differ from the values obtained using the CM method. The coupled mode model only qualitatively determines the positions of resonance reflection bands and roughly estimates their widths and reflection coefficients.

The obtained results indicate that, in comparison with the model of coupled modes, the method of coupled resonators more correctly describes dependence of the refection coefficient R on the incident radiation frequency and the corrugation length of a one-dimensional grating. The values obtained by the method of coupled resonators agree well with the results of numerical modeling using the method of finite elements; however, an advantage of the method of coupled resonators is the significant decrease in the computational time.

Thus, we developed a model of coupled resonators intended for calculating the electromagnetic fields excited in a one-dimensional Bragg grating. The model equation, derived without additional assumptions from the solution to a two-dimensional boundary problem for the Helmholtz equation, can be used for calculating the corrugated waveguide structures of arbitrary shapes and dimensions. Moreover, the proposed approach allows a direct and quite clear generalization to a two-dimensional case. This is important for the calculation of electromagnetic fields in two-dimensional Bragg gratings, where direct modeling is related to solving three-dimensional problems.

REFERENCES

1. G. G. Denisov and M. G. Reznikov, Izv. Vyssh. Uchebn. Zaved., Radiofiz. **25** (5), 562 (1982).
2. V. L. Bratman, N. S. Ginzburg, and G. G. Denisov, Pis'ma Zh. Tekh. Fiz. **7** (21), 1320 (1981) [Sov. Tech. Phys. Lett. **7**, 565 (1981)].
3. N. S. Ginzburg, N. Yu. Peskov, and A. S. Sergeev, Pis'ma Zh. Tekh. Fiz. **18** (9), 23 (1992) [Sov. Tech. Phys. Lett. **18**, 285 (1992)].
4. N. S. Ginzburg, N. Yu. Peskov, A. S. Sergeev, *et al.*, Nucl. Instrum. Methods Phys. Res. A **358**, 189 (1995).
5. N. Yu. Peskov, N. S. Ginzburg, G. G. Denisov, *et al.*, Pis'ma Zh. Tekh. Fiz. **26** (8), 72 (2000) [Tech. Phys. Lett. **26**, 348 (2000)].
6. B. Z. Katsenelenbaum, *Theory of Irregular Waveguides with Slowly Varying Parameters* (Akad. Nauk SSSR, Moscow, 1961).
7. P. M. Morse and H. Feshbach, *Methods of Theoretical Physics* (McGraw-Hill, New York, 1953; Inostrannaya Literatura, Moscow, 1958, 1959), Vols. 1 and 2.
8. *Partial Differential Equation Toolbox User's Guide* (The MathWorks Inc., 1997).

Translated by P. Pozdeev

Technical Physics Letters, Vol. 27, No. 10, 2001, pp. 834–837. Translated from Pis'ma v Zhurnal Tekhnicheskoĭ Fiziki, Vol. 27, No. 19, 2001, pp. 76–84.

Degradation Processes in the Aluminum–Silicon System Induced by Pulsed Electric Signals

A. A. Skvortsov*, A. M. Orlov, and A. A. Salanov

Ul'yanovsk State University, Ul'yanovsk, Russia

**e-mail: scvor@sv.uven.ru*

Received May 11, 2001

Abstract—Thermal conditions in a metallization layer deposited onto a single crystal silicon substrate were studied during the passage of single electric pulses with a current density of $j = (1–8) \times 10^{10}$ A/m^2 and a duration of $\tau = 50–800$ μs. Mechanisms of the irreversible degradation in the aluminum–silicon contact under the pulsed current action are established. The degradation is manifested by the contact melting and the metallization layer fusion. Methods for the identification of these phenomena and determination of the critical current densities j_k are proposed. The critical current density depends on the current pulse duration as described by the relationship $j_k \sim 1/\sqrt[4]{\tau}$. It is established that the passage of single current pulses with $j \geq 5 \times 10^{10}$ A/m^2 and $\tau \geq 200$ μs leads to the formation of linear defects in the region of maximum temperature gradient in the test structure. © *2001 MAIK "Nauka/Interperiodica".*

As is known, breakage of the metal–semiconductor contacts and degradation of the metallization layers leads to irreversible failures in semiconductor devices [1–3]. These events are preceded by electrically stimulated degradation phenomena typically beginning at the sites of metal film bending, mechanical and structural defect localization, and phase contacts. We believe that especially significant effects are produced by pulsed electric signals, since the resulting electric transport processes can lead (within a time period as short as 10–100 μs [2, 3]) to irreversible degradation of a contact system. In connection with this, our aim was to study the degradation processes in most widely used aluminum–silicon (Al–Si) system caused by the passage of rectangular electric pulses with a current density of $(1–8) \times 10^{10}$ A/m^2 and a duration of $\tau = 100–800$ μs.

The temperature regimes of operation of the test structures wee studied as described elsewhere [4, 5]. The semiconductor substrates represented 350-μm-thick (111)-oriented phosphorus-doped silicon single crystal wafers with a resistivity of 20–30 Ω cm. Such substrates virtually do not short the metallization layers, which markedly facilitates the analysis of the thermal flux redistribution in the test structures.

Aluminum films were deposited by electron-beam evaporation in vacuum onto the silicon substrates heated to 473 K at a residual pressure of 7×10^{-4} Pa. The deposition was performed at a rate of 2 nm/s for a time not exceeding 40 min. After the metal film deposition, the test structures depicted in Fig. 1 were formed by methods of contact photolithography.

The temperature regimes of the test structure functioning were studied by measuring the switch-on voltage oscillograms $U(t)$ with the aid of various potential contacts of the sample. The temperature dynamics $\Delta T = T - T_0$ in a given region of the test structure was readily evaluated from $U(t)$ by the formula

$$\Delta T(t) = \frac{1}{\alpha}\left(\frac{U(t)}{U_0} - 1\right), \quad (1)$$

where α (K^{-1}) is the temperature coefficient of resistance $U_0 = IR_0$, I is the current passing in the structure (A), and R_0 (Ω) is the resistance at $\Delta T = 0$.

A change in the system characteristics during the current pulse was monitored by the dynamics of temperature variation of the aluminum film, which is related to the semiconductor matrix by a relationship [6]

$$\Delta T = T_I - T_0 = \frac{I^2 \bar{R}}{\bar{d}S\bar{C}}\sqrt{\frac{t}{\bar{a}}}. \quad (2)$$

Here, I is the current pulse amplitude; S (m^2) is the area of the metal–semiconductor thermal contact; R (Ω) is the resistance of the metallization strip; C (J/(kg K)), a (m^2/s), and d (kg/m^3) are the heat capacity, temperature diffusivity, and density of silicon, respectively. The upper bar indicates a temperature-integral average.[1]

The behavior predicted by relationship (2) is consistent with experiment up to a current density of 4×10^{10} A/m^2. In this range, the true current densities j do

[1] The temperature-integral average of a quantity $\bar{b}$ is defined as $\bar{b} = \frac{1}{\Delta T}\int_{T_0}^{T_1} b(T)dT$.

not reach a critical level,[2] as indicated by a monotonic variation of $U(t)$ in the experimental oscillograms (Fig. 2, curve *1*). It must be noted that a possible degradation of some local microscopic regions of aluminum does not introduce significant thermal perturbations into the test structure conducting the current pulses with subcritical amplitudes j.

The pulses with large j values modify the structure of local areas in the current-conducting film. This is manifested by the formation of a liquid layer at the Al–Si interface caused by the contact melting of components upon heating up to the eutectic temperature (850 K). The oscillograms measured in such areas not only allow the beginning and end of the overall degradation phenomena to be determined but indicate a sequence of the stages of the contact melting and aluminum strip fusion during the current pulse.

Indeed, the gradual formation of a melted layer is accompanied by the current redistribution toward liquid phase. This phase begins to form at the eutectic temperature and actively grows at elevated temperatures. The current redistribution between conducting phases leads to a decrease in j, which is manifested in the oscillograms by a drop in the potential $U(t)$ observed at 440 μs (Fig. 2, curve *2*).

At large densities of the thermal fluxes generated by high j values, a dominating role in the degradation process belongs to local fusion of the metallization layer. This is accompanied by sharp jumps in the potential oscillograms $U(t)$, with the slope of the corresponding fragment (see Fig. 2, portion AB in curve *3*) being determined by the rate of fusion of a particular area in the metallization strip. The complete fusion corresponds to a maximum potential jump, the magnitude of which is related to a difference of the electric conductivities between the solid (ρ_s) and liquid ($\rho_l = 2.2\rho_s$) aluminum [7]. The subsequent events manifested by a decay of the potential $U(t)$ correspond to the contact melting of Si in the liquid Al film. The process of a liquid phase formation caused by large j begins at certain "weak points" of the structure, which is clearly indicated by microscopic observations. Previously, we observed a discrete nucleation of melted zones, accompanied by a potential jump in Al–Si structures with high-ohmic amorphous semiconductor sublayers [4].

The switch-on oscillograms measured at a current density above 7×10^{10} A/m^2 (especially in multilayer structures) exhibit a strongly oscillating character in the sage of irreversible changes. Here, the $U(t)$ curves display jumps and drops of the potential against the background of a clearly pronounced tendency to decrease as a result of the contact melting of silicon. These oscillations are poorly reproduced, although the general trend is clearly manifested [4].

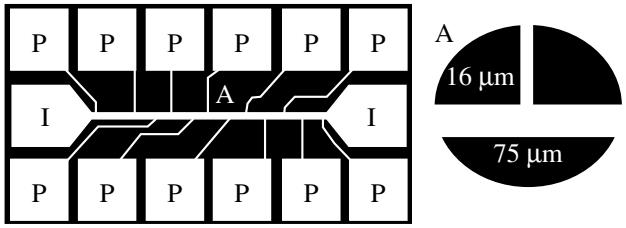

Fig. 1. A diagram of the test Al–Si structure bearing 12 potential (P) and two current (I) contact areas. The inset A shows a fragment of the test structure (magnification, ×21).

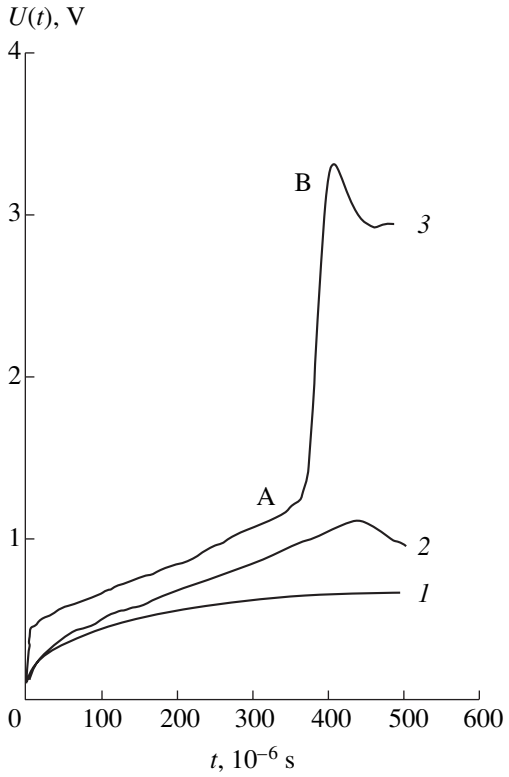

Fig. 2. Typical switch-on voltage oscillograms measured during the passage of a single rectangular current pulse with a duration of 500 μs and an amplitude of (*1*) 4.5×10^{10} A/m^2, (*2*) 5.0×10^{10} A/m^2 (contact melting without Al fusion), and (*3*) 5.6×10^{10} A/m^2 (contact melting with Al fusion). Potential electrodes spaced by 3.5 mm; aluminum; film thickness, 3 μm.

It was previously established [4] that this pattern of changes is related to numerous breaks in the deformed metal film and to the parallel process of merging of the fused zones under the action of electro- and thermotransfer forces. The random variation of the potential is determined by poor adhesion in multilayer systems and a pronounced random character of the formation of fused metal zones.

[2] By the critical current density j_k we imply the value at which irreversible damage (contact melting, fusion, breakage, etc.) takes place in the metallization layer and in the whole metal–semiconductor structure in the course of the current pulse passage.

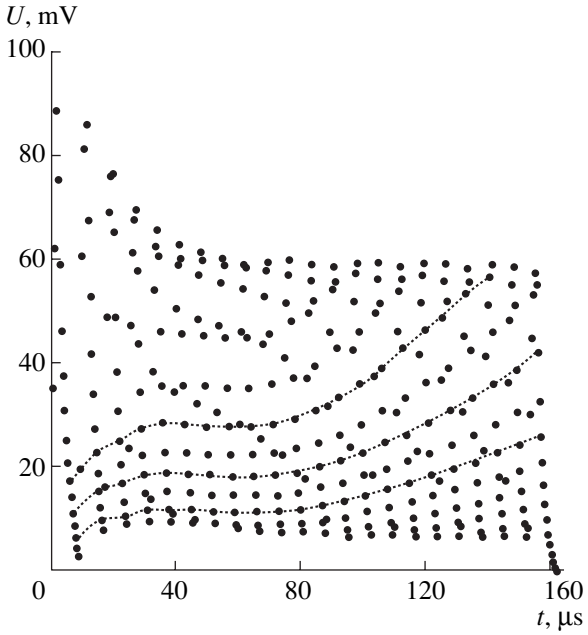

Fig. 3. A switch-on voltage oscillogram measured during the passage of a single rectangular current pulse with a duration of 160 μs and an amplitude of 6×10^{10} A/m^2.

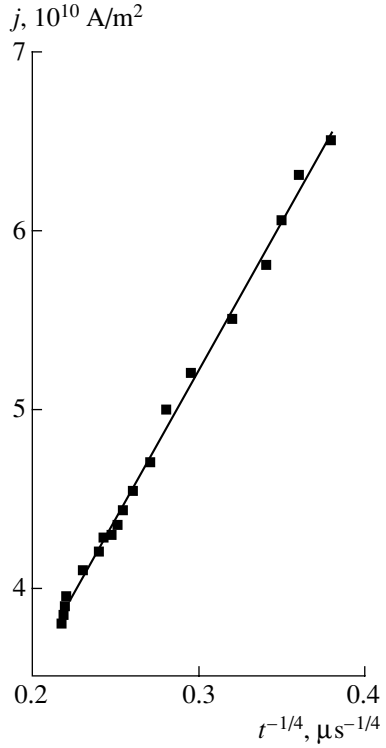

Fig. 4. A plot of the critical current density versus current pulse duration in the test Al–Si structure.

In contrast to the behavior of multilayer systems, the formation of local liquid regions in the Al–Si structures studied, which are characterized by a better adhesion of film to substrate, exhibits a more ordered character. In this case, variations of the oscillating potential take place at the same sites of the fused zone. This must lead to an ordered arrangement of the points of oscillating potential.

Indeed, the experimental oscillograms measured in the Al–Si structure after attaining the melting temperature of aluminum display the contribution from all local fusion zones (three such contributions are indicated by dashed lines connecting the points in Fig. 3). Moreover, the number of such dashed lines corresponds to the number of nucleated local zones in a given metallization region, from which the $U(t)$ signal is measured.

In practice, important information is provided by the values of the critical current densities leading to irreversible degradation processes. These values can be readily estimated using Eq. (2) by relating the degradation onset to the moment of the potential deviation from the parabolic growth of U (and, hence, of T):

$$j_c = \sqrt{\frac{(\Delta T)S\bar{C}d}{(bh)^2\bar{R}}}\sqrt[4]{\frac{\bar{a}}{\tau}}. \qquad (3)$$

As can be seen from this formula, the plot of the critical current density j_c versus the pulse duration must fit to a straight line in the coordinates of j_c versus $1/\sqrt[4]{\tau}$, in good agreement with experiment (Fig. 4). The higher the current density, the faster the onset of the test structure degradation.

By comparing the experimental data (Fig. 4) to Eq. (3), we may estimate the critical temperature T_c corresponding to the onset of irreversible changes at the Al–Si contact under the action of a pulsed electric current. The results of calculations showed that this temperature corresponds to the eutectic melting of the system components (T_c = 870 K). The calculations were performed using the following experimental temperature dependences of the parameters [8, 9]:

$$d = \frac{2328}{(1 + 7.5 \times 10^{-6}T)} \quad (\text{kg/m}^3),$$

$$C = 800 + 8 \times 10^{-2}T - 1.5 \times 10^3 T^{-2} \quad (\text{J/(kg K)}),$$

$$\lambda = 12 \times 10^4 T^{-1.2} \quad (\text{W/(m K)}),$$

$$\alpha = 4.3 \times 10^{-3} \quad (\text{K}^{-1}).$$

The thermal impact on the silicon surface favors the development of strong temperature gradients, which give rise to considerable mechanical stresses. This favors the formation of linear defects in the region of maximum gradients (~10^7 K/cm) even after the passage of a single current pulse with $j \sim 5 \times 10^{10}$ A/cm^2 and τ = 100 μs.

The results of our metallographic investigations showed the presence of dislocation etch pits on the sur-

face of silicon upon removal of the metallization layer. The aluminum film was removed by etching in orthophosphoric acid solution, while the dislocation etch pits on the exposed silicon were revealed by a standard CP etchant.

Thus, the degradation processes taking place in Al–Si structures under the action of strong current pulses are related to the intensive phase formation processes. The main stages in the development of this type of the heterostructure degradation are established. The results of oscillographic measurements allowed the stages of metal fusion and contact melting on the silicon surface to be separated and analyzed. The regions of the manifestation of these effects are determined. The initial stages of the metallization layer degradation are established at various current densities j interpreted as the critical degradation current densities. It was established that single current pulses with a duration of 100 μs and an amplitude of 5×10^{10} A/m^2 favor the formation of linear defects in the region of maximum temperature gradients. Some features in the manifestation of this effect need a special investigation, the results of which will be reported soon.

REFERENCES

1. K. A. Valiev, A. A. Orlikovskiĭ, A. G. Vasil'ev, and V. F. Lukichev, Mikroélektronika **19** (2), 116 (1990).
2. P. Burggraff, Solid State Technol. **43** (1), 63 (2000).
3. H. Wang and G. S. Fischman, J. Appl. Phys. **76** (3), 1557 (1994).
4. A. M. Orlov, B. M. Kostishko, A. A. Skvortsov, and A. V. Pirogov, Neorg. Mater. **32** (6), 277 (1996).
5. A. M. Orlov, A. A. Skvortsov, and B. M. Kostishko, Poverkhnost, No. 4, 64 (2000).
6. A. M. Orlov, A. V. Pirogov, and T. G. Emel'yanova, Neorg. Mater. **29** (11), 1559 (1993).
7. D. R. Wilson, *Structure of Liquid Metals and Alloys* (Metallurgiya, Moscow, 1972).
8. *Handbook on Electrotechnical Materials*, Ed. by Yu. V. Koretskiĭ, V. V. Pasynkov, and B. M. Tareev (Énergoatomizdat, Leningrad, 1988), Vol. 3.
9. A. S. Okhotin, A. S. Pushkarskiĭ, and V. V. Gorbachev, *Thermophysical Properties of Semiconductors* (Atomizdat, Moscow, 1972).

Translated by P. Pozdeev

Technical Physics Letters, Vol. 27, No. 10, 2001, pp. 838–840. Translated from Pis'ma v Zhurnal Tekhnicheskoĭ Fiziki, Vol. 27, No. 19, 2001, pp. 85–89.

Current Generation During the Interaction of a Supersonic Xenon Plasma Flow with a Magnetic Field

S. V. Bobashev[a], Yu. P. Golovachov[a], Yu. A. Kurakin[a], V. G. Maslennikov[a], V. A. Sakharov[a]*, K. Yu. Treskinskiĭ[a], A. A. Schmidt[b], and D. M. Van Wie[b]

[a] *Ioffe Physicotechnical Institute, Russian Academy of Sciences, St. Petersburg, 194021 Russia*
**e-mail@V.Sakharov@pop.ioffe.rssi.ru*
[b] *Johns Hopkins University, Laurel, Maryland, USA*
Received May 24, 2001

Abstract—The interaction of a supersonic pure xenon plasma flow at $M \sim 4.0$ with a magnetic field of $B \sim 1$ T was studied. The integral current passing in the plasma was measured depending on the initial ionization level. The experimental data are compared to the results of numerical modeling. © *2001 MAIK "Nauka/Interperiodica".*

The problem of controlling supersonic flows in low-temperature plasmas is actively discussed in relation to the prospects of creating a new generation of aircraft. In particular, one possibility is to control the air flow in the entrance device (air intake) of such a system. Several years ago, it was suggested that this problem can be solved by using the phenomenon of a magnetohydrodynamic (MHD) interaction between weakly ionized air and a magnetic field [1, 2]. Obviously, the solution to this task requires a complex approach combining fundamental investigations in many fields and the search for new technical solutions.

A complex experimental MHD setup for investigation of the interaction of supersonic flows of ionized gases with an external magnetic field was created based on the Big Shock Wave Tube [3] in the Laboratory of Physical Gasdynamics at the Ioffe Physicotechnical Institute (St. Petersburg). In this setup, a plasma flow is generated in the shock wave tube channel by heating gas with a reflected shock wave *1* (see Fig. 1). The shock wave tube operates in a regime with intermediate chamber, owing to which it is possible to hold a plasma at a temperature of up to $T \sim 10^4$ K and a pressure of up to $P \sim 5$ MPa for 1–1.5 ms. Then the ionized gas is accelerated in the supersonic nozzle *2* and directed to the working chamber *3* featuring the MHD interaction.

The working chamber is situated in the gap between two horizontal coils *4* spaced by 210 mm. The coils are a part of the system generating a pulsed magnetic field, also including a capacitor bank with a total capacitance of 30 mF, a 5-kV charging unit, a current switch, and a monitoring instrumentation. The half-period of the capacitor bank discharge is 4 ms. The maximum value of the magnetic induction at the center of the gap

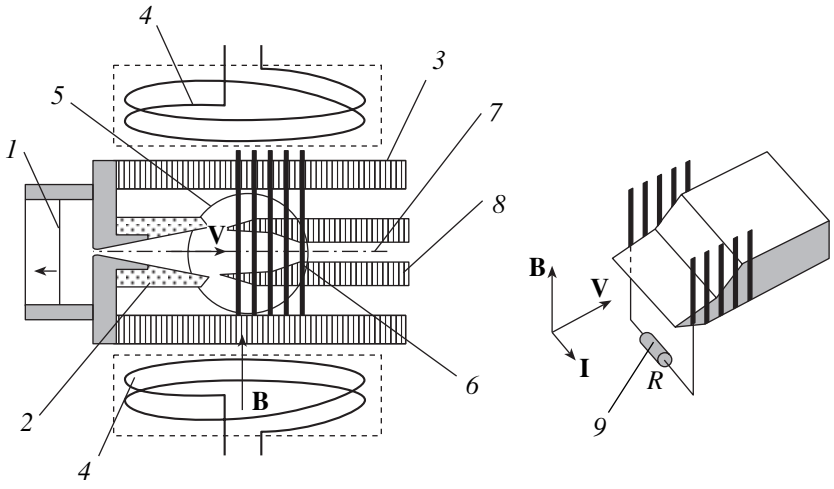

Fig. 1. Schematic diagrams of the working chamber and the measuring circuit (see the text for explanations).

1063-7850/01/2710-0838$21.00 © 2001 MAIK "Nauka/Interperiodica"

between coils is 1.5 T. The side walls of the working chamber bear a pair of optical windows *5* with a diameter of 140 mm, which are used for visualization of a gasdynamic pattern of the flow in the region of the MHD interaction with the aid of a special optical system.

In this study, the experiments were performed in a working medium representing a xenon plasma accelerated in a flat supersonic nozzle up to a Mach number of $M = 4.0$. The nozzle parameters are as follows: width, 75 mm; aperture angle, 22°; critical cross section, 10 mm; output cross section, 60 mm; supersonic part length, 130 mm. The MHD channel represents a dielectric chamber with a 75-mm-wide rectangular cross section accommodating a system of electrodes *6* mounted on the inner surface of the side walls and oriented perpendicularly to the nozzle axis of symmetry *7*. A double wedge *8* is situated near the exit edge of the nozzle, with the wedge surfaces forming angles of 10° and 20° with the nozzle wall.

In an analogous experiments carried out previously [4], we failed to generate a current in the plasma using only an external magnetic field. The reason was that the magnitude of a near-electrode potential fall exceeded the magnetic-field-induced emf. For compensating the near-electrode potential fall and creating a current sufficient for the MHD interaction, an external voltage source was connected to the electrodes. The magnetic-field-induced emf ε is equal to the product BVL, where B is the absolute value of the magnetic induction, V is the plasma velocity, and L is the interelectrode distance. Thus, the emf depends, in particular, on the electrode spacing L. In this study, we employed an MHD channel with $L = 70$ mm, which is 2.5 times the channel size used in [4].

The magnetic-field-induced current was monitored by measuring a voltage drop across resistor *9* with $R = 0.1\ \Omega$ between a pair of electrodes situated most closely to the nozzle. A distance from the nozzle entrance to the measuring cross section was 180 mm. The mutual orientation of the vectors of magnetic induction **B**, flow velocity **V**, and induced current **I** is illustrated in the Fig. 1.

The plasma parameters were modified by changing the shock wave intensity, which was achieved by varying the initial xenon pressure P_1 in the shock wave channel. The initial conditions, measured vales, and the results of a model calculation of the flow parameters are presented in the table below (during the measurements, the magnetic induction was maintained on a constant level of $B \sim 1$ T).

As can be seen from data in the table, a change in the flow regime (i.e., in the starting Mach number M_{s1}) virtually does not affect the magnetic-field-induced emf ε in the interelectrode gap. Therefore, we may suggest that, under the experimental conditions studied, the current in the working cross section is determined by the degree of gas ionization α. In Fig. 2, points show the

Initial experimental conditions and the results of experiments and model calculations

Regime	P_1, Torr	M_{s1}	U_m, V	ε, V
1	40	7.7	1	131
2	25	8.2	2	132
3	12	9.5	6	135

Note: P_1 is the initial xenon pressure in the low-pressure channel of the shock wave; M_{s1} is the Mach number of the incident shock wave; U_m is the voltage amplitude of resistor R.

experimental variation of the current amplitude I_m in the measuring circuit versus the degree of gas ionization α at the nozzle entrance, which was determined from calculations of the equilibrium ionization of Xe behind the shock wave.

We have numerically modeled the flow regimes presented in the table within the framework of the MHD approximation using a nonviscous gas model. The magnetic field was assumed to be constant and the electric field was determined via a loading coefficient using a formula for the Faraday generator with ideal sectioned electrodes. A system of equations was written for a two-temperature plasma with an allowance for the collision and ionization processes. The gasdynamic equations with additional electromagnetic terms were solved by a high-resolution finite-volume scheme of the Godunov type in combination with a two-layer implicit scheme used to take into account the nonequilibrium processes. The stationary solutions were found by a setting method. The numerical modeling procedure is described in detail elsewhere [5].

The solid curves in Fig. 2 connects the three points corresponding to the values of the integral current calculated in the working cross section for three regimes indicated in the table. These values correspond to the stationary flows featuring no changes in the current. However, an analysis of the signal measured on resistor R

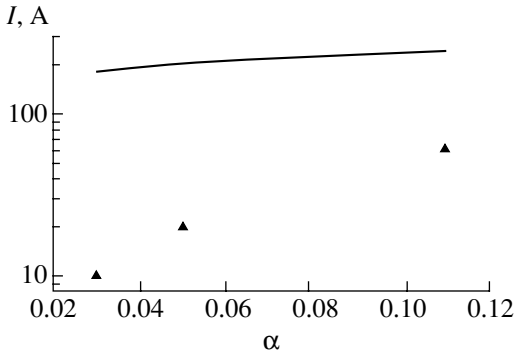

Fig. 2. The plot of current amplitude I in the measuring circuit versus degree of ionization α at the nozzle entrance.

during the experiment showed that a stationary current was not established in the circuit during the plasma efflux time (~500 μs). In other words, the current amplitude measured in the experiment does not correspond to the stationary flow conditions used in the model calculations. This is probably the main reason for the discrepancy between calculations and experiment. Another reason may be related to the fact that the calculation did not took into account processes in the near-electrode plasma layer and that the Faraday generator model with ideal sectioned electrodes is not quite adequate to the electrode system of a real experimental setup.

Acknowledgment. The authors are grateful to T.A. Lapushkina for her help in preparation of the experiment.

REFERENCES

1. E. P. Gurijanov and P. T. Harada, in *Proceedings of the 7th Aerospace Planes and Hypersonic Technology Conference, Norfolk, 1996*, AIAA Pap. **96-4609** (1996).
2. D. I. Brichkin, A. L. Kuranov, and E. G. Sheikin, in *Proceedings of the 8th International Space Planes and Hypersonic Systems and Technologies Conference, Norfolk, 1998*, AIAA Pap. **98-1642** (1998).
3. V. G. Maslennikov and V. A. Sakharov, Zh. Tekh. Fiz. **67** (11), 88 (1997) [Tech. Phys. **42**, 1322 (1997)].
4. S. V. Bobashev, R. V. Vasil'eva, E. A. D'yakonova, *et al.*, Pis'ma Zh. Tekh. Fiz. **27** (2), 63 (2001) [Tech. Phys. Lett. **27**, 71 (2001)].
5. Yu. P. Golovachov, Yu. A. Kurakin, A. A. Schmidt, *et al.*, AIAA Pap. **2001–2883** (2001).

Translated by P. Pozdeev

Technical Physics Letters, Vol. 27, No. 10, 2001, pp. 841–843. Translated from Pis'ma v Zhurnal Tekhnicheskoĭ Fiziki, Vol. 27, No. 19, 2001, pp. 90–94.

Modeling of the Synchrotron Diagnostics of Explosions

A. P. Ershov

Lavrent'ev Institute of Hydrodynamics, Siberian Division, Russian Academy of Sciences, Novosibirsk, Russia
e-mail: ers@hydro.nsc.ru

Received May 10, 2001

Abstract—Application of the synchrotron radiation (SR) to the diagnostics of explosions is considered. The interaction of an SR beam with a cylindrical charge of a detonating explosive is described within the framework of a one-dimensional hydrodynamic model. © *2001 MAIK "Nauka/Interperiodica".*

Introduction. Beginning in 2000, a new direction in the diagnostics of high-rate processes is developed based on the use of synchrotron radiation (SR). A high intensity, small angular divergence, and potentially large repetition frequency of the probing radiation pulses are obvious advantages of the SR diagnostics in comparison to the usual X-ray transillumination techniques. At the same time, the SR probing can be virtually nonperturbing. This combination of properties makes the SR diagnostics, probably, a most promising method for studying explosion and detonation processes. Although only some preliminary results have been reported (see, e.g. [1–3]), the importance of this problem justifies preliminary analysis of the possible applications of the SR diagnostics.

In experiments, an SR beam extracted from the undulator of a 2-GeV electron accelerator was normally incident onto a cylindrical charge of an explosive with a diameter of 1 cm. By measuring the beam absorption, it was possible to estimate the charge density. It was also possible to measure the radiation scattered at small angles from carbon (in particular, diamond) particles formed as a result of the explosion. The scattered signal exhibited a significantly sloped leading front (a few microseconds). At first glance, this contradicts the commonly accepted notions about a faster diamond formation during a detonation process (within a submicrosecond chemical reaction zone [4]). Based on the results of modeling of the interaction of an SR beam with a detonating charge, we propose an interpretation consistently combining new data with the concept of rapid particle formation.

Model description. The most important circumstance is that a carbon particle formed as a result of the explosion is immersed into a dense gas. This medium reduces the electron density contrast as the particle surface and, hence, decreases the scattering intensity. As the explosion products expand with a characteristic time on the order of a few microseconds, the gas density drops and the contrast (as well as the scattering signal) grows. This circumstance accounts for an important role of the expansion dynamics in the analysis of SR beam absorption.

The expansion gasdynamics was numerically calculated in a one-dimensional approximation. Although a one-dimensional model cannot give exact values of the medium density on the ray path, this approximation can be used for estimation purposes. It was assumed the Jouguet state was instantaneously established behind the detonation front, followed by the cylindrical expansion stage. The detonation products were assumed to obey the equation of state [5], and the surrounding air was considered as the ideal gas with the adiabatic exponent 1.25. A system of the Lagrange equations of motion was solved by the effective viscosity method [6].

The charge cross section was subdivided into concentric cells. Passed through such a cell, the beam intensity $I(r, t)$ decreased as reflected by the factor $\exp(-\mu\rho(r, t)|\Delta r|)$. Here, μ is the mass attenuation coefficient, $\rho(r, t)$ is the density, Δr is the increment of the Euler radius r (note that each cell is crossed by the beam two times).

The current beam intensity $I(r, t)$ generates scattering in the cell. In the experiment, the maximum photon energy was about 30 keV. For a characteristic particle size of $R \sim 4$ nm, the main maximum of the small-angle scattering function corresponds to the scattering angle on the order of 0.5°. Upon averaging over the ensemble of particles and the spectrum, this function yields a factor on the order of unity. The aforementioned immersion makes the scattered signal proportional to a square difference of the electron densities of particle and gas or, with a good precision, to the square difference of the mass densities of diamond (ρ_d) and gas (ρ_g); for elements entering into the composition of explosives, a deviation from the atomic number to mass ratio of 1/2 is observed only for hydrogen whose mass fraction is very small. The scattering intensity can be presented in the form convenient for comparison to the gasdynamic calculation:

$$\Delta I_S \sim I(r, t)\rho(r, t)(\alpha_d/\rho_d)(\rho_d - \rho_g)^2 R^3 \Delta r, \qquad (1)$$

1063-7850/01/2710-0841$21.00

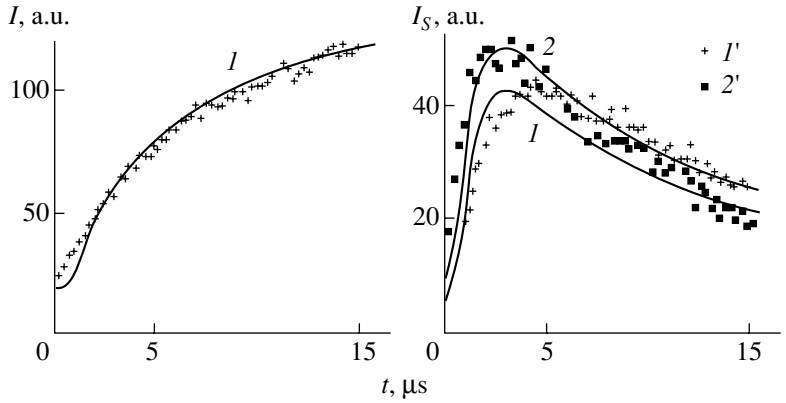

Time variation of the intensity of the transmitted (I) and scattered (I_S) SR beams. Points present the experimental data for (*1*') TNT and (*2*') TH 50/50 [2]; sold curves show the results of the model calculation for (*1*) TNT and (*2*) TH 50/50.

where α_d is the explosive mass fraction corresponding to the diamond phase. If the condensed product is not entirely diamond, this relationship can naturally be corrected.

Experimental limitations made it necessary to employ the entire radiation spectrum (white beam). The absorption is strongly dependent on the radiation wavelength. The rigid component is transmitted first; as the density decreases, the soft radiation component is also manifested and, hence, the polychromatic character of the radiation beam employed also affects the resolution characteristics.

The whole spectral energy range from 0 to 30 keV was divided into 20 equal parts. The calculations of absorption and scattering according to Eq. (1) were carried out separately in each energy interval. The initial radiation spectrum was taken from [7] (for a wiggler field strength of 2 T) and corrected for the absorption in air (on the path to the charge) and in the entrance beryllium window. Then the intensities of the transmitted $I(E)$ and scattered $I_S(E)$ beams in each cell of the charge were calculated for each beam component with an allowance for absorption of the scattered radiation. Finally, the absorption in air (on the path to the detector) and in the exit window was taken into account. The mass attenuation coefficients were interpolated using the tabulated data [8]. It was assumed that the detector signal is proportional to the radiation power integrated over the whole spectrum.

Results and discussion. A comparison of the results of the model calculation to the experimental data [2] for a pressed trinitrotoluene (TNT) charge with a density of 1.6 g/cm^3 and a cast 50% TNT–50% hexogen (TH) composition is presented in the figure. It was assumed that the beam traveled in air a distance of 1 m from source to charge and 50 cm from charge to detector. The initial beam intensity was matched to the experimental value. Note a good coincidence of calculated and experimental data for the transmitted beam.

The yields of condensed carbon and diamond, as well as the particle dimensions, were taken from [4]; the condensation process was assumed to be instantaneous. The scattering signal was determined according to Eq. (1) to within a constant factor and the maximum was matched to the experimental value for TNT. Despite a smaller amount of carbon, the intensity of scattering for TH is somewhat greater, in agreement with experiment. This is explained by a higher yield of diamond (producing a stronger scattering signal as compared to that of carbon).

The dynamics of scattering is reproduced only qualitatively. The calculated signal initially increases due to the growing contrast and then decays as a result of the general expansion (leading to a decrease in the amount of particles interacting with the beam). The maximum signal level is attained at approximately 3 μs for both explosives. In the TH experiment, the experimental growth is somewhat faster than calculated, while the TNT experiment lags significantly behind the calculation. In should be noted that the expansion stage in the model employed is somewhat retarded because we did not take into account the axial expansion of the detonation products. A two-dimensional model would provide for a faster buildup of the signal, which may explain the discrepancy with the TH experiment. However, the same correction would be expected for TNT (due to the close expansion gasdynamics in the two cases).

It was suggested [2] that condensation not only takes place in the chemical reaction zone but proceeds in the expanding detonation products as well. The above estimates show that the scattering signal increases for a few microseconds even assuming the "instantaneous" condensation of carbon. The delayed condensation might probably take place only for TNT, where the signal grows at a slower rate. This can be due to, for example, incomplete conversion, whereby the reaction continues and the carbon particles form on the background of expansion.

In contrast to the detonation diamonds, the graphite and amorphous carbon particles dominating in the TNT

detonation products were studied much less extensively. The variant of delayed condensation, implying the growth of coarser particles (up to tens nanometers in size), seems to be unlikely because of the size limitations [9]. Moreover, the signal from coarse particles is determined by the "tail" of the scattering profile (i.e., is roughly proportional to $1/R$) rather than by the first maximum; in this region of parameters, the signal growth implies a decrease in the particle size. Although coarse graphite-like particles were found in the retained product, the formation of this fraction is probably related to the action of high temperatures in the later stages of explosion.

It seems more likely that the observed phenomena are due to the constraint effect. The TNT detonation products are characterized by a very large concentration of free carbon. This leads to the formation of a spatial structure of fine graphite particles, which accounts for the high conductivity of such medium [9, 10]. In the course of expansion, the structure breaks with the formation of fresh surfaces that increase the scattering intensity. This possibility offers an alternative to the explanation proposed in [2].

In the monochromatic approximation (ignoring "development" of the beam spectrum), the time of the scattering signal buildup was twice as short (~1.5 μs). Therefore, the contributions of the immersion and the beam polychromaticity to the signal front sloping are approximately equal. Use of a monochromatic SR beam would sharply increase the quality of the transmitted signal independent of the contrast.

REFERENCES

1. B. P. Tolochko, I. L. Zhogin, O. V. Evdokov, *et al.*, in *Proceedings of the XIII All-Russia Conference on the Use of Synchrotron Radiation* (Inst. Yad. Fiz. Sib. Otd. Ross. Akad. Nauk, Novosibirsk, 2000), p. 53.
2. A. N. Aleshaev, P. I. Zubkov, G. N. Kulipanov, *et al.*, in *Proceedings of the XIII All-Russia Conference on the Use of Synchrotron Radiation* (Inst. Yad. Fiz. Sib. Otd. Ross. Akad. Nauk, Novosibirsk, 2000), p. 184.
3. P. I. Zubkov, L. A. Luk'yanchikov, V. M. Titov, *et al.*, in *Chemical Physics of Combustion and Explosion: Proceedings of the 12th Symposium on Combustion and Explosion* (Inst. Probl. Khim. Fiz. Ross. Akad. Nauk, Chernogolovka, 2000), p. 177.
4. V. M. Titov, V. F. Anisichkin, and I. Yu. Mal'kov, Fiz. Goreniya Vzryva **25** (3), 117 (1989).
5. V. F. Kuropatenko, Fiz. Goreniya Vzryva **25** (6), 112 (1989).
6. R. D. Richtmyer and K. W. Morton, *Difference Methods for Initial-Value Problems* (Interscience, New York, 1967; Mir, Moscow, 1972).
7. G. N. Kulipanov and A. N. Skrinskiĭ, Usp. Fiz. Nauk **122** (3), 369 (1977) [Sov. Phys. Usp. **20**, 559 (1977)].
8. *X-ray Technique: Handbook*, Ed. by V. V. Klyuev (Mashinostroenie, Moscow, 1980).
9. A. P. Ershov, A. L. Kupershtokh, and V. N. Kolomiĭchuk, Pis'ma Zh. Tekh. Fiz. **16** (3), 42 (1990) [Sov. Tech. Phys. Lett. **16**, 102 (1990)].
10. B. Hayes, in *Proceedings of the 4th International Symposium on Detonation, White Oak, 1965* (Office of Naval Research, Washington, 1967), ACR-126, p. 595.

Translated by P. Pozdeev

Technical Physics Letters, Vol. 27, No. 10, 2001, pp. 844–846. Translated from Pis'ma v Zhurnal Tekhnicheskoĭ Fiziki, Vol. 27, No. 20, 2001, pp. 1–6.

Calculating a Change in the Electron Work Function upon Cesium Adsorption on the (111)TiO_2 Surface

S. Yu. Davydov and I. V. Noskov

St. Petersburg State Electrotechnical University, St. Petersburg, Russia

Received May 14, 2001

Abstract—A simple model is proposed for calculating a change in the electron work function caused by the adsorption of Cs atoms on the (111) rutile surface. The model takes into account both the dipole–dipole repulsion of adatoms and the adlayer metallization at large coverages. The results of the calculation using this model agree well with the experimental data. © *2001 MAIK "Nauka/Interperiodica".*

The electron work function is one of the most important characteristics of any adsorption system [1, 2]. From the theoretical standpoint, the most interesting problem is to calculate a change $\Delta\phi$ in the work function related to an increase in the surface coverage with adsorbed atoms $\Theta = N_a/N_{ML}$, where N_a is the surface concentration of adatoms and N_{ML} is the surface concentration corresponding to a monolayer (ML) coverage. The results of such calculations allow us to judge on the character of interaction between atoms in the adsorption layer [3, 4].

In contrast to the case of adsorption of metal atoms on the surface of metals [2, 5], Group IV semiconductors, and A_3B_5 semiconductor compounds (see, e.g., [6] and references therein), the adsorption on metal oxide substrates has not been studied until quite recently [7, 8]. In this paper, we will analyze the experimental results of Grant and Campbell [9] on the electron work function of a (110) rutile surface and its change caused by the adsorption of Cs atoms.

The first point to be noted is that the $\Delta\phi(\Theta)$ curves obtained in [9, 10] exhibit, despite significant distinctions, generally the same character as the analogous curves observed for the adsorption of alkali metals on refractory metal substrates (cf. experimental data in [9, 10] and, e.g., those in [2, 5]). Therefore, it is natural to construct the first approximation based on the approach developed for calculating the $\Delta\phi(\Theta)$ curves for the adsorption of metals on metal [11–13] and semiconductor [14, 15] substrates.

The purpose of this study was to develop a phenomenological model for calculating the $\Delta\phi(\Theta)$ curves describing the adsorption of metals on metal oxides, in particular, for the $Cs/TiO_2(110)$ system. In this stage of the system description, we ignore details of the geometric structure of the adlayer and take into account only a change in the surface concentration of adatoms (i.e., adlayer density). At the same time, we will take into account that, as surface coverage Θ increases, the quasilevel of an adatom (broadened due the interaction with the substrate) smears so as to form a band as a result of both indirect [16] and direct interaction between adatoms [17]. This smearing can be described by introducing a Θ-dependent quasilevel halfwidth Γ:

$$\Gamma(\Theta) = \Gamma_0(1 + \gamma\Theta), \tag{1}$$

where Γ_0 is the quasilevel halfwidth of an isolated adatom [3, 4] and γ is a dimensionless coefficient. This approach to describing the quasilevel smearing into a band was previously employed in [18].[1]

Let us consider an atom with a single electron on the outer *s* shell. As a result of adsorption, leading to the possibility for the electron to ass from adatom to substrate (in our case, from Cs atom to Ti^{4+} ion), the *s* orbital occupancy *n* differs from unity and the adatom acquires a charge $Z = 1 - n$. Dependence of the *Z* value on the coverage Θ is described by the formula [11–13, 15]

$$Z(\Theta) = \frac{2}{\pi}\arctan\frac{\Omega - \xi\theta^{3/2}Z(\Theta)}{\Gamma(\Theta)},$$
$$\xi = 2e^2\lambda^2 N_{ML}^{3/2}A, \tag{2}$$

where Ω is the quasilevel energy of the adatom relative to the substrate Fermi level, ξ is the constant of the dipole–dipole repulsion between adatoms, 2λ is the surface dipole length, and $A \sim 10$ is a dimensionless coefficient weakly dependent on the adatom lattice geometry.

A change in the electron work function is determined by the formula [2, 11, 12]

$$\Delta\phi(\Theta) = -\Phi\Theta Z,$$
$$\Phi = 4\pi e^2 N_{ML}\lambda. \tag{3}$$

[1] On accepting the structureless adlayer model, we believe that the location of an adatom is random and assume that the quasilevel broadening is proportional to the first power of the coverage (for details, see [16]).

1063-7850/01/2710-0844$21.00 © 2001 MAIK "Nauka/Interperiodica"

At this point, it is necessary to specify the model parameters. For this purpose, we will use the experimental data from [9]. The λ value can be determined from the dipole moment $p = Z_0 e\lambda^2$ ($Z_0 \equiv Z(\Theta = 0)$) for $\Theta \longrightarrow 0$ [2]. Using the value $p = 6D$ for $\Theta = 0.1$, we obtain $Z_0\lambda = 1.25$ Å.

Assuming that

$$\Omega = \phi - I \tag{4}$$

and taking $I = 3.89$ eV for the ionization energy of Cs and $\phi = 5.30$ eV for the work function of the (110) rutile surface [20], we obtain $\Omega = 1.41$ eV. Substituting Eq. (4) into formula (2) with $\Theta = 0$ and taking $\Gamma_0 = 0.5$ eV, we obtain $Z_0 = 0.78$ and $\lambda = 1.60$ Å. Note that this λ value is not much greater than a halfsum of the ion radii r_i (see [20] of Cs^+ and Ti^{3+} (1.28 Å) and almost coincides with a halfsum of the ion radii of Cs^+ and O^{2-} (1.61 Å).

Taking 1 ML = 4×10^{14} cm^{-2} [9], we obtain estimates of the parameters $\xi = 5.87$ eV and $\Phi = 11.58$ eV. For $\Delta\phi_{ML} \equiv \Delta\phi(\Theta = 1) = -2.20$ eV [9] and a monolayer coverage, relationship (3) gives the adatom charge $Z_{ML} \equiv Z(\Theta = 1) = 0.19$. Then, Eq. (2) yields

$$\gamma = \frac{\Omega - \xi Z_{ML}}{\Gamma_0 \tan\left(\frac{\pi}{2} Z_{ML}\right)} - 1, \tag{5}$$

from which it follows that $\gamma = 1$.

The curve of $\Delta\phi(\Theta)$ calculated using the above model is presented in the figure in comparison to the experimental data from [9]. It should be noted that Grant and Campbell [9] draw a smooth curve through the experimental points denoted by crosses, considering the break at $\Theta \sim 0.5$ as an artifact; taking into account that the $\Delta\phi(\Theta)$ curve in [9] exhibits a pronounced minimum, the agreement between our calculation and that experiment can be considered as quite satisfactory.

Now let us discuss the numerical values adopted as the model parameters. Since the dipole length is quite reasonable (see above), it is also natural that the parameters ξ and Φ fall within standard limits (see, e.g., [20, 21]). Note that, within the framework of the commonly accepted model (employing Anderson's Hamiltonian [22, 23]) of the adsorption on metals, the halfwidth of the quasilevel of an isolated adatom is given by the formula $\Gamma_0 = \pi V^2 \rho_S$, where V is (in our case) the matrix element of interaction between the *s* orbital of adatom and the *d* orbital of titanium and ρ_S is the density of states of the substrate. The matrix element can be calculated using the method of Harrison [24] as $V \equiv V_{sd\sigma} = -3.16\hbar^2 r_d^{3/2}/m(2\lambda)^{7/2}$ (where m is the electron mass, $r_d = 0.99$ Å is the radius of the *d* state [25]); this yields $V = 0.89$ eV. Since we took $\Gamma_0 = 0.5$ eV and ρ_S can be represented as $\sim 1/W$, where W is the width of an adsorption-active band, the above values lead to an estimate of $W = 5$ eV, virtually coinciding with the width of the valence *d* band of TiO_2 [7, 8]. The value of $\gamma = 1$ also seems quite reasonable, leading to the estimates of $\Gamma_{ML} = 2\Gamma_0 = 1$ eV for a monolayer coverage ($\Theta = 1$).

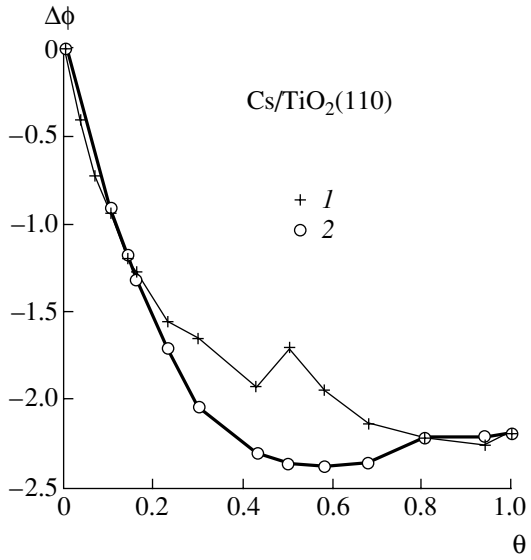

A change in the electron work function as a function of the adsorption coverage for the adsorption of Cs on TiO_2. Crosses *1* present the experimental data [9], solid curve *2* shows the results of calculations according to the proposed model.

Thus, we have demonstrated that a simple model with reasonable values of the parameters can be constructed within the framework of a standard approach of the adsorption on metals. The model adequately describes a change in the electron work function upon the adsorption of alkali metals on metal oxides.

Acknowledgments. This study was performed within the framework of the Federal Program "Surface Atomic Structures" (project no. 4.5.99).

REFERENCES

1. É. Ya. Zandberg and N. I. Ionov, *Surface Ionization* (Nauka, Moscow, 1969).
2. L. A. Bol'shov, A. P. Napartovich, A. G. Naumovets, and A. G. Fedorus, Usp. Fiz. Nauk **122** (1), 125 (1977) [Sov. Phys. Usp. **20**, 432 (1977)].
3. O. M. Braun, Ukr. Fiz. Zh. **23** (8), 1234 (1978).
4. O. M. Braun and V. K. Medvedev, Usp. Fiz. Nauk **157** (4), 631 (1989) [Sov. Phys. Usp. **32**, 328 (1989)].
5. *Physics and Chemistry of Alkali Metal Adsorption*, Ed. by H. P. Bonzel, A. M. Bradshow, and G. Ertl (Elsevier, Amsterdam, 1989).
6. G. P. Srivastava, Rep. Prog. Phys. **60** (5), 561 (1997).
7. V. E. Henrich and P. A. Cox, *The Surface Science of Metal Oxides* (Cambridge Univ. Press, Cambridge, 1994).

8. H.-J. Freund, H. Kuhlenbeck, and V. Staemmler, Rep. Prog. Phys. **59** (3), 283 (1996).
9. A. W. Grant and C. T. Campbell, Phys. Rev. B **55** (3), 1844 (1997).
10. M. Brause, S. Skordas, and V. Kempter, Surf. Sci. **445** (1-3), 224 (2000).
11. J. P. Muscat and D. M. Newns, J. Phys. C **7** (15), 2630 (1974).
12. S. Yu. Davydov, Fiz. Tverd. Tela (Leningrad) **19** (11), 3376 (1977) [Sov. Phys. Solid State **19**, 1971 (1977)].
13. S. Yu. Davydov, Fiz. Tverd. Tela (St. Petersburg) **41** (9), 1543 (1999) [Phys. Solid State **41**, 1413 (1999)].
14. T. Kato, K. Ohtomi, and M. Nakayama, Surf. Sci. **209** (1), 131 (1989).
15. S. Y. Davydov, Appl. Surf. Sci. **140** (1), 58 (1999).
16. S. Yu. Davydov, Fiz. Met. Metalloved. **47** (3), 481 (1979).
17. S. Yu. Davydov, Fiz. Tverd. Tela (Leningrad) **20** (6), 1752 (1978) [Sov. Phys. Solid State **20**, 1013 (1978)].
18. S. Y. Davydov, Surf. Sci. **407** (1-3), L652 (1998).
19. *Handbook of Physical Quantities*, Ed. by I. S. Grigoriev and E. Z. Meilikhov (Énergoizdat, Moscow, 1991; CRC Press, Boca Raton, 1997).
20. S. Yu. Davydov, Zh. Tekh. Fiz. **69** (5), 116 (1999) [Tech. Phys. **44**, 584 (1999)].
21. S. Yu. Davydov, Fiz. Tverd. Tela (St. Petersburg) **42** (6), 1129 (2000) [Phys. Solid State **42**, 1164 (2000)].
22. C. Kittel, *Quantum Theory of Solids* (Wiley, New York, 1963; Nauka, Moscow, 1967).
23. *Theory of Chemisorption*, Ed. by J. R. Smith (Springer-Verlag, Berlin, 1980; Mir, Moscow, 1983).
24. W. A. Harrison, *Electronic Structure and the Properties of Solids: The Physics of the Chemical Bond* (Freeman, San Francisco, 1980; Mir, Moscow, 1983), Vol. 2.
25. G. K. Straub and W. A. Harrison, Phys. Rev. B **31** (12), 7668 (1985).

Translated by P. Pozdeev

Technical Physics Letters, Vol. 27, No. 10, 2001, pp. 847–849. Translated from Pis'ma v Zhurnal Tekhnicheskoĭ Fiziki, Vol. 27, No. 20, 2001, pp. 7–13.

The Effect of Thermal Explosion in a Supercritical Water

A. A. Vostrikov, D. Yu. Dubov, and S. A. Psarov

Institute of Thermal Physics, Siberian Division, Russian Academy of Sciences, Novosibirsk, Russia
Novosibirsk State University, Novosibirsk, Russia
e-mail: vostrikov@itp.nsc.ru

Received April 16, 2001

Abstract—The conversion of hydrocarbons (eicosane, naphthalene, and synthetic bitumen) dissolved in supercritical water (SCW) was studied in a batch reactor at a pressure of P = 30 MPa and a range of temperatures from 450 to 750°C. It was established that water participates in the conversion process on a chemical level: in particular, oxygen from water molecules is involved in the formation of carbon oxides. Even in the absence of added molecular oxygen, the process of naphthalene and bitumen conversion in a certain temperature interval exhibited an exothermal character. Upon adding O_2 into SCW, the oxidation reaction may proceed in a burning regime with self-heating of the mixture. Under certain conditions, the self-heating process may lead to the thermal explosion effect accompanied by ejection of the substance from the reactor, which is explained by the high rate of hydrocarbon burning in SCW. © *2001 MAIK "Nauka/Interperiodica".*

Under conditions significantly beyond the critical pressures and temperatures (P = 22.1 MPa, T = 374°C), water is capable of dissolving unlimited amounts of weakly polar and nonpolar substances and oxygen [1]. This property of supercritical water (SCW) can be used for the partial burning of organic compounds and obtaining high-quality or harmless target products. However, this would require some additional basic knowledge, in particular, on the mechanisms, kinetics, and energetics of the chemical processes in SCW.

We have experimentally studied the partial oxidation of a series of "fuels," including eicosane ($C_{20}H_{42}$), naphthalene ($C_{10}H_8$), and a synthetic bitumen (C/H = 1 : 1.43), in pure SCW and in that containing O_2 additives. The fuels were supplied with the aid of a piston into a vertical cylindrical reactor preliminarily charged with SCW or an SCW–O_2 mixture. This procedure ensured rapid a (<1 s) mixing of the reagents. SCW was supplied from a prereactor with a volume of about 30 times the reactor volume, which ensured damping of the pressure jump in the reactor as a result of the fuel decomposition. After reacting with SCW for a certain time t (the time of stay in the reactor), the substance was discharged into a cryogenic separator and than transferred in portions via pipelines heated to 120°C into a receiver and a vacuum chamber. A flow of the gaseous reaction products entering into the vacuum chamber was converted into a molecular beam [2] that crossed an ionization source (ionizing electron beam) of a quadrupole mass spectrometer of the MS-7303 type. The nonvolatile reaction products were analyzed by conventional physicochemical methods [3].

Figure 1 shows plots of the relative amount N versus reaction temperature T for various reaction products determining the features of the fuel oxidation in SCW: methane (*1*, *1*'), carbon dioxide (*2*, *2*'), carbon monoxide (*3*, *3*'), molecular hydrogen (*4*, *4*'), water chemically formed and consumed in the reactions (*5*, *5*'), and residual fuels (*6*, *6*'). The N values were determined by dividing the amount of a given product by the amount of the initial fuel charged at a preset T and P = 30 MPa in SCW. Note that the products contained neither O_2 nor oxygen-containing substances other than those indicated in Fig. 1. The experimental conditions for Fig. 1 are as follows: (a) t = 300 s, mass ratio (MR) $H_2O : C_{20}H_{42} : O_2 = 1 : 0.5 : 0$; (b) t = 300 s, mass ratio $H_2O : C_{20}H_{42} : O_2 = 1 : 0.5 : 0.15$; (c) t = 600 s, mass ratio $H_2O : C_{10}H_8 : O_2 = 1 : 0.5 : 0.26$ or $H_2O : C_{10}H_8 : O_2 = 1 : 0.5 : 0$ (for some points at T = 710°C); (d) t = 600 s, mass ratio H_2O : bitumen : $O_2 = 1 : 0.3 : 0$ or H_2O : bitumen : $O_2 = 1 : 0.3 : 0.25$ (for dashed curves denoted by primed numbers). A change in the amount of water in each reaction was calculated proceeding from the balance of oxygen and hydrogen before and after reaction.

As can be seen from Fig. 1 (curves *5* and *5*'), water participates in the conversion of hydrocarbons on a chemical level: in particular, oxygen from water molecules is involved in the formation of carbon oxides (curves *2* and *3*), while hydrogen is involved in the hydrogenation of hydrocarbons and in the H_2 production. The latter conclusion follows from the analysis of hydrogen balance in the reaction products. The process of naphthalene decomposition begins (simultaneously with water decomposition) at $T \approx 600$°C (Fig. 1c). This is explained by the high thermodynamic stability of the aromatic molecules studied. Direct measurements of the eicosane and naphthalene residues in SCW without O_2 additives in the region of 75 s < t < 600 s and the temperatures T indicated in Figs. 1a and 1c allowed us to determine the corresponding decomposition rate

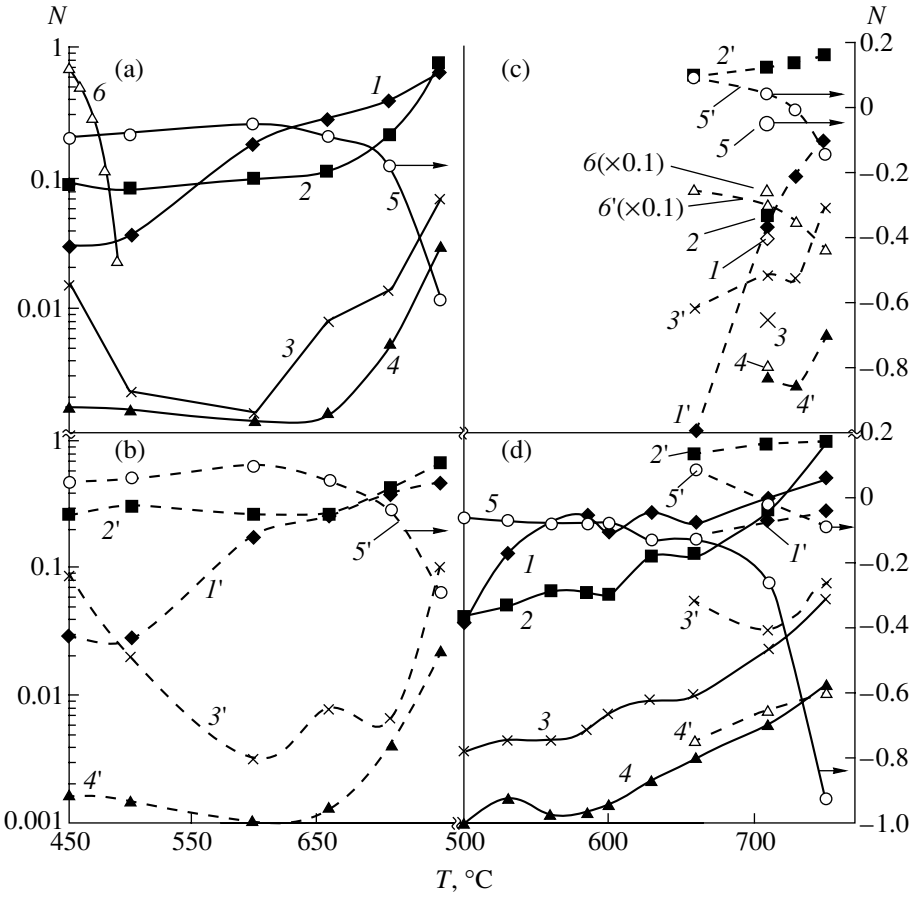

Fig. 1. Plots of the relative amount N versus reaction temperature T for some products of the conversion of (a, b) eicosane, (c) naphthalene, and (d) synthetic bitumen in supercritical water.

constants $k(T)$. According to [4], we expected to obtain a first-order kinetics and the Arrhenius relationship for $k(T)$: $dL/dt = -kL$, where L is the amount of fuel in SCW; $k(T) = A\exp(-E/T)$, where E is the activation energy. We obtained $k = 10^{16.5 \pm 0.5}\exp[-(32000 \pm 2000)/T]$ s^{-1} for eicosane and $k = 10^{12.3}\exp[-(35400/T]$ s^{-1} for naphthalene. Since bitumen is a mixture of hydrocarbons, the chemical interaction of water with bitumen and the gasification of bitumen are observed already at $T = 500$°C (Fig. 1d).

It should be noted that the composition of the products of hydrocarbon conversion in SCW depends on the C : H ratio in the initial fuel. The products of $C_{10}H_8$ conversion always contained soot, which was never observed in the experiments with $C_{20}H_{42}$ and bitumen. Adding oxygen did non change the qualitative composition of the volatile reaction products. However, the conversion of bitumen in a mixture of SCW with O_2 was accompanied by the formation of soot, the amount and composition (C : H ratio) of which depended on the amount of oxygen and the reaction temperature. The amount of metal oxides in the system was insignificant and did not affect the main conclusions.

Once the quantitative composition of the products of hydrocarbon conversion in SCW was known, we used the reference data [5, 6] and determined the thermal effect Q of the reactions studied. Figure 2 shows the plots of $Q(T)$ for eicosane (curves *7* and *7*'), naphthalene (point *8* and curve *8*'), and bitumen (points *9* and *9')* obtained for the same conditions as in Fig. 1. The primed numbers refer to the data for a mixture of SCW and O_2. As is seen, the hydrocarbon conversion can be exothermal even in the absence of molecular oxygen. This is a consequence of the fact that the heat consumed for the decomposition of molecules are compensated by the exothermal reactions of oxidation and hydrogenation by the O and H atoms of water. For example, in the exothermal reaction

$$C_iH_j + (i - j/4)H_2O = (i/2 - j/8)CO_2 + (i/2 + j/8)CH_4 + Q,$$

$Q = 246.2$ and 238.7 kJ/mol for eicosane and naphthalene, respectively.

Judging by the products of naphthalene conversion in SCW at $T = 660$°C, the thermal effect of this process

can be qualitatively described by the reactions

$$C_{10}H_8 + H_2O = C_6H_6 + CH_4 + CO + 0.2C_{10} + 10.6 \text{ kJ/mol},$$

$$CO + H_2O = CO_2 + H_2 + 24 \text{ kJ/mol}.$$

The ambiguous behavior of the $Q(T)$ curve for bitumen (Fig. 2, curve *8*) is explained by the complicated composition of this mixture of hydrocarbons. A sharp decrease in Q at $T = 750$°C observed for the conversion of eicosane and bitumen (Fig. 2, curves *7* and *9*) is explained by delayed hydrogenation (methanation) and accelerated H_2 production.

Adding molecular oxygen in to SCW significantly modifies the mechanisms and energetics of the hydrocarbon conversion processes. The former is clearly illustrated by the behavior of H_2O (curves *5* and *5*') and the C : H ratio in the hydrocarbon products. The latter is confirmed by the $Q(T)$ values (curves *7*, *7*'–*9*, *9*'). In the case of naphthalene conversion, oxygen completely oxidized a part of naphthalene to CO_2 and H_2O: $C_{10}H_8 + 12O_2 = 10CO_2 + 4H_2O + 5000$ kJ/mol. The amount of soot was independent of the O_2 content in SCW (the molar ratio $C_{10}H_8 : O_2$ was varied from 0 to 2.5), which indicates that soot was formed in the slower (compared to burning) process of naphthalene pyrolysis in SCW. The process of fuel burning at $T \geq 660$°C was so rapid that, under certain conditions (fuel injection time < 10 s, mass ratio H_2O : fuel : O_2 = 1 : 0.5 : 0.2 or above), the mixture exhibited self-heating in the reactor; sometimes this was even accompanied by ejection of substance from the reactor into prereactor. A small self-heating was monitored by a increase in the total (reactor plus prereactor) volume of the gaseous reaction products.

The ejection of substance from reactor was related to the effect of thermal explosion. Using the data [7] on the rate of benzene oxidation in an SCW–O_2 mixture (no such data are available for $C_{10}H_8$, $C_{20}H_{42}$, and bitumen), we determined for $T = 700$°C and the mass ratio $H_2O : C_6H_6 : O_2 = 1 : 0.5 : 0.2$ that 90% of O_2 would react for 2 s with the evolution of $Q = 5.3$ kJ per gram of C_6H_6. Taking into account the thermal losses thorough reactor walls and assuming that the valve between reactor and prereactor is closed, the temperature jump may reach up to $\Delta T \sim 670$°C and the pressure jump, up to $\Delta P \sim 21$ MPa. The results of the T calculation for SCW performed in an adiabatic approximation using the thermal parameters taken from [8] are depicted for the conversion of eicosane in Fig. 2 (curve *10*') (under the conditions corresponding to Fig. 1b, i.e., curve *7*' in Fig. 2). As can be seen, even a small O_2 additive to SCW may give rise to a significant temperature jump in the reactor.

Thus, in studying the conversion of organic substances in supercritical water under isothermal conditions, it is necessary to thoroughly control the amount and rate of heat evolution. Adding oxygen to SCW (e.g., for ensuring the autothermicity) requires great care, especially in the process initiation stage, in order to avoid the thermal explosion development that may lead to self-oscillation of the process parameters and even to the system failure. We are planing to study these processes in more detail.

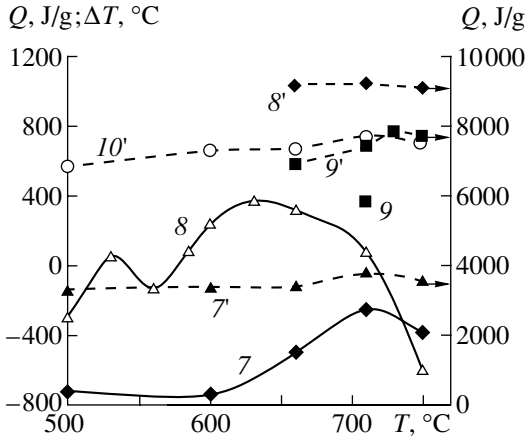

Fig. 2. Plots of the thermal effect Q and temperature jump ΔT (curve *10*') versus reaction temperature for the conversion of (*7*, *7*', *10*') eicosane, (*8*, *8*') naphthalene, and (*9*, *9*') synthetic bitumen in supercritical water.

Acknowledgments. This study was supported by a a grant from the Ministry of Education of the Russian Federation, project no. 3H-119-01.

REFERENCES

1. P. E. Savage, S. Gopalan, T. I. Mizan, *et al.*, AIChE J. **41** (7), 1723 (1995).
2. A. A. Vostrikov, D. Yu. Dubov, and I. V. Samoĭlov, Zh. Tekh. Fiz. **64** (12), 120 (1994) [Tech. Phys. **39**, 1267 (1994)].
3. A. A. Vostrikov, D. Yu. Dubov, and S. A. Psarov, in *Petroleum and Gas Chemistry* (STT, Tomsk, 2000), Vol. 2, pp. 492–496.
4. J. Yu and S. Eser, Ind. Eng. Chem. Res. **36** (3), 585 (1997).
5. *Physicochemical Properties of Individual Hydrocarbons*, Ed. by V. M. Tatevskiĭ (Gostoptekhizdat, Moscow, 1960).
6. *Thermodynamical Properties of Individual Substances: Reference Edition*, Ed. by V. P. Glushko (Nauka, Moscow, 1978), Vol. 2, Part 2.
7. J. L. DiNaro, J. W. Tester, and J. B. Howard, React., Kinet., Catal. **46** (11), 2274 (2000).
8. M. P. Vukalovich, *Tables of Thermodynamical Properties of Water and Water Vapor* (Énergiya, Moscow, 1965).

Translated by P. Pozdeev

Technical Physics Letters, Vol. 27, No. 10, 2001, pp. 850–851. Translated from Pis'ma v Zhurnal Tekhnicheskoĭ Fiziki, Vol. 27, No. 20, 2001, pp. 14–19.

The Effect of a Magnetic Field on the Kinetics of Melting of Ionic Crystals

L. A. Bityutskaya, E. S. Mashkina, and I. Yu. Butusov

Voronezh State University, Voronezh, Russia

e-mail: phme22-1@main.vsu.ru

Received April 20, 2001

Abstract—The kinetics of melting of an ionic crystal treated in a pulsed magnetic field ($H \sim 10^6$ A/m) was studied by a computer-aided DTA technique. Significant changes in the nonequilibrium thermodynamic parameters of transient processes during melting and in the enthalpy of melting were observed for KCl crystals, which is evidence that the magnetic field induces a special nonequilibrium state in these nonmagnetic crystals. © *2001 MAIK "Nauka/Interperiodica".*

The results of our investigation of the kinetics of KCl melting by DTA measurements above and below the melting temperature (T_m) showed the presence of cooperative transient processes different from the effect of fusion as such [1–3]. These effects, considered as representing a new class of universality in the kinetic phase transitions involved in the real melting of both ionic crystals and the crystals possessing other types of chemical bonds, are characterized by a system of experimentally measured thermodynamic parameters J [3, 4].

There is much reported on the effects of constant and pulsed magnetic fields on the real structure and physical properties of crystals [5–8]. Under this action, the ionic crystals exhibit a number of macroscopic phenomena, such as the magnetoplastic effect, induced luminescence, and a change in the mechanical properties [5, 6]. Showing a nonequilibrium character, these phenomena are retained even upon prolonged high-temperature annealing and possess, according to [5, 7], a spin-dependent nature. All this gives grounds for studying the effect of magnetic fields on the real melting, including both transient processes and the effect of fusion as such.

The purpose of this work was to study the kinetics of melting of KCl crystals treated in a pulsed magnetic field. The melting kinetics was studied by computer-aided DTA using a procedure described elsewhere [2–4]. The thermal measurements were conducted in evacuated quartz Stepanov vessels heated at a rate of $v = 5$ or 10 K/min. The experiments were performed with 2-g samples of crystalline KCl (reagent grade, doubly recrystallized).

A pulsed magnetic field (PMF) was generated by a solenoid [9]; the pulses had a semisinusoidal shape with an amplitude of $H \sim 10^6$ A/m and a duration of 30 μs. The treatment was performed at a pulse repetition rate of 50 Hz for $t = 30$ s. The samples were treated and stored prior to measurements at room temperature. The DTA measurements were conducted in the sequential and cyclic regimes. In the sequential experiment, four independent series of samples were measured 24, 48, 72, and 96 h after treatment in the magnetic field. The cyclic measurements were carried out on the same sample, which was measured daily over a period of five days after the PMF treatment. Prior to the PMF treatment, each sample was characterized by the initial pre- and postmelting parameters.

The sequential DTA measurements showed that the PMF treatment has a latent character, with the maximum effect manifestations observed 72 h after pretreatment. It is important to note that significant variations of the characteristic pre- and postmelting J values are related to a radical change in a basic parameter such as the enthalpy of melting at a virtually constant melting temperature (Figs. 1 and 2).

Upon the PMF treatment, the pre- and postmelting transient processes in KCl show (in comparison to the initial characteristics) a significant increase in their temperature–time interval, smearing of the heat pulse front, and a change in the frequency spectrum of the dissipation heat fluctuations. Figure 1 presents typical pre- and postmelting DTA curves for KCl crystals measured 72 h after PMF treatment, in comparison to those for the initial sample. As can be seen, the initial transient states are retained after the PMF treatment, but the pre- and postmelting heat pulses are significantly modified. The dissipation heat fluctuations become more inhomogeneous and increase in amplitude. In contrast to the untreated crystalline KCl, the transient excited premelting states appear at a premelting onset temperature ($T'_{\text{pre-m}}$) that is 70–100 K lower than that for the initial sample, while the transient excited postmelting states appear at a postmelting onset temperature ($T'_{\text{post-m}}$) that is 7–10 K higher than that for the untreated sample.

Figure 2 illustrates changes in the shape and area of the DTA peaks of melting which were observed in the course of storage of a KCl sample after pretreatment. A

1063-7850/01/2710-0850$21.00 © 2001 MAIK "Nauka/Interperiodica"

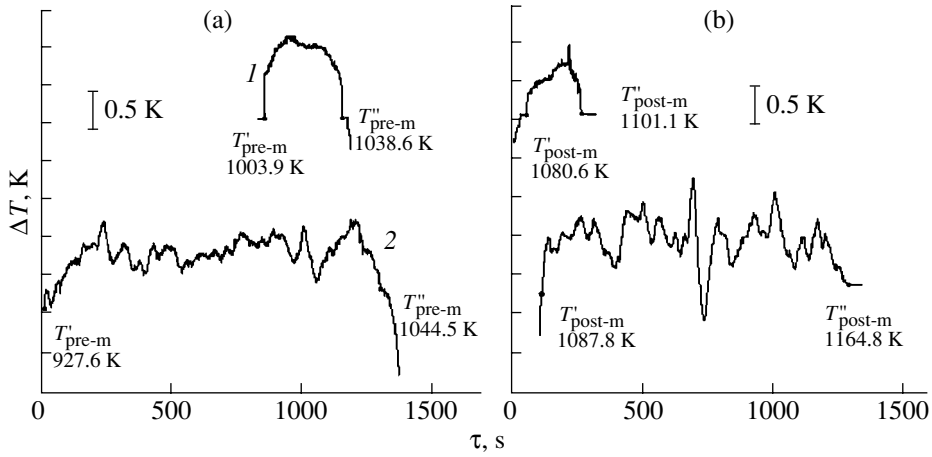

Fig. 1. Typical (a) pre- and (b) postmelting DTA curves for KCl crystals (m = 2g, v = 5 K/min) measured (*1*) before and (*2*) 72 h after PMF treatment ($H \sim 10^6$ A/m, t = 30 s).

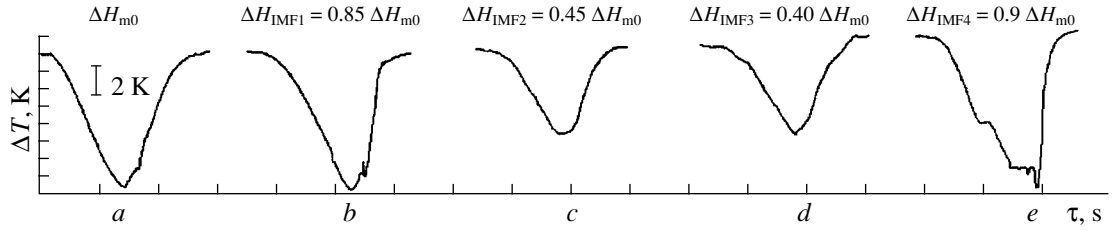

Fig. 2. Evolution of the shape and area of the DTA peaks of KCl melting measured during storage after the PMF treatment ($H \sim 10^6$ A/m, t = 30 s): *a*, initial; *b*, 24 h; *c*, 48 h; *d*, 72 h; *e*, 96 h.

change in the area under the melting peak for the samples after PMF treatment was determined relative to the initial value (S_0): $S_{IMF}/S_0 = \Delta H_{IMF}/\Delta H_{m0}$. The area under the peak was calculated using a trapezoid formula. A significant change in the enthalpy of melting was observed beginning with the second day after the PMF treatment. The relative change in the enthalpy exhibits an extremum ($\Delta H_{IMF}/\Delta H_{m0} \sim 0.4$) 72 h after the treatment. Beginning on the fourth day of the observation, the enthalpy of melting exhibits relaxation. In this stage, the peak acquires a complicated shape, with additional effects manifested on the smooth melting background. In the general case, the relaxation exhibits a long-term character, with a certain "memory" of the PMF treatment retained even on the 10th day after the PMF treatment.

The cyclic DTA measurements showed that the effect of the PMF treatment on the KCl melting kinetics is the same as that observed in the sequential experiment, with a minimum $\Delta H_{IMF}/\Delta H_{m0}$ value of ~0.4 reached 72 h after the treatment and the relaxation beginning on the fourth to fifth day of observation.

Thus, the PMF treatment of KCl crystals at room temperature induces the formation of a thermodynamically nonequilibrium mesophase in the sample. The melting kinetics of this mesophase shows the following characteristic features: (i) latent character; (ii) variation of the transient process parameters on melting; (iii) a significant decrease in the enthalpy of melting at a virtually constant T_m; (iv) long-term relaxation of the mesophase to the initial state; (v) "memory" of the PMF treatment retained after heating above T_m.

Acknowledgments. This study was supported by the Russian Foundation for Basic Research, project no. 01-03-32848.

REFERENCES

1. L. A. Bityutskaya and E. S. Mashkina, Pis'ma Zh. Tekh. Fiz. **21** (18), 85 (1995) [Tech. Phys. Lett. **21**, 763 (1995)].
2. L. A. Bityutskaya and E. S. Mashkina, Zh. Fiz. Khim. **74** (7), 1189 (2000).
3. L. A. Bityutskaya and E. S. Mashkina, Zh. Tekh. Fiz. **69** (12), 57 (1999) [Tech. Phys. **44**, 1449 (1999)].
4. L. A. Bityutskaya and E. S. Mashkina, Phase Transit. **71**, 317 (2000).
5. V. I. Al'shits, E. V. Darinskaya, and O. L. Kazakova, Zh. Éksp. Teor. Fiz. **111** (2), 615 (1997) [JETP **84**, 338 (1997)].
6. Yu. I. Golovin and R. B. Morgunov, Zh. Éksp. Teor. Fiz. **115** (2), 605 (1999) [JETP **88**, 332 (1999)].
7. M. I. Molotskiĭ, Fiz. Tverd. Tela (Leningrad) **33** (10), 3112 (1991) [Sov. Phys. Solid State **33**, 1760 (1991)].
8. M. N. Levin and B. A. Zon, Zh. Éksp. Teor. Fiz. **111** (4), 1373 (1997) [JETP **84**, 760 (1997)].
9. V. I. Chechernikov, *Magnetic Measurements* (Mosk. Gos. Univ., Moscow, 1969).

Translated by P. Pozdeev

Technical Physics Letters, Vol. 27, No. 10, 2001, pp. 852–854. Translated from Pis'ma v Zhurnal Tekhnicheskoĭ Fiziki, Vol. 27, No. 20, 2001, pp. 20–24.

A Study of the Zirconium–Oxygen Interaction in Silicon

T. S. Pchelintseva*, V. K. Prokof'eva, V. V. Svetukhin, A. S. Ambrozevich, B. N. Rygalin, and L. N. Lysenko

Ul'yanovsk State University, Ul'yanovsk, Russia;
Moscow State University of Electronic Technology, Moscow, Russia
** e-mail: slava@sv.uven.ru*

Received May 31, 2001

Abstract—The energy levels created by zirconium in silicon (0.65, 0.52, and 0.32 eV) were determined from the photoconductivity data. The oxygen solubility in zirconium-doped silicon was studied. It was established that zirconium affects the solubility of interstitial oxygen. *© 2001 MAIK "Nauka/Interperiodica".*

The efficiency and reliability of integrated circuits (especially of the VLSI type) depend on the quality of an internal oxygen getter formed in the silicon substrate. It was established that the best gettering layer (autogetter) is obtained when the atomic concentration of oxygen in a silicon wafer falls within a narrow interval $(7–9) \times 10^{17}$ cm^{-3} and deviates from this interval by no more than 10% over the cross section [1]. Usually, the oxygen concentration varies along the length of a silicon single crystal ingot from 1.8×10^{18} cm^{-3} at the beginning to $(5–6) \times 10^{17}$ cm^{-3} at the end. Therefore, no effective gettering band can be formed in the wafers cut from most of such an ingot. By doping silicon with zirconium (Zr), it is possible to provide for a uniform distribution of oxygen in both length and cross section of a single crystal ingot.

Lemke [2] studied the electrical properties of zirconium and revealed three electron levels with close energies. Numerous investigations devoted to the behavior of oxygen in silicon showed that the influence of this impurity on the properties of the crystal matrix is determined by the concentration and by the character of thermal treatment (prehistory) of single crystal wafers. Therefore, it is necessary to develop a detailed procedure for the preparation of silicon substrates with controlled oxygen content. The main purpose is to establish the optimum concentration of oxygen and find the most favorable regimes of thermal annealing for a given base material.

Silicon single crystal ingots of the KDB-12 grade with a diameter of 100 mm were grown by the Czochralski method from a silicon melt with zirconium at an atomic concentration from 5×10^{18} to 5×10^{19} cm^{-3}. As is known, dopants are nonuniformly distributed along the length of ingots grown by this method. The average content of zirconium atoms in our silicon crystals was 10^{16} cm^{-3}, while the local concentration gradually increased from the beginning to the end of the ingot. For this reason, we separated the ingots into four parts and studied the wafers cut from each part.

The sample wafers were studied by method of photoconductivity. The photoconductivity peaks in zirconium-doped silicon were observed at 0.32, 0.52, and 0.65 eV. Measurements of the temperature variation of the conductivity showed the electron energy levels at 0.51 and 0.15 eV. These results agree with the data obtained by the deep transient level spectroscopy [2], which revealed the levels at $E_c - 0.14$ eV, $E_c - 0.41$ eV, and $E_v + 0.32$ eV in silicon single crystals grown by a crucibleless floating zone technique.

The concentration of interstitial oxygen is usually determined by a method based on the optical absorption measurements at a wavelength of 1106 cm^{-1}. The oxygen content is calculated from the differential absorption data using the formula [1]

$$N_{ox} = K(\alpha_1 - \alpha_2),\ \text{cm}^{-3}, \quad (1)$$

where α_1 and α_2 are the absorption coefficients at 1106 cm^{-1} measured in the doped and oxygen-free silicon, respectively, and $K = 2.45 \times 10^{17}$ cm^{-2}.

The concentration of interstitial oxygen in silicon wafers is frequently monitored using "asymmetric" samples with only one side polished. In addition, measurements of the oxygen content in such wafers must take into account the effect of multiple internal light reflection in the crystal volume.

The optical transmittance of silicon at 1106 cm^{-1} (for the normal light incidence onto the polished wafer side) and the reflectances R_1 and R_2 (for a light incidence angle of $\gamma = 70°$ on the polished and rough sides, respectively) were measured with a Specord M-80

spectrophotometer (Germany). These reflection coefficients can be expressed trough the absorption coefficient α and the reflection coefficients r_1 and r_2 by the formulas

$$R_1 = \frac{r_1[1 - r_1 r_2 \exp(-2\alpha d) + (1 - r_1)^2 r_2]\sqrt{1 - \frac{1}{n^2}\sin^2\gamma}\exp(-2\alpha d)}{1 - r_1 r_2 \exp(-2\alpha d)}, \quad (2)$$

$$R_2 = \frac{r_2[1 - r_1 r_2 \exp(-2\alpha d) + (1 - r_2)^2 r_1]\sqrt{1 - \frac{1}{n^2}\sin^2\gamma}\exp(-2\alpha d)}{1 - r_1 r_2 \exp(-2\alpha d)}, \quad (3)$$

$$T = \frac{(1 - r_1)(1 - r_2)\exp(-\alpha d)}{1 - r_1 r_2 \exp(-2\alpha d)}, \quad (4)$$

where d is the silicon wafer thickness. Equations (2)–(4) were derived with an allowance for the multiple reflection of light from the internal surfaces.

By numerically solving the system of Eqs. (2)–(4), it is possible to determine the absorption coefficient at 1106 cm^{-1} with a good precision, taking into account both the multiple internal reflection and the different sample surface finish. Using these data, the interstitial oxygen concentration can be calculated by formula (1). With neglect of the multiple internal reflection effect, the error of determination of the reflection coefficients for a silicon wafer with a thickness of d = 500 μm is about 10%.

Possessing a large covalent radius, zirconium atoms create considerable internal stresses in silicon [3] that may affect the solubility of oxygen. Using the method described above, we determined the oxygen content in the wafers cut from various parts of the single crystal ingot. The results are presented in the figure, where the error bars reflect the inhomogeneous radial distribution of oxygen in the wafers. It was established that the concentration of zirconium grows and the oxygen content drops from the beginning to the end of the ingot. In the undoped (zirconium-free) silicon wafers, the atomic concentration of oxygen amounts to (1.2–0.7) × 10^{18} cm^{-3}. In the zirconium-doped samples, the content of oxygen decreased to (0.85–0.65) × 10^{18} cm^{-3}.

A decrease in the oxygen solubility may be caused by the elastic stresses created by zirconium atoms in the silicon lattice. As is known, the solubility of oxygen in silicon is described by the relationship

$$N_{ox} = A\exp\left(-\frac{H}{kT}\right), \quad (5)$$

where H is the enthalpy of dissolution. We can suggest that the elastic stresses lead to an increase in the enthalpy:

$$H' = H + \Omega. \quad (6)$$

Here, the quantity Ω describes interaction of the ensemble of zirconium atoms with an oxygen atom. Under the modified conditions, formula (5) transforms to

$$N_{ox(Zr)} = A\exp\left(-\frac{H'}{kT}\right). \quad (7)$$

Combining formulas (6) and (7), we obtain

$$\frac{N_{ox(Zr)}}{N_{ox}} = \exp\left(-\frac{\Omega}{kT}\right). \quad (8)$$

Using this relationship, the constant characterizing the elastic interaction of zirconium and oxygen was found to vary from 0.025 eV at the beginning to 0.058 eV at the end of the ingot.

Thus, we have developed a method for determining the concentration of interstitial oxygen in silicon

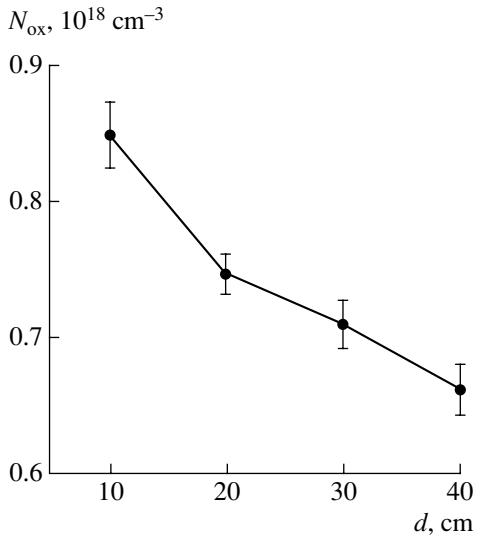

Variation of the atomic concentration of oxygen along the length of a Czochralski-grown zirconium-doped silicon ingot.

wafers from the results of optical measurements, with an allowance for the multiple internal reflection and the different sample surface finish. Investigation of the oxygen solubility in zirconium-doped silicon showed that the concentration of oxygen is affected by the level of doping. It is suggested that this effect is related to the elastic stresses developed by zirconium atoms in the silicon crystal lattice. The energy levels created by zirconium in silicon were determined from the photoconductivity data.

REFERENCES

1. V. M. Babich, N. I. Bletskan, and E. F. Venger, *Oxygen in Silicon Single Crystals* (Interpress LTD, Kiev, 1997).
2. H. Lemke, Phys. Status Solidi A **122**, 617 (1990).
3. E. B. Sokolov, V. K. Prokof'eva, and E. V. Belyanina, Izv. Vyssh. Uchebn. Zaved., Tsvetn. Metall., No. 6, 69 (1996).

Translated by P. Pozdeev

Technical Physics Letters, Vol. 27, No. 10, 2001, pp. 855–856. Translated from Pis'ma v Zhurnal Tekhnicheskoĭ Fiziki, Vol. 27, No. 20, 2001, pp. 25–28.

The Lower-Boundary Asymptotics of Continuous Spectrum for Quantum Layers Laterally Coupled by a Periodic System of Small Windows

I. Yu. Popov

Institute of Fine Mechanics and Optics (Technical University), St. Petersburg, Russia

Received April 24, 2001

Abstract—Asymptotics of the lower boundary of continuous spectrum is determined for quantum layers coupled by a periodic system of small windows. © *2001 MAIK "Nauka/Interperiodica".*

The development of nanoelectronics has led to the appearance of a new class of objects, including quantum dots, waveguides, and layers, using which it is possible to create basically new electronic devices (see, e.g., [1]). In order to describe the functioning of such devices, it is necessary to study the transport of electrons in the above quantum structures. This, in turn, implies the investigation of spectral properties of the corresponding quantum-mechanical operator. In recent years, considerable attention was paid to the study of coupled quantum layers [2] treated as mesoscopic systems—small so as to make it necessary to describe electrons as quantum objects but, on the other hand, sufficiently large to consider these electrons as moving in an average field, not separating their interaction with individual atoms.

This study is devoted to description of the quantum layers $\Omega_\pm = \{(x_1, x_2, x_3) \in \mathbf{R}^2 \times [0, \pm d_\pm]\}$ coupled by a periodic system of small windows. The case of one window ω_a representing an aperture with the diameter $2a$ ($\omega_a = a\omega$) was considered in [3]. It was demonstrated that a Laplacian obeying the Dirichlet condition possesses a bound state λ_a close to the boundary of continuum, for which the following estimates were obtained for sufficiently small a and $d_+ \geq d_-$:

$$e^{-c_1 a^{-3}} \leq \frac{\pi^2}{d_+^2} - \lambda_a \leq e^{-c_2 a^{-3}}, \qquad (1)$$

where c_1 and c_2 are some constant factors.

Below, we will consider the case of quantum layers coupled by a periodic chain and a periodic lattice of windows. The system is described using the method of matching of the asymptotic expansions of solutions to boundary problems [4, 5]. A variant of this method for the eigenvalues close to the boundary of continuum was developed previously [6–10].

First, consider a periodic chain of the coupling windows. Let $\Lambda_1 = \{x, x = (qL, 0, 0), q \in Z\}$ be the corresponding Bravais lattice with an elementary cell containing only one window center ($\omega_i^a = a\omega_i$, $\omega_{0,i} = \omega_i$). By virtue of the periodicity, the corresponding solution ψ_a obeys the Bloch condition: $\psi_a(x + L) = e^{i\theta L}\psi_a(x)$, where θ is the quasimomentum ($-\pi L^{-1} \leq \theta \leq \pi L^{-1}$). For a fixed quasimomentum, the system possesses the eigenvalue λ_a^θ. Our purpose is to find an asymptotic for this eigenvalue and then determine the zone parameters by varying θ. The asymptotic expansion for some function f_{Λ_1} of $\lambda_a^\theta = k_{a,\theta}^2$ is obtained in the following form:

$$f_{\Lambda_1}(k_{a,\theta}) = L\sqrt{\pi^2 - k_{a,\theta}^2 d_+^2 + \theta^2 d_+^2} = k_3^\theta a^3 + o(a^3). \quad (2)$$

The asymptotic expansion of the corresponding eigenfunction is as follows:

$$\psi_a(x) = \pm f_{\Lambda_1}(k_{a,\theta}) \times \sum_{j=0}^{\infty}\sum_{q=-\infty}^{\infty} a^j (P_{p+1}^{q,j}(D_y) G^\pm(x, y, k_{a,\theta}))\big|_{y=z^q}, \qquad (3)$$

$$x \in \Omega^\pm \backslash U_q S_{a^{1/2}}^q,$$

$$\psi_a(x) = \sum_{j=1}^{\infty} v_j^q(x/a) a^j, \quad x \in S_{2a^{1/2}}^q, \qquad (4)$$

where $P_1^{q,j}(D_y) = \alpha_q^j \dfrac{\partial}{\partial n_y}$ (the Bloch condition leads to the relationship $\alpha_q^j = e^{i\theta L q}\alpha_0^j$) and $G^\pm(x, y, k_{a,\theta})$ is the Green function for the layer $\Omega^\pm$. Using the procedure of matching of the asymptotic expansions, we obtain asymptotics of the zone boundary. It appears that, provided a is sufficiently small, the solution has no gap and

the lower boundary of continuous spectrum of the Dirichlet Laplacian exhibits the following asymptotics:

$$\lambda_{\min,a} = \begin{cases} \frac{\pi^2}{d_+^2} - \frac{\pi^6}{d_+^6 L^2} b_{\omega_0}^2 a^6 + o(a^6), & d_+ > d_-, \\ \frac{\pi^2}{a^2} - \frac{4\pi^6}{d_+^6 L^2} b_{\omega_0}^2 a^6 + o(a^6), & d_+ = d_- = d. \end{cases}$$

Here, b_{ω_0} is the average virtual mass of the window. In the case of small round windows ω_i with a dimensionless radius R, the values of b_{ω_0} are known [11] and we obtain

$$\lambda_{\min,a} = \begin{cases} \frac{\pi^2}{d_+^2} - \frac{16\pi^4}{81 d_+^6 L^2} R^6 a^6 + o(a^6), & d_+ > d_-, \\ \frac{\pi^2}{d^2} - \frac{64\pi^4}{81 d_+^6 L^2} R^6 a^6 + o(a^6), & d_+ = d_- = d. \end{cases}$$

Now consider a periodic lattice of the coupling windows with the corresponding Bravais lattice Λ_2:

$$\Lambda_2 = \{n_1 a_1 + n_2 a_2 \in \mathbf{R}^2 | (n_1, n_2)| \in \mathbf{Z}^2\},$$

where a_1 and a_2 are linearly independent vectors in $\mathbf{R}^2$. Let the reciprocal lattice Γ_2, the Wigner–Seitz cell $\hat{\Gamma}_2$, and the Brillouin zone $\hat{\Lambda}_2$ be such that

$$\Gamma_2 = \{n_1 b_1 + n_2 b_2 \in \mathbf{R}^6 | (n_1, n_2) \in \mathbf{Z}^2\},$$
$$a_j b_{j'} = 2\pi\delta_{jj'}, \quad j, j' = 1, 2.$$

$$\hat{\Gamma}_2 = \{s_1 a_1 + s_2 a_2 \in \mathbf{R}^2 | s_j \in [-1/2, 1/2), \quad j = 1, 2\},$$

$$\hat{\Lambda}_2 = \{s_1 b_1 + s_2 b_2 \in \mathbf{R}^2 | s_j \in [-1/2, 1/2), \quad j = 1, 2\}.$$

Here, the asymptotics is constructed using the same scheme as that for the chain, but the function $f_{\Lambda_1}(k_{a,\theta})$ with the asymptotics (2) is replaced by $f_{\Lambda_2}(k_{a,\theta})$ such that

$$f_{\Lambda_2}(k_{a,\theta}) = |\hat{\Lambda}_2|^{-1} 4\pi^2 (|\gamma_\theta + \theta|^2 + \pi^2 d_+^{-2} - k_{a,\theta}^2),$$
$$|\gamma_\theta + \theta|^2 = \min_{\gamma \in \Gamma_2} |\gamma + \theta|^2,$$

$$f_{\Lambda_2}(k_{a,\theta}) = k_{3,\theta}^{\Lambda_2} a^3 + o(a^3).$$

In this case, the solution for sufficiently small windows also does not exhibit a gap and the lower-boundary asymptotics of continuous spectrum is as follows:

$$\lambda_{\min,a} = \begin{cases} \frac{\pi^2}{d_+^2} - |\hat{\Lambda}_2| \frac{\pi}{2 d_+^3} b_{\omega_0} a^3 + o(a^3), & d_+ > d_-, \\ \frac{\pi^2}{d^2} - |\hat{\Lambda}_2| \frac{\pi}{d_+^3} b_{\omega_0} a^3 + o(a^3), & d_+ = d_- = d. \end{cases}$$

For small round windows, this yields

$$\lambda_{\min,a} = \begin{cases} \frac{\pi^2}{d_+^2} - |\hat{\Lambda}_2| \frac{\pi}{9 d_+^3} R^3 a^3 + o(a^3), & d_+ > d_-, \\ \frac{\pi^2}{d^2} - |\hat{\Lambda}_2| \frac{4}{9 d_+^3} R^3 a^3 + o(a^3), & d_+ = d_- = d. \end{cases}$$

Acknowledgments. This study was supported by the Russian Foundation for Basic Research (project no. 01-01-00253) and by grants from the Ministry of Education of the Russian Federation and from ISF.

REFERENCES

1. C. W. J. Beenakker and H. van Houten, in *Solid State Physics: Advances in Research and Applications*, Ed. by H. Ehrenreich and D. Turnbull (Academic, New York, 1991), Vol. 44, pp. 1–228.
2. P. Duclos and P. Exner, Rev. Math. Phys. **7**, 73 (1995).
3. P. Exner and S. Vugalter, J. Phys. A **30**, 7863 (1997).
4. A. M. Il'in, *Matching of Asymptotic Expansions of Boundary Problem Solutions* (Nauka, Moscow, 1989).
5. R. R. Gadyl'shin, Algebra Analiz **4** (2), 88 (1992).
6. I. Yu. Popov, Pis'ma Zh. Tekh. Fiz. **25** (3), 57 (1999) [Tech. Phys. Lett. **25**, 106 (1999)].
7. I. Yu. Popov, Rep. Math. Phys. **43** (3), 427 (1999).
8. I. Yu. Popov, Phys. Lett. A **264** (2-3), 148 (2000).
9. S. V. Frolov and I. Yu. Popov, J. Math. Phys. **41** (7), 4391 (2000).
10. I. Yu. Popov, Appl. Math. Lett. **14**, 109 (2001).
11. M. Schiffer and G. Szego, Trans. Am. Math. Soc. **67** (1), 130 (1949).

Translated by P. Pozdeev

Technical Physics Letters, Vol. 27, No. 10, 2001, pp. 857–859. Translated from Pis'ma v Zhurnal Tekhnicheskoĭ Fiziki, Vol. 27, No. 20, 2001, pp. 29–34.

Investigation of the Process of Voltage Distribution over Elements of a High-Power Semiconductor Current Interrupter

A. V. Ponomarev, S. N. Rukin*, and S. N. Tsyranov

Institute of Electrophysics, Ural Division, Russian Academy of Sciences, Yekaterinburg, Russia

** e-mail: rukin@iep.uran.ru*

Received May 31, 2001

Abstract—The process of voltage distribution over serially connected elements of a high-power semiconductor current interrupter in the stage of current breakage is studied within the framework of a previously developed physicomathematical model. It is established that a mechanism is operative that provides for the voltage drop leveling between unit structures of the p^+–p–n–n^+ type with various depths X_p of the p–n junctions. The mechanism is related to the fact that the formation of a strong field region on the stage of current breakage in the unit structures with larger X_p begins later, but the expansion of this region proceeds faster than the same processes in the units with smaller X_p. *© 2001 MAIK "Nauka/Interperiodica".*

Introduction. The SOS-diode-based semiconductor current interrupters are employed in the generators of high-power nanosecond pulses in the schemes with inductive energy storage [1]. An SOS diode is a system comprising a large number of serially connected unit structures of the p^+–p–n–n^+ type. In practice, an important problem related to the proper functioning of such a serial system of semiconductor devices is to provide a uniform voltage distribution over elements of the SOS diode structure, which is necessary to ensure reliable failure-proof operation of the pulse-switching device. This task is solved either by using resistive voltage dividers (compensating the technological scatter in characteristics of the individual elements arising in the fabrication stage) or by selecting component structures, prior to assembling an SOS diode, with respect to the capacitance–voltage and current–voltage characteristics [2].

The experience of using SOS diodes showed that these devices can reliably operate on a megavolt signal even without taking the above measures, provided that the number of serially connected structural elements in the current interrupter exceeds 10^3. Based on this fact, we may suggest that an internal mechanism is inherent in the SOS diodes which is capable of providing for a uniform voltage distribution over a large number of serially connected elements. A special feature of the dopant distribution profile in SOS diodes is a large depth X_p of the p–n junction (reaching up to 200 μm [3, 4]). The X_p value is the main characteristic determining the process of a strong field region (SFR) formation in an SOS diode structure in the stage of current breakage. The SFR width and the SFR formation rate are factors determining the maximum possible voltage applicable to a given structure.

The purpose of this study was to describe the process of voltage distribution over serially connected structural elements of an SOS diode in the stage of current breakage.

Description of model. The calculations were conducted using a physicomathematical model developed previously [5]. The SOS diode structure and the pumping scheme were analogous to those described in [3]. The SOS diode studied contained 10 serially connected unit elements. For modeling the technological scatter of parameters, the X_p values of individual elements were varied in a range from 170 to 188 μm at a 2 μm step. All elements had an area of 0.24 cm^2.

After switching on the direct pump capacitor, a dc current with a density of up to 1.75 kA/cm^2 was passing through the SOS diode elements over a time period of 420 ns. During the subsequent switching on the reverse pump capacitor, the system conducted a reverse current over a time period of 70 ns, with a density reaching 4.6 kA/cm^2 by the instant of current breakage.

The notation is illustrated in Fig. 1. In the stage of current breakage, a characteristic strong field region of width W with clear boundaries is formed in the p layer of each element. This region expands at a velocity of $V = V_1 - V_2$, where V_1 and V_2 are the velocities of the left- and right-hand boundaries, respectively. The right-hand SFR boundary coincides with the position of the excess plasma front, while the left-hand boundary corresponds to the point where the current saturation condition is obeyed. The breakdown field strength in the SFR amounts to 200 kV/cm and varies rather weakly in the current breakage stage. The voltage drop across the SOS diode element is determined mostly by the SFR

1063-7850/01/2710-0857$21.00

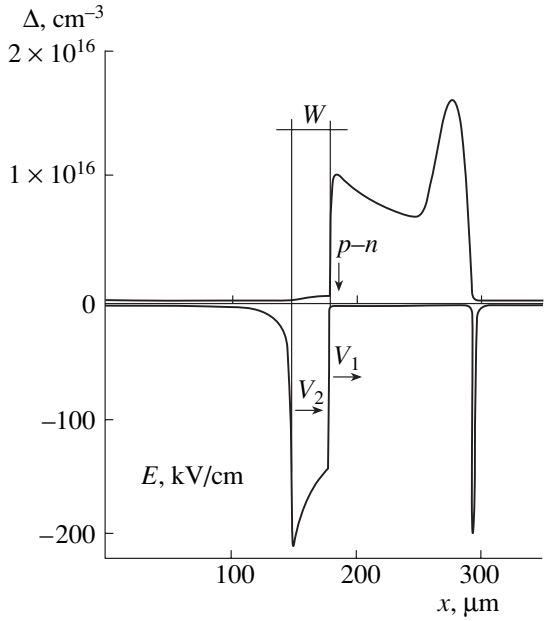

Fig. 1. A schematic diagram showing the excess plasma density distribution and the electric field profile in a SOS diode element with X_p = 180 μm in the stage of current breakage (current density, 4.6 kA/cm^2). Arrows indicate the position of the *p–n* junction and the SFR boundary velocities.

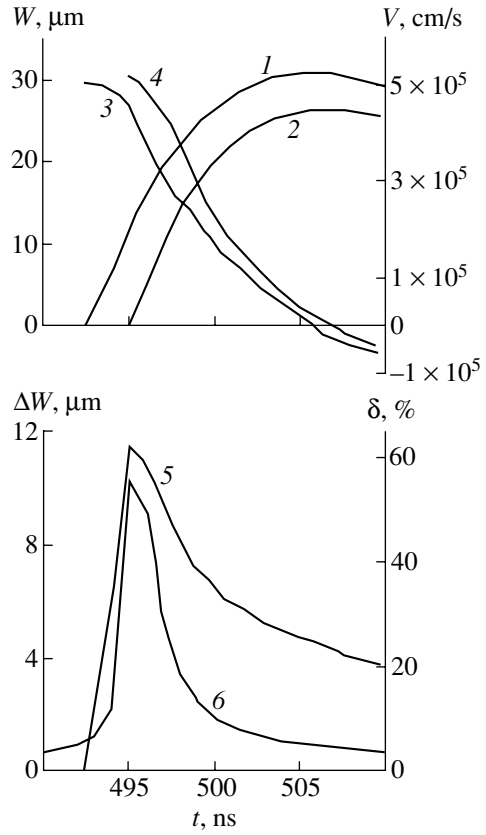

Fig. 2. The time variation of (*1*, *2*) SFR width *W*, (*3*, *4*) SFR expansion velocity *V*, (*5*) Δ*W*, and (*6*) δ in the stage of current breakage for the SOS diode elements with X_p = 170 (*1*, *3*) and 188 μm (*2*, *4*).

width *W*. In the beginning of the current breakage process, the V_1 value is greater than V_2, the SFR expands, and the voltage difference across the element increases. Then the velocities of both SFR boundaries decrease so that V_2 becomes greater than V_1. As a result, the SFR width decreases and the voltage difference across the element falls [3].

It should be noted that a characteristic strong field region in the current breakage stage also exists in the right-hand part of the element, near the n–n^+ junction (Fig. 1). However, this SFR is only a few microns wide and virtually does not influence the process of current breakage and the voltage drop across the element.

Results and discussion. It was found that the SFR formation in the SOS diode elements with smaller X_p values begins earlier than the process in elements with greater depths of the junction. The maximum difference in the onset time of the SFR formation, observed for the elements with most strongly differing X_p values (170 vs. 188 μm), is 2.5 ns (Fig. 2). The same elements exhibit a maximum difference in *W* and, hence, in the voltage drop. The mechanism responsible for the earlier operation of structures with smaller X_p is as follows. In the stage of direct pumping, when the charge is accumulated in the *p* layer of each element, the excess plasma density is higher in the elements with smaller X_p, where the same accumulated charge is distributed over the *p* layer of a smaller thickness. Accordingly, the elements with smaller X_p are characterized by a higher intensity of the recombination processes and by a lower amount of the accumulated charge that can be subsequently carried by the reverse current. In the stage or reverse pumping, for the same law of the current density variation in time (determined by the serial connection of elements), a lower amount of the charge accumulated in the elements with smaller X_p results in that the carrier velocity saturation in the *p* layer and the SFR formation in these elements begin earlier than in the elements with large X_p.

By the onset time of the SFR formation in the element with X_p = 188 μm (see Fig. 2, curve *2*), the SFR width in the element with X_p = 170 μm (see Fig. 2, curve *1*) already reaches 11.5 μm. At this instant, an inhomogeneity of the voltage distribution over elements is most pronounced. A maximum deviation δ = 56% of the voltage drop across a given element from the average value is observed for the element with X_p = 170 μm. This deviation is determined by the formula $\delta = |U_i - U_{av}| \times 100\%/U_{av} \times 100\%$, where U_{av} is the arithmetic mean for an element in the SOS diode structure (Fig. 2, curve *6*).

Darznek *et al.* [3] showed that the elements with larger X_p values are characterized by higher SFR expansion velocities owing to a lower excess plasma density in the *p* layer. As can be seen from Fig. 2 (cf. curves *3* and *4*), the velocity *V* of the SFR expansion in the element with X_p = 188 μm always exceeds that in the ele-

ment with X_p = 170 μm. This circumstance results in that both the SFR width difference ΔW and the voltage drop deviation δ decrease in the course of the current breakage. By the moment of attaining the maximum voltage drop (maximum *W*), a difference in the SFR width does not exceed 5 μm (Fig. 2, curve *5*) and the δ value drops down to 4% (Fig. 2, curve *6*).

Conclusion. The model calculations showed that a SOS diode composed of serially connected elements features a mechanism providing for the voltage drop leveling between the elements with different depths of the *p*–*n* junction. The mechanism is related to the fact that the formation of a strong field region on the stage of current breakage in the unit structures with larger X_p begins later, but the expansion of this region proceeds faster than the same processes in the units with smaller X_p.

REFERENCES

1. S. N. Rukin, Prib. Tekh. Éksp., No. 4, 5 (1999).
2. V. M. Tuchkevich and I. V. Grekhov, *Novel Principles of High-Power Switching by Semiconductor Devices* (Nauka, Leningrad, 1988).
3. S. A. Darznek, S. N. Rukin, and S. N. Tsiranov, Zh. Tekh. Fiz. **70** (4), 56 (2000) [Tech. Phys. **45**, 436 (2000)].
4. S. A. Darznek *et al.*, Élektrotekhnika, No. 4, 20 (1999).
5. S. A. Darznek *et al.*, Zh. Tekh. Fiz. **67** (10), 64 (1997) [Tech. Phys. **42**, 1170 (1997)].

Translated by P. Pozdeev

Technical Physics Letters, Vol. 27, No. 10, 2001, pp. 860–861. Translated from Pis'ma v Zhurnal Tekhnicheskoĭ Fiziki, Vol. 27, No. 20, 2001, pp. 35–38.

The Effect of Electric Field on Nonpolar Liquids Not Contacting with Potential Electrodes

N. N. Krasikov and O. V. Shuvaeva

Kovrov State Technological Academy, Kovrov, Russia

Received May 10, 2001

Abstract—It is experimentally established that a contactless exposure of liquids representing the homologous series of alkanes to a high-strength electric field leads to the appearance of an optical anisotropy. The effect, related to a field-induced partial ordering (orientation) of extended molecules, is more clearly manifested in the liquids possessing higher molecular masses (longer molecules). *© 2001 MAIK "Nauka/Interperiodica".*

When a dielectric liquid exposed to an electric field is not in contact with the potential electrodes, we may neglect the electric current irrespective of the electric conductivity of the liquid [1]. We have studied the behavior of nonpolar liquids in an electric field generated by a source of dc voltage U = 5–15 kV. The liquid was separated from the upper electrode by an air–vapor gap and from the lower electrode, by the insulating (organic glass) cell bottom, so that the measuring system represented a three-layer capacitor.

The experiments were performed with compounds representing the homologous series of alkanes, including *n*-nonane (C_9H_{20}), *n*-decane ($C_{10}H_{22}$), *n*-undecane ($C_{11}H_{24}$), and *n*-dodecane ($C_{12}H_{26}$), occurring under normal conditions in the form of liquids. Compounds in the series studied possess identical molecular structures, differing from each other by one added CH_2 group. The permittivity slightly increases (from 1.598 to 2.006) on the passage from light to heavier substances [2]. The optical transmission of a polarized light was measured and characterized as percentage relative to the value observed in the absence of the electric field. The optical cell with a liquid was placed between electrodes at a voltage of 10 kV. The air gap width was 17 mm, the liquid layer thickness was 25 mm, and the insulating bottom thickness was 3 mm. The method of measurements was described previously [1].

The experimental data are presented in Fig. 1. All four liquids studied show a decrease in the relative optical transmission after switching the field on, followed by attaining a certain individual saturation level. Upon switching the field off, the transmission gradually restores on the initial level observed before the voltage application. As the molecular mass (chain length) increases, the relative transmission also varies: the η value for *n*-dodecane is almost two times that for *n*-nonane. The same refers to the relaxation time, as is clearly observed after the field switch-off.

The experimentally observed variation in the optical transmission under the action of the applied electric field can be related to the orientational ordering of hydrocarbon molecules, whereby structures intermediate between those typical of liquid and solid crystalline states are formed in the paraffins. Following [3], the main role in this process may belong to the methylene (CH_2) groups, the number of which increases by unity on the passage to each next member of the series studied.

The molecules of *n*-paraffins in the liquid state are involved in the dispersive and sterical interactions, tending to arrange "apex-to-apex" with respect to one another. The molecules most probably rotate about longitudinal axes terminated by symmetric CH_3 groups [4]. For the electric field action to take place, it is necessary

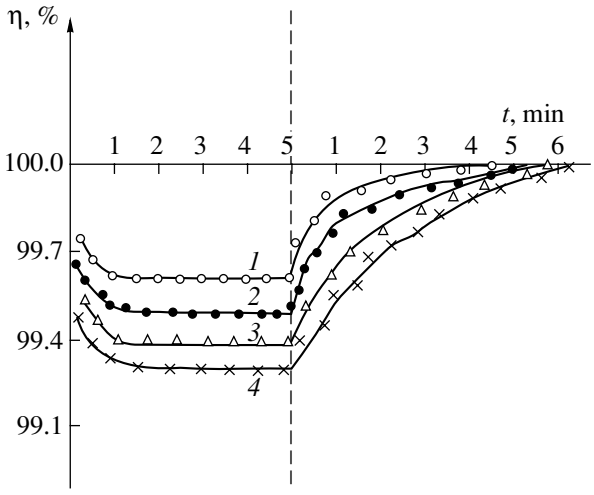

Fig. 1. Time variation of the transmission of a polarized light η in the liquids studied (percentage of that for the control sample) exposed to the electric field (switched on at t = 0 and off at t = 5 min): (*1*) *n*-nonane (C_9H_{20}); (*2*) *n*-decane ($C_{10}H_{22}$); (*3*) *n*-undecane ($C_{11}H_{24}$); (*4*) *n*-dodecane ($C_{12}H_{26}$).

1063-7850/01/2710-0860$21.00 © 2001 MAIK "Nauka/Interperiodica"

that the integrally nonpolar molecules would contain electrically active elements. Although the hydrocarbon molecules possess (on the whole) no dipole moment, there are nonzero dipole moments of the individual CH_2 groups amounting to $0.4D$ ($D = 3.33 \times 10^{-30}$ C m) [5].

Let us consider a saw-tooth-shaped *n*-paraffin molecule as a system of dipoles arranged at the apices facing opposite directions (Fig. 2). We may suggest that each dipole **p** is subject to a rotating moment $\mathbf{M} = [\mathbf{p} \times \mathbf{E}]$. Acting upon such dipole systems, the rotating moments tend to order the molecules so as to reverse one (upper) group and rotate another (lower) group in the field **E**. The energy of interaction between the field and the dipoles is determined by the scalar product $W = -\mathbf{pE}$. In the limit, the limiting *W* values can be obtained for the dipoles of both groups. The upper group is characterized by a maximum (unstable equilibrium), while the lower group possesses a minimum reflecting a stable equilibrium for the molecule exposed to the field **E**. Thus, the existence of individual dipole moments due to the CH_2 groups implies manifestations of a partial ordering of the hydrocarbon molecules, with their longitudinal axes arranged perpendicularly to the applied field **E**. The process of ordering proceeds by a mechanism of the anomalous relaxation type [6].

The proposed model corresponds to a possible physical approach, not stating that it is the only possible variant. It should be pointed out that notions of the volume–charge polarization [1] characteristic of the dipole liquids (water and alcohols) either possess restricted validity or are not at all applicable to the system under consideration.

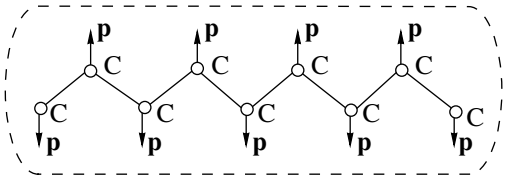

Fig. 2. Schematic diagram of a linear *n*-paraffin molecule (dashed contour indicates the external boundary of CH_2 and CH_3 groups.

REFERENCES

1. N. N. Krasikov and O. V. Shuvaeva, Pis'ma Zh. Tekh. Fiz. **26** (11), 75 (2000) [Tech. Phys. Lett. **26**, 485 (2000)].
2. M. F. Vuks, *Electrical and Optical Properties of Molecules in Condensed Matter* (Leningr. Gos. Univ., Leningrad, 1984).
3. V. M. Tatevskiĭ, *Molecular Structure* (Khimiya, Moscow, 1977).
4. A. S. Akhmatov, *Molecular Physics of Boundary Friction* (Fizmatgiz, Moscow, 1963).
5. V. I. Minkin, O. A. Osipov, and Yu. A. Zhdanov, *Dipole Moments* (Khimiya, Leningrad, 1968).
6. G. E. Skvortsov, Pis'ma Zh. Tekh. Fiz. **25** (7), 57 (1999) [Tech. Phys. Lett. **25**, 274 (1999)].

Translated by P. Pozdeev

Technical Physics Letters, Vol. 27, No. 10, 2001, pp. 862–864. Translated from Pis'ma v Zhurnal Tekhnicheskoĭ Fiziki, Vol. 27, No. 20, 2001, pp. 39–45.

The Effect of the Irradiated Glass Target Temperature on the Implanted Silver Distribution Profile

A. L. Stepanov

Institute of Physics 1, Aachen Technical University, 52056 Aachen, Germany;
Kazan Physicotechnical Institute, Russian Academy of Sciences, Kazan, Tatarstan, 420029 Russia
e-mail: anstep@dionis.kfti.knc.ru

Received May 10, 2001

Abstract—Features of the profiles of silver ions implanted into a soda–lime silicate glass were studied depending on the substrate temperature varied in a narrow range from 20 to 100°C. The implant depth–concentration profiles were modeled with an allowance for a thermostimulated increase in the diffusion mobility of the implanted impurity in the sample volume. It is shown that an increase in the substrate temperature by several tens of degrees leads to a diffusion smearing of the implanted impurity profile and, hence, to a decrease in the local implant concentration hindering the metal silver nucleation. An analysis of the results of modeling points to the need in thoroughly controlling the substrate temperature in order to provide for the required conditions of the metal nanoparticle synthesis and to obtain the metal–glass composites with reproducible characteristics.

The task of obtaining thin composite layers based on inorganic glasses containing synthesized metal nanoparticles is currently important for various practical applications. One of the actively developed methods for the preparation of such layers is ion implantation, which allows reaching high values of the filling factor for a metal implanted into dielectric substrates [1, 2]. By varying on the ion implantation parameters, including the ion energy and dose, ion beam current, and the target temperature, it is possible to modify the conditions of synthesis of the implanted metal nanoparticles.

The latter implantation process parameter—the target temperature—was recently demonstrated (see, e.g., [3–5]) to significantly affect the distribution of implanted metal ions in glass substrates and, hence, the final properties of metal–glass composites. Despite a broad (but not systematic) set of substrate temperatures used in the cited papers (from 77 to 300 K), it was suggested that one of the pathways for the temperature influence is a thermoinduced increase in the diffusion mobility of implanted impurity in the substrate material. On the whole, this problem is still insufficiently studied and the available data are very restricted. Recent experimental investigations of the metal ion implantation showed that the optical properties of composites may significantly differ even when the temperature of a soda–lime glass substrate varies in a narrow interval from 20 to 50°C [5, 6].

The purpose of this study was to model the effect of the temperature of a soda–lime silicate glass, varied in a narrow range from 20 to 100°C, on the depth profile of implanted Ag^+ ions with an allowance for the thermostimulated impurity diffusion process.

The modeling was performed for the ion energies (30–150 keV) and doses (2×10^{16} ion/cm^2) typically employed in the ion- implantation synthesis of metal nanoparticles [1]. Since the problem refers to the stage of Ag^+ ion implantation preceding the metal nanoparticle formation, the calculations are restricted to the dose indicated above. Once this level is exceeded, the accumulated concentration of Ag^0 impurity atoms in the near-surface region increases above the solubility limit of silver in the glass substrate and the silver nanoparticles form to become effective sinks for the delivered Ag^+ ions, which hinders further spreading of the implant deeper into the substrate [1, 5]. Moreover, the phase composition of the implanted layer containing metal nanoparticles becomes significantly different from that of the initial soda–lime silicate glass.

On the whole, the ion implantation process can be subdivided with respect to time into several stages, including the incorporation of accelerated ions, the diffusion of implant, and the nanoparticle nucleation and growth. In the initial implantation stage, the implant concentration profile can be described (ignoring the surface sputtering effects) by a statistical Gauss distribution function. This distribution can be calculated by the Monte Carlo method, for example, using the TRIM (Transport of Ions in Matter) or SRIM (Stopping and Range of Ions in Solids) computer program packages [7]. However, these models do not take into account the effect of the ion dose on the implant distribution profile in depth of the target [8]. In this study, the contribution of the temperature-dependent diffusion mobility of implanted metal ions on their concentration redistribution in various implantation stages (i.e., on the

1063-7850/01/2710-0862$21.00 © 2001 MAIK "Nauka/Interperiodica"

irradiation time and/or dose) is taken into account by using the diffusion equation with a continuous source [1]:

$$\frac{\partial N(x,t)}{\partial t} = D\frac{\partial^2 N(x,t)}{\partial x^2} + n(x,t). \quad (1)$$

Here, $N(x, t)$ is the implanted ion concentration, D is the impurity diffusion coefficient, $n(x, t)$ is the amount of impurity introduced by ion implantation, x is the distance (depth) measured from the surface, and t is the implantation duration (time). To simplify the problem, the D value in Eq. (1) is assumed to be independent of x and the temperature of the soda–lime silicate glass substrate is assumed to be fixed (constant in time). We will also assume that $n(x, t)$ at the initial time instant is descried by a Gaussian distribution function [7]

$$n(x,t) = \frac{\Phi}{\Delta R_p (2\pi)^{1/2}} \exp\left[-\frac{1}{2}\left(\frac{x-R_p}{\Delta R_p}\right)^2\right], \quad (2)$$

where Φ is the ion flux (ion current) per unit area, R_p is the average projected range of implanted ions in the sample, and ΔR_p is the corresponding standard deviation from R_p. The R_p and ΔR_p values corresponding to the irradiation of soda–lime silicate glass substrates by Ag^+ ions with the energies 30, 60, 100, and 150 keV were calculated within the framework of the standard TRIM procedure using an SRIM-2000 program [7]. The solution of Eq. (1) under the conditions of step-by-step ion dose increase in the substrate, with an allowance for the dynamic implant profile variation in time the as a result of diffusion, leads to determination of the resulting implant distribution in depth of the substrate. For modeling the Ag^+ ion distribution in the soda–lime silicate glass substrate, we will use an analytical solution of Eq. (1) obtained previously for the implantation of semiconductors [9]:

$$N(x,t) = \Phi\sqrt{\frac{2Dt+\Delta R_p^2}{2\pi D^2}}\exp\left(-\frac{\alpha^2}{4Dt+2\Delta R_p^2}\right) - \Phi\sqrt{\frac{\Delta R_p^2}{2\pi D^2}}\exp\left(-\frac{\alpha^2}{2\Delta R_p^2}\right) + \frac{\alpha\Phi}{2D}\left(\operatorname{erfc}\frac{\alpha}{\sqrt{4Dt+2\Delta R_p^2}} - \operatorname{erfc}\frac{\alpha}{\Delta R_p\sqrt{2}}\right), \quad (3)$$

where $\alpha = x - R_p$. As follows from this expression, the temperature-dependent diffusion coefficient $D(t)$ determines the shape of the resulting impurity profile deviating from the initial Gaussian distribution. To estimate the diffusion coefficients of Ag^+ ions (D_{Ag}) in the soda–lime silicate glass substrate, we will use the Arrhenius equation with the diffusion activation energy E_a = 0.69 eV and the preexponential term $D_0 = 5.6 \times 10^{-5}$ cm^2/s determined in [10]. The obtained D_{Ag} values

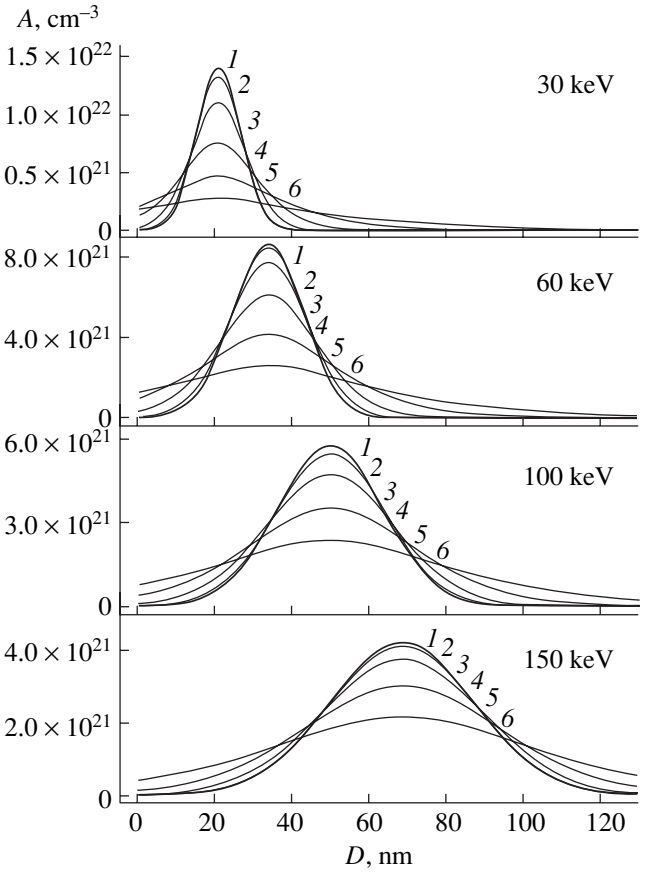

The profiles of atomic concentration A versus depth D of Ag^+ ions implanted at various ion beam energies into soda–lime silicate glass substrates heated to various temperatures. The model calculations were performed using a SRIM-2000 program (*1*) without an allowance for the implant diffusion and (*2*–*6*) taking into account the thermostimulated diffusion of silver at a substrate temperature of (*2*) 20, (*3*) 40, (*4*) 60, (*5*) 80, and (*6*) 100°C.

are assumed to be independent of the ion implantation duration at a fixed temperature of the glass substrate.

The model profiles of the Ag^+ ion distribution in depth of the soda–lime silicate glass substrates implanted at various ion energies are presented in the figure. The samples were implanted over 360 s using an ion beam with a current density of 5.58×10^{13} ion/(cm^2 s), which corresponds to a total dose of 2×10^{16} ion/cm^2. As can be seen from the figure, an increase in the substrate temperature from 20 to 100°C (and the corresponding growth in the diffusion coefficient D_{Ag} from 2.88×10^{-17} to 2.66×10^{-14} cm^2/s) leads to a significant broadening of the initial Gaussian profile of the impurity distribution and to a decrease in the implant concentration in the distribution peak even without an allowance for the radiation-stimulated diffusion. The redistribution of silver (diffusion-induced ion loss) from the implanted layer is related to a concentration gradient and an increase in the diffusion coefficient with growing tem-

perature, which is especially important for the implantation at lower energies.

Thus, the distribution of implanted Ag^+ ions in a sample may significantly vary even upon a small change in the temperature of the soda–lime silicate glass substrate. Therefore, the substrate temperature is one of the critical factors determining the process of silver accumulation in local regions of the implanted layers. As the temperature increases, other conditions being equal, a higher total irradiation dose would be required in order to reach the critical impurity concentration necessary for the nucleation of nanoparticles.

It must be emphasized that the temperature interval leading to such a significant change in the implant distribution profile only rather insignificantly exceeds room temperature, which is indicative of a high temperature sensitivity of the process of silver ion implantation into silicate glasses. Apparently, the high diffusion mobility of Ag atoms and the resulting loss from the implanted layer at a sufficiently high temperature may hinder the synthesis of metal nanoparticles in the bulk of a glass substrate within a reasonable implantation time. This was in fact observed previously for a soda–lime silicate glass substrate implanted with 60-keV Ag^+ ions at a temperature of 180°C [4, 5]. It should also be recalled that the results of modeling presented above were obtained assuming that the glass substrate temperature and the local temperature in the implanted region are equal. In practice, however, the implanted glass surface possesses a higher temperature due to the radiation-induced heating that was ignored in our model calculations.

Conclusion. Thus, we have modeled the process of Ag^+ ion implantation into a soda–lime silicate glass substrate and studied the profiles of implanted impurity distribution in depth with an allowance for the substrate temperature, that is, for the thermostimulated diffusion process. It was shown that even a small (within several tens of degrees) heating of the glass substrate above room temperature leads to "smearing" of the impurity distribution profile as a result of the outward (to the surface) and inward (to the sample bulk) diffusion of implanted silver atoms. As a result, the implantation of metal ions into a glass substrate occurring at an elevated temperature must be performed to a higher total dose in order to reach the critical implant concentration in the implanted layer necessary for the nucleation of metal nanoparticles.

An analysis of the obtained results points to the necessity of thoroughly monitoring and controlling the substrate temperature during the implantation. This is especially important for the dielectric substrates possessing low thermal conductivities which, heated by the ion beam current, cannot be effectively cooled by standard technical means. The overheating would unavoidably affect the conditions of nanoparticle synthesis and the reproducibility of characteristics of the metal–glass composites.

Acknowledgments. The author is grateful to Prof. P. Townsend (University of Sussex, England) for his useful advice and fruitful discussions of results. The author is grateful to the Alexander Humboldt Foundation (Germany) for the financial support of his work in Germany. The work was supported by the Russian Foundation for Basic Research, project nos. 99-02-17767 and 00-15-96615.

REFERENCES

1. P. D. Townsend, P. J. Chandler, and L. Zhang, *Optical Effects of Ion Implantation* (Cambridge Univ. Press, Cambridge, 1994).
2. A. L. Stepanov, I. B. Khaĭbullin, P. D. Townsend, D. Hole, and A. A. Bukharaev, RF Patent No. 2156490 (2000).
3. G. W. Arnold and J. A. Borders, J. Appl. Phys. **48**, 1488 (1977).
4. N. D. Skelland and P. D. Townsend, J. Non-Cryst. Solids **188**, 243 (1995).
5. D. E. Hole, A. L. Stepanov, and P. D. Townsend, Nucl. Instrum. Methods Phys. Res. B **166**, 26 (2000).
6. A. L. Stepanov, D. Hole, and V. N. Popok, Pis'ma Zh. Tekh. Fiz. **27** (13), 57 (2001) [Tech. Phys. Lett. **27**, 554 (2001)].
7. J. F. Ziegler, J. P. Biersak, and U. Littmark, *The Stopping and Range of Ions in Solids* (Pergamon, New York, 1996).
8. A. L. Stepanov, V. A. Zhikharev, and I. B. Khaĭbullin, Fiz. Tverd. Tela (St. Petersburg) **43** (4), 733 (2001) [Phys. Solid State **43**, 766 (2001)].
9. S. Namba, K. Masuda, K. Gamo, *et al.*, in *Proceedings of the Conference on Ion Implantation in Semiconductors, London, 1971*, pp. 231–236.
10. A. Berger, J. Non-Cryst. Solids **151**, 88 (1992).

Translated by P. Pozdeev

Technical Physics Letters, Vol. 27, No. 10, 2001, pp. 865–867. Translated from Pis'ma v Zhurnal Tekhnicheskoĭ Fiziki, Vol. 27, No. 20, 2001, pp. 46–50.

An Electron Microscopy Study of a Copper Surface During the Sliding Boundary Friction in the Presence of Fullerene C_{60}

O. F. Kireenko, A. A. Sitnikova, and B. M. Ginzburg

Institute of Machine Science, Russian Academy of Sciences, St. Petersburg, Russia;
Ioffe Physicotechnical Institute, Russian Academy of Sciences, St. Petersburg, 194021 Russia

Received May 4, 2001

Abstract—The structure of a protective film formed on the copper counterbody surface during the sliding boundary friction in the presence of fullerene C_{60} additives in a lubricant oil was studied by transmission electron microscopy and electron diffraction. © *2001 MAIK "Nauka/Interperiodica".*

Previously [1–3], we reported that a fullerene-containing soot and the pure powder of fullerene C_{60} added to a commercial lubricant oil provide for a significant increase in the antifriction and antiwear properties of copper–steel couples in the sliding boundary friction regime. The structure and the mechanical properties of the surface of a copper counterbody were studied by a combination of physical techniques [2, 3]. The wide-angle X-ray diffraction data showed that the structure of the friction surface of the copper counterbody remains almost unchanged when C_{60} is present in the lubricant oil, whereas significant structural changes take place for the same base oil without fullerene additives.

The fact that the counterbody surface structure remained intact was explained by a thin protective film (with a thickness not exceeding 1000 Å) formed on the copper surface in the course of friction, which was confirmed by scanning electron microscopy. Possessing a very small thickness, the film did not contribute to the X-ray diffraction pattern; nor did we manage to separate the film from the copper foil and study the film structure immediately without substrate. In this study, we employed a different experimental approach, whereby a copper foil with the film formed during friction was sputtered by an ion beam from the rear side (opposite to the friction contact surface) unless a crater with a through hole was etched. A thin edge of this hole was studied by transmission electron microscopy (TEM) in both light and dark field, as well as by the electron diffraction technique.

For comparison, we have studied 200-μm-thick copper foil counterbody samples of the two types, obtained upon the friction test with steel lubricated with a base (fullerene-free) lubricant oil and with the same oil containing a 5 wt % C_{60} additive. The TEM measurements were performed on a Philips EM-420 electron microscope operated at an accelerating voltage of up to 100 kV.

Figure 1a shows a TEM image of the hole edge region in the foil tested with the fullerene-free lubricant oil in the so-called "wearless" friction mode [4]. As can be seen, the hole edge (i.e., the friction surface) bears a film that apparently accounts for a low value of the friction coefficient and prevents from the mutual mass transfer between dissimilar metal counterbodies and their intermixing on a microscopic level [5]. The film, with a thickness estimated at ~100 Å, shows a good stability with respect to the electron beam action and exhibits an amorphous structure (producing no reflections in the corresponding electron diffraction patterns). The film is likely to represent a strongly crosslinked tribopolymer network composed of low-molecular-weight hydrocarbon chains (present in the oil) [6]. Under this film, the friction surface displays a finely dispersed structure with a grain size on the order of 0.1 μm. This observation is consistent with the results of our previous investigation using the scanning electron microscopy technique [4]. A self-organized structure of this type probably ensures dissipation of the friction energy by means of the grain displacement and rotation in the near-surface layer. The electron diffraction patterns (Fig. 1b) confirm that the near-surface layer is composed of the crystalline copper grains with an admixture of Cu_2O particles. No traces of the transfer of steel particles to the friction surface of the copper counterbody was observed in this system.

In the presence of C_{60}, no fragmentation of the near-surface copper layer was observed either (Fig. 2a). In this case, an amorphous surface film is also formed on copper in the course of friction. However, the film thickness is about ten times that (below 1000 Å) observed in the absence of fullerene and is readily damaged by the electron beam. The latter circumstance can be explained by a lower energy of the β bonds in the hydrocarbon chains covalently bound to C_{60} [3, 7] and

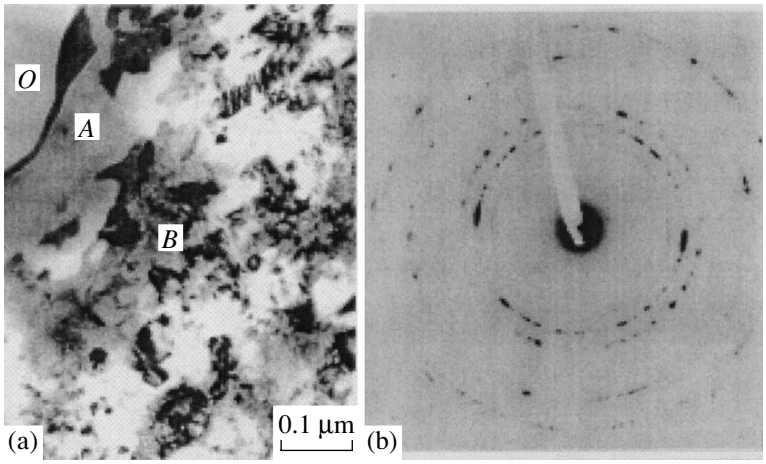

Fig. 1. (a) A light-field TEM micrograph of the ion-etched hole edge (*O*) and the surrounding craterlike "section" in a foil copper upon friction with a base lubricant oil (×150000) showing a ~100-Å-thick surface film (region *A*) and a block structure of ~0.1-μm-sized (1000 Å) grains in a near-surface metal layer (region *B*). (b) Electron diffraction pattern from the block structure, representing a superposition of diffractograms typical of the Cu and Cu_2O lattices (diffraction brightness index, 140).

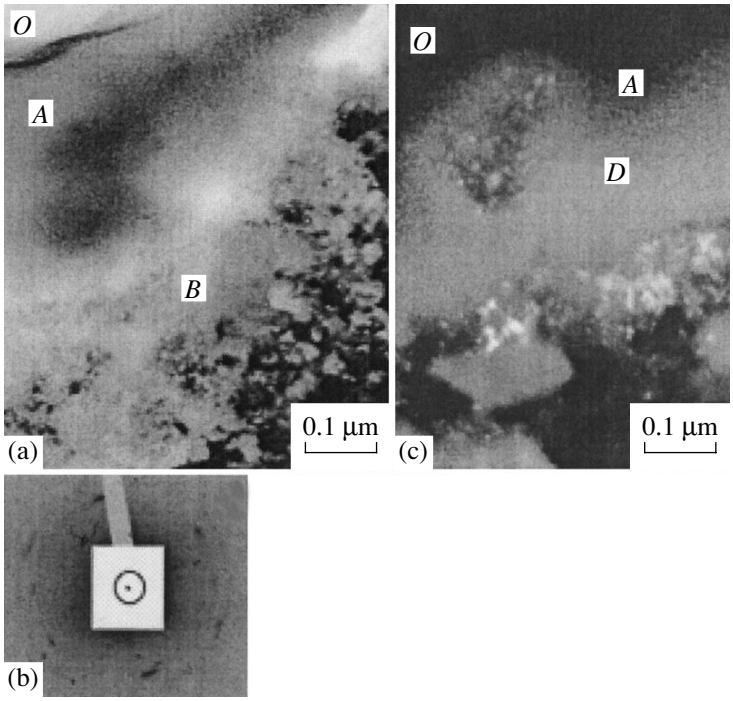

Fig. 2. (a) The same as in Fig. 1a, but after friction with the same lubricant oil containing 5% C_{60} (*O* indicating the hole; *A*, a ~1000-Å-thick film; *B*, a near-surface copper layer without block structure); (b) a typical electron diffraction pattern from the film *A* (diffraction brightness index, 120); (c) a dark-field image of the film *A* (in superimposed 200 Cu_2O and 111 copper lattice reflections) showing inclusions of wear particles *D*.

by the conditions of heat removal being less favorable in thicker films.

The electron diffraction reflections from the protective film and the near-surface copper layer (Fig. 2b) correspond to a textured Cu_2O [111] lattice (with an interplanar spacing of 2.45 Å). The dark field image of the film (Fig. 2c) obtained in the 111 copper lattice and 200 cuprous oxide lattice reflections (the two reflections strongly overlap) displays the inclusions of finely dispersed particles with dimensions between ~100 and ~1000 Å. These are probably the wear particles formed from an oxidized surface material in the initial friction stage.

The electron diffraction patterns exhibit no signals characteristic of the crystalline state of fullerene C_{60} or the related compounds. However, this by no means

implies that the fullerene does not participate in the film formation. On the contrary, the fullerene molecules apparently act as the agents initiating the tribopolymerization process (this circumstance explains the easy formation and considerable thickness of the film) [3, 7]. The fact that the film is insoluble in toluene indicates that it most likely comprises a network of hydrocarbon molecules in which the C_{60} molecules may play the role of junctions or the centers of agglomerates (of the molecular coil type) formed of the hydrocarbon lubricant molecules.

Thus, the results of this study confirmed the previously proposed model [4] of the two-layer surface structure formed on a copper counterbody in the "wearless" friction regime. This structure, comprising a thin tribopolymer film above a layer of friction-modified finely dispersed copper, is just what accounts for the protection of metals in the friction couple from fracture and wear by featuring the rotational modes during the shear deformation development on the friction surface. The amorphous surface film formed in the presence of fullerene C_{60} is ten times thicker than that in the previous case. This thick protective film simultaneously performs several functions, preventing the surface mass transfer, reducing the friction coefficients, and accepting the shear stresses arising during friction (rather than transferring stress to the underlying metal layers). This is possible, in particular, provided that there is a fine surface film containing structural elements capable of converting the shear deformation into rotational modes. This role is probably performed by molecular coils formed around fullerene molecules.

Therefore, a positive effect of the fullerene additive in a base lubricant oil consists in facilitating the formation of such a single-layer protective structure during friction. This process developing more readily than fragmentation of the metal surface, the "wearless" friction regime is more easily attained in the presence of fullerene [1, 2].

REFERENCES

1. O. F. Kireenko, B. M. Ginzburg, V. P. Bulatov, and V. P. Budtov, Trenie i Iznos **20** (4), 400 (1999).
2. B. M. Ginzburg, O. F. Kireenko, M. V. Baĭdakova, and V. A. Solov'ev, Zh. Tekh. Fiz. **69** (11), 113 (1999) [Tech. Phys. **44**, 1367 (1999)].
3. B. M. Ginzburg, M. V. Baĭdakova, D. G. Tochil'nikov, *et al.*, Zh. Tekh. Fiz. **70** (12), 87 (2000) [Tech. Phys. **45**, 1595 (2000)].
4. O. F. Kireenko, Trenie i Iznos **14** (1), 85 (1993).
5. A. I. Berdenikov and O. F. Kireenko, in *The Physics of Wear-Resistant Metal Surfaces. A Collection of Papers* (Fiz.-Tekh. Inst., Leningrad, 1988), pp. 183–187.
6. Yu. S. Zaslavskiĭ and R. N. Zaslavskiĭ, *Antiwear Oil Additives: Principle of Operation* (Khimiya, Moscow, 1978).
7. A. A. Shepelevskiĭ, L. A. Shibaev, B. M. Ginzburg, and V. P. Bulatov, Zh. Prikl. Khim. (St. Petersburg) **72** (7), 1198 (1999).

Translated by P. Pozdeev

Technical Physics Letters, Vol. 27, No. 10, 2001, pp. 868–870. Translated from Pis'ma v Zhurnal Tekhnicheskoĭ Fiziki, Vol. 27, No. 20, 2001, pp. 51–56.

A New Method for Determining the Sharpness of InGaAs/GaAs Heterojunctions by Auger Depth Profiling

M. N. Drozdov, V. M. Danil'tsev, Yu. N. Drozdov, O. I. Khrykin, and V. I. Shashkin

Institute for Physics of Microstructures, Russian Academy of Sciences, Nizhni Novgorod, Russia

e-mail: drm@ipm.sci-nnov.ru

Received May 3, 2001

Abstract—It is established for the first time that the phenomenon of ion-stimulated surface segregation can be used to increase the depth resolution of Auger profiling during analysis of the $In_xGa_{1-x}As/GaAs$ heterostructures. It is demonstrated that, by varying the energy of the sputtering Ar^+ ion beam from 1 to 0.5 keV in the region of the GaAs/InGaAs heterojunction, the junction sharpness can be estimated at a resolution on the order of 0.5 nm determined by a difference in the projected range of Ar^+ ions and independent of the escape depth of the Auger electrons. *© 2001 MAIK "Nauka/Interperiodica".*

Introduction. Informativity of the elemental depth profiling of structures by Auger spectroscopy in combination with ion sputtering depends to a considerable extent on the depth resolution (ΔZ) achieved during the analysis of each particular junction. Under optimum ion sputtering conditions, the depth resolution is determined by the escape depth of Auger electrons and by the artifacts of ion sputtering in the collision cascades. For a low-energy (below 1 keV) ion beam used in the sputtering stage, the limiting ΔZ is 1–1.2 nm [1, 2].

In the case of semiconductor structures, where the ΔZ value is additionally influenced by the ion-stimulated diffusion and segregation processes, the limiting ΔZ value increases to 1.5–2 nm. From the standpoint of investigation of the semiconductor structures with heterojunctions, this is a significant drawback since the ΔZ value is considerably greater than the characteristic size of structural inhomogeneities. As a result, the method fails to distinguish between structures fabricated under different conditions if the differences fall within the ΔZ limits.

Hofmann [2] suggested that, in systems featuring the ion-stimulated segregation, the directed transfer of atoms from a subsurface layer toward the surface may compensate for the sputter front smearing as a result of the atomic mixing in the collision cascades and the diffusion processes. This phenomenon might lead to a rather curious situation, whereby the depth resolution is improved by the ion-stimulated processes. However, this effect was never observed in practice. We believe that the positive (from the standpoint of depth profiling) influence of the segregation is masked by the effect of preferential sputtering: the atoms of elements more susceptible to segregation typically possess greater sputtering coefficients and are selectively removed from the surface [3, 4].

Below, we propose a new approach to the Auger depth profiling of structures with sharp junctions, which allows a positive influence of the directed transfer of atoms toward the surface as a result of the ion-stimulated segregation to be manifested. The idea of the new approach is to vary the energy of the sputtering ion beam used for the depth profiling immediately in the region of sharp changes in the elemental profiles. Variation of the ion beam energy during sputtering of the surface of homogeneous multicomponent materials was employed for a long time in analysis of the mechanisms of the ion–surface interaction [5, 6]. Using this method, it is possible to separate various phenomena (possessing a dissimilar character of the nonstationary response) such as the preferential sputtering, recoil implantation, atomic mixing in collision cascades, and radiation-stimulated diffusion and segregation processes.

In the application to inhomogeneous structures, this approach can be considered as a nonstationary method of depth profiling in which a change in the sputtering ion energy is used to modify the depth resolution function within certain layers and, hence, to separate the contribution due to the real elemental profile of the inhomogeneous structure. To our knowledge, this possibility was never considered in the literature. We may only point to the investigations [7, 8] where the ion beams of variable energy were employed for the depth profiling of multilayer Mo/Si and Ge/Si structures in order to identify the ion sputtering artifacts (atomic mixing and surface roughness development).

Experimental. We have studied a series of multilayer heterostructures of the $GaAs/In_xGa_{1-x}As/GaAs$ system with quantum wells. The samples were prepared by metalorganic vapor phase epitaxy in various growth regimes. Typical structures were represented by

H142 and H341 samples with the $In_xGa_{1-x}As$ layer thickness of 10 and 7 nm, respectively, and $x = 0.12$.

The depth profiling analysis was performed in an ESO-3 Auger electron spectrometer, in which the sputtering was effected by 0.5- or 1-keV Ar^+ ions incident at an angle of 38° relative to the sample surface normal. Details of the Auger profiling procedure were described previously [9, 10]. The sputtering velocity was calibrated using specially prepared multilayer test structures of the $In_xGa_{1-x}As/GaAs$ type with the layer thickness determined using the X-ray diffraction measurements (DRON-4 diffractometer).

Results and discussion. Figures 1a and 1b show typical In Auger depth profiles in the semiconductor heterostructures studied. Despite different growth conditions for the H142 and H341 samples, the profiles of indium distribution in the two cases are much alike. The widths of In junctions between the levels of 0.2 and 0.8 of the maximum in Figs. 1a and 1b is 1.4–1.6 nm. The traditional Auger depth profiling cannot provide for a better accuracy in determining the sharpness of junctions. Figures 2a and 2b show the indium distribution in the same structures measured with the sputtering ion energy switched from 1 to 0.5 keV in the vicinity of the first (facing surface) front of the InGaAs layer. As is seen, the profiles of In in H142 and H341 samples observed in this case are significantly different. The former sample analyzed using a decreased sputtering ion beam energy shows an additional indium peak with sharp decay at a depth on the order of and below 1 nm. This was not the only case: a similar behavior of In was observed upon the energy variation in some other sample heterostructures. The distribution of In in H341 is significantly different: measured with the ion energy variation in the same region as in Fig. 2a, the profile in Fig. 2b only shows a somewhat lower slope of the first front.

In our opinion, the observed behavior of In is related to the effect of ion-stimulated segregation of In atoms in the course of the depth profiling. The transfer of atoms involved in the ion-stimulated phenomena takes place within a near-surface layer with a thickness on the order of the ion diffusion path. The minimum diffusion path coincides with the collision cascade length, which is close to the projected ion range L_P.

During the depth profiling with a 1-keV ion beam, In atoms appear on the sputtered surface of GaAs when the sputter crater front approaches the InGaAs layer to a distance of $L_P^{(1)}$. The concentration of In on the sample surface is determined by competition of the opposite effects of In segregation and preferential sputtering [4]. The measured In peak intensity is determined by depth-averaged yield of the corresponding Auger electrons.

Upon the stepwise change of the ion energy from 1 to 0.5 keV, the projected range decreases to $L_P^{(2)}$. In the case of a sharp heterojunction, the region featuring the ion-stimulated transfer of In atoms will not reach the

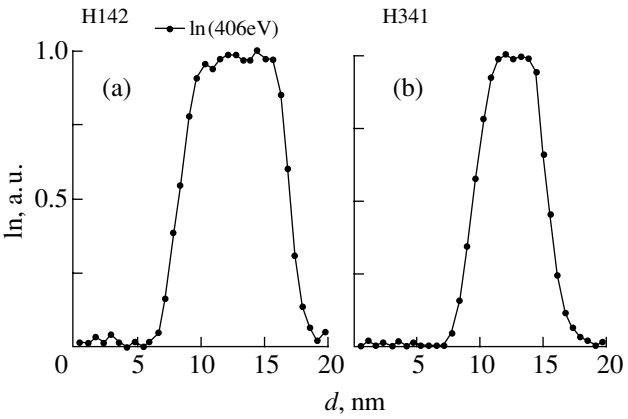

Fig. 1. Auger depth profiles of In in (a) H142 and (b) H341 samples of a InGaAs/GaAs heterostructure measured with a constant Ar ion sputtering energy of 0.5 keV.

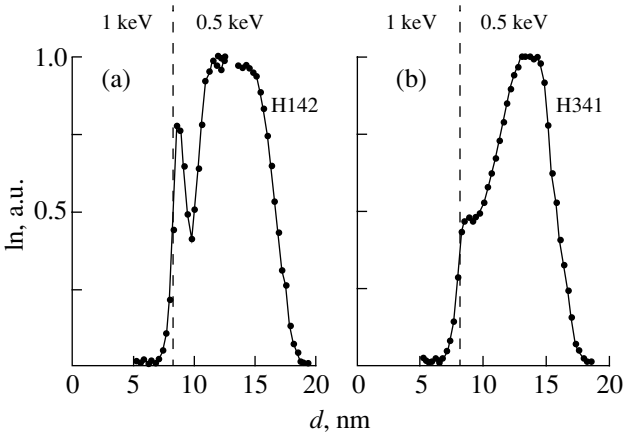

Fig. 2. Auger depth profiles of In in (a) H142 and (b) H341 sample structures measured with the Ar ion sputtering energy changed from 1 to 0.5 keV in the region of the first front of the InGaAs layer.

InGaAs layer. This results in a sharp drop in the In peak intensity, which begins to increase only upon removal of an additional layer of GaAs (Fig. 2a). After a drop in the surface concentration of In, the preferential sputtering of In atoms is no longer a compensating factor determining the profile shape as mentioned above. In the case of a smooth junction, the decrease in L_P leads to no significant changes in the In profile (Fig. 2b) because of a small In concentration gradient in the region corresponding to the ion projected ranges $L_P^{(2)}$ and $L_P^{(1)}$.

Thus, a characteristic depth resolution scale in the proposed method of Auger depth profiling is on the order of the difference between $L_P^{(2)}$ and $L_P^{(1)}$, which is not related to the yield depth of Auger electrons. According to [11, 12], for Ar^+ ions with the energies of 1 and 0.5 keV this difference amounts to about 0.5 nm. The profiles in Figs 2a and 2b allow us unambiguously

distinguishing between H142 and H341 samples: the heterojunction width in the former structure is smaller and that in the latter structure is greater than this characteristic length. Note that the proposed method of depth profiling only estimates the sharpness of a junction, rather than the exact profile shape. The distribution of elements in the region of the heterojunction can be restored by mathematical processing of the experimental profile with an allowance for the depth resolution function. The necessary investigation of the ion-stimulated phenomena taking place in semiconductor heterostructures and the influence of these processes on the results of Auger depth profiling is in progress.

Conclusion. We have observed for the first time the effect of sharp increase and decay in the In depth–concentration profiles of GaAs/$In_xGa_{1-x}As$/GaAs heterostructures on a resolution scale below than 1 nm, which was related to a stepwise change in the sputtering ion energy from 1 to 0.5 keV in the region of the heterojunctions. The effect is interpreted as a manifestation of the ion-stimulated segregation phenomenon—a directed transfer of In atoms toward the surface in the course of the sputtering front passage through the heterojunction region. The proposed method of nonstationary Auger depth profiling allows the heterojunction sharpness to be estimated on a level of the order of $L_P^{(1)} - L_P^{(2)} \approx 0.5$ nm not related to the escape depth of Auger electrons. On this level, it is possible to distinguish between heterojunctions showing close elemental profiles during the traditional Auger depth profiling with a constant ion sputtering energy. Of course, this new approach is effective only in the analysis of structures featuring significant manifestations of the ion-stimulated segregation phenomena. However, the class of such structures is rather wide and includes, besides the InGaAs/GaAs system, many other semiconductor heterostructures such as AlGaAs/GaAs and Ge/Si, as well as multilayer structures with metals.

Acknowledgments. This study was supported by the Russian Foundation for Basic Research (project nos. 99-02-18037 and 00-02-16141) and by the Federal Program “Surface Atomic Structures.”

REFERENCES

1. S. Hofmann, Rep. Prog. Phys. **61**, 827 (1998).
2. S. Hofmann, J. Vac. Sci. Technol. A **9** (3), 1466 (1991).
3. N. Q. Lam, Surf. Interface Anal. **12** (1), 65 (1988).
4. R. Kelly, Surf. Interface Anal. **7** (1), 1 (1985).
5. G. Betz and G. K. Wehner, in *Topics in Applied Physics*, Vol. 52: *Sputtering by Particle Bombardment II*, Ed. by R. Behrisch (Springer-Verlag, Berlin, 1983; Mir, Moscow, 1986), Chap. 2.
6. J. B. Malherbe, Crit. Rev. Solid State Mater. Sci. **19** (3), 129 (1994).
7. A. Koncol, A. Sulyok, M. Menyhard, and A. Barna, J. Vac. Sci. Technol. A **12** (2), 436 (1994).
8. M. Menyhard, A. Barna, J. P. Biersack, *et al.*, J. Vac. Sci. Technol. A **13** (4), 1999 (1995).
9. M. N. Drozdov, V. M. Danil’tsev, Yu. N. Drozdov, *et al.*, Pis’ma Zh. Tekh. Fiz. **22** (4), 61 (1996) [Tech. Phys. Lett. **22**, 761 (1996)].
10. M. N. Drozdov, V. M. Danil’tsev, N. N. Salashchenko, *et al.*, Pis’ma Zh. Tekh. Fiz. **21** (18), 1 (1995) [Tech. Phys. Lett. **21**, 725 (1995)].
11. K. Wittmaack, Vacuum **34** (1-2), 119 (1984).
12. S. Hofmann, Surf. Interface Anal. **21**, 673 (1994).

Translated by P. Pozdeev

Technical Physics Letters, Vol. 27, No. 10, 2001, pp. 871–872. Translated from Pis'ma v Zhurnal Tekhnicheskoĭ Fiziki, Vol. 27, No. 20, 2001, pp. 57–60.

The Avalanche Multiplication of Electrons and Holes in Cadmium Telluride

N. V. Demich and V. P. Makhniĭ

Chernovtsy National University, Chernovtsy, Ukraine

e-mail: oe-dpt@chnu.cv.ua

Received May 12, 2001

Abstract—It is experimentally demonstrated that the process of impact ionization in cadmium telluride crystals is stimulated by holes. The ratio of the impact ionization coefficients of holes (α_p) and electrons (α_n) amounts to $\alpha_p/\alpha_n \approx 30$–$40$. © *2001 MAIK "Nauka/Interperiodica".*

The extensive development of optoelectronics led to the need in fast-response photodetectors highly sensitive in a certain spectral range, which is achieved by means of the internal photocurrent amplification. Avalanche photodiodes representing this class of optoelectronic devices are most frequently based on Ge, Si, and A^3B^5 semiconductor compounds [1]. To provide for a minimum internal noise level in these photodiodes, it is necessary to use materials possessing a maximum difference between the impact ionization coefficients of holes (α_p) and electrons (α_n) [2]. Unfortunately, this criterion fails to be valid in GaAs, the compound most widely used in optoelectronics, which is characterized by $\alpha_n \approx \alpha_p$ [3]. The purpose of this study was to determine the α_n/α_p ratio in cadmium telluride, a compound many properties of which are much like those of gallium arsenide.

The avalanche processes in diode structures are most frequently studied by analyzing their photoelectric characteristics measured in a negative bias regime [4]. In practice, the amplification coefficient M is usually determined as the ratio of the photocurrent $I_p(V)$ at a given voltage V to the value I_{p0} for which no internal gain takes place. Figure 1 shows the $I_p(V)$ curves for two surface-barrier diodes fabricated using materials possessing close values of the free carrier density but belonging to different conductivity types. The devices were illuminated trough a transparent rectifying contact by a total (nonmonochromatic) light of an incandescent tungsten-filament lamp. Note that a sharp increase in the photocurrent beginning at a certain voltage is not related to the light-induced heating of the samples, since the shape of the $I_p(V)$ curves remains the same when the light intensity varies by several orders of magnitude.

A particular shape of the $M(V)$ characteristic is determined by the mode of potential variation in the photodiode space-charge region and by the ratio of α_n and α_p [4]. For a sharp surface barrier and strongly different impact ionization coefficients, the amplification coefficient is

$$M = \exp\left[a\exp\left(-\frac{b}{\varphi_0 - eV}\right)\right], \quad (1)$$

while for $\alpha_n = \alpha_p$ we obtain a relationship

$$N = 1 - M^{-1} = a\exp\left(-\frac{b}{\varphi_0 - eV}\right), \quad (2)$$

where N is the ionization coefficient. The voltage-independent quantities a and b are determined by parameters of the material and the diode structure. According to [4], the b/a ratio determines to the first approximation the impact ionization threshold energy E_i, the experimental value of which in CdTe at 300 K is ~2 eV [5]. A comparison of the experimental $M(V)$ plots to the relationships (1) and (2) shows a better coincidence with the theory assuming that α_n and α_p strongly different. This result is consistent with the conclusions made in

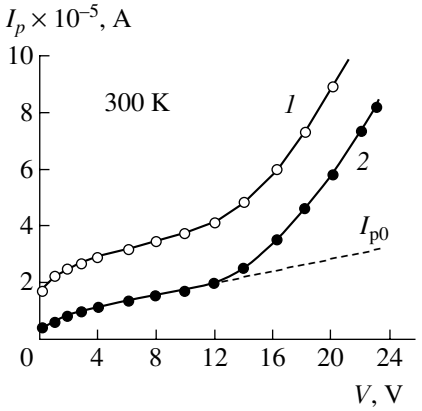

Fig. 1. Plots of the room-temperature photocurrent $I_p(V)$ versus reverse bias voltage V for (*1*) ITO–*p*-CdTe and (*2*) *i*-Au–*n*-CdTe surface-barrier diodes.

1063-7850/01/2710-0871$21.00 © 2001 MAIK "Nauka/Interperiodica"

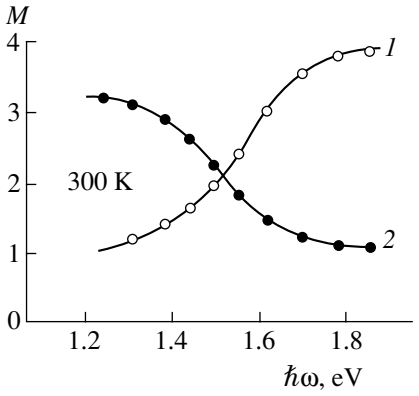

Fig. 2. The room-temperature spectral dependence of the amplification coefficient M for (*1*) ITO–*p*-CdTe and (*2*) *i*-Au–*n*-CdTe surface-barrier diodes.

[5], but the question as to which type of carriers dominates in the impact ionization process remains open.

To elucidate this question, we have additionally studied the spectral dependence of the amplification coefficient as it was done by Baranov *et al.* [6] for a variband *p*–*n* structure based on the $Ga_{1-x}Al_xSb_{1-y}As_y$ system. The photon energy dependence $M(\hbar\omega)$ in our case (Fig. 2) is related to a difference in the photocurrent contributions due to the charge carriers produced in different regions of the surface-barrier diode structure. Let us analyze this difference in more detail for a structure of the Au–*n*-CdTe type. In this system, the high-energy photons with $\hbar\omega$ exceeding the semiconductor bandgap width E_g are absorbed on the surface and, hence, only electrons can penetrate through a strong field region in the structure with "plus" on the base substrate, while holes sink to the gold "minus" contact. Under these conditions, only electrons participate in the impact ionization process for $M \le 2$. For $\hbar\omega < E_g$, the charge carriers are generated at the boundary between the space-charge region and a quasineutral base region. Hence, only holes can penetrate through the strong field region and produce the impact ionization. The opposite situation takes place in structures of the ITO–*p*-CdTe type, where holes produce the impact ionization for $\hbar\omega > E_g$ and electrons, for $\hbar\omega < E_g$. An analysis of the data presented in Fig. 2 shows that α_p is greater than α_n in cadmium telluride. In order to quantitatively estimate the α_p/α_n ratio, we can use a relationship obtained in [6]:

$$\frac{\alpha_p}{\alpha_n} = \frac{M_p - 1}{M_n - 1}. \quad (3)$$

For the M_n and M_p values from the corresponding saturation regions, formula (3) yields $\alpha_p/\alpha_n \approx 30$–$40$.

Thus, the process of avalanche amplification in cadmium telluride crystals is stimulated by holes. This circumstance has to be taken into account in the development of avalanche photodiodes based on this material. In particular, a low internal noise level and a high product of the amplification coefficient by the bandgap width in the Schottky barrier avalanche photodiodes are more readily achieved with *p*-CdTe. Optimization of the other important parameters of these photodetectors (as well as those based on the different barrier type) needs special consideration that goes beyond the framework of this communication.

REFERENCES

1. S. Sze, *Physics of Semiconductor Devices* (Wiley, New York, 1981; Mir, Moscow, 1984).
2. R. I. McInture, IEEE Trans. Electron Devices **ED-13**, 164 (1996).
3. R. A. Logan and S. M. Sze, J. Phys. Soc. Jpn., Suppl. **21**, 434 (1966).
4. I. K. Vereshchagin, *Electroluminescence of Crystals* (Nauka, Moscow, 1974).
5. V. P. Makhniĭ, Fiz. Élektron. **35**, 23 (1987).
6. A. N. Baranov, T. N. Danilova, A. N. Imenkov, *et al.*, Fiz. Tekh. Poluprovodn. (Leningrad) **17** (4), 753 (1983) [Sov. Phys. Semicond. **17**, 473 (1983)].

Translated by P. Pozdeev

Technical Physics Letters, Vol. 27, No. 10, 2001, pp. 873–874. Translated from Pis'ma v Zhurnal Tekhnicheskoĭ Fiziki, Vol. 27, No. 20, 2001, pp. 61–64.

Phase Transitions in $Li_{0.13}Na_{0.87}NbO_3$ Crystals

E. A. Dul'kin*, L. V. Grebenkina, and V. G. Gavrilyachenko*****

** Advanced School of Applied Science, The Hebrew University of Jerusalem, Jerusalem, 91904 Israel*
*** Institute of Mechanics and Applied Mathematics, Rostov State University, Rostov-on-Don, 344104 Russia*
**** Rostov State University, Rostov-on-Don, 344104 Russia*

Received April 3, 2001

Abstract—$Li_{0.13}Na_{0.87}NbO_3$ crystals were studied by dilatometric, dielectric, acoustic emission, and optical methods on heating in a temperature range from 20 to 700°C. Based on the results of these measurements, the following sequence of phases was established: 20–350°C, ferroelectric orthorhombic *Pmm*2; 350–400°C, ferroelectric orthorhombic *Pmmm*; 400–630°C, ferroelectric tetragonal, 14/*mmm*; above 630°C, cubic *Pm*3*m*. The latter two transformations can be classified as second-order ferroelectric phase transitions. © *2001 MAIK "Nauka/Interperiodica".*

Solid solutions of the $(1 - X)NaNbO_3$–$XLiNbO_3$ system have drawn the attention of researchers by exhibiting a number of various phase transitions and by possessing pyro- and piezoelectric properties promising from the standpoint of practical applications. Both ceramic [1–4] and single crystal [5, 6] samples were studied. The temperature intervals of phases existing in the ceramics with $0 < X < 0.145$ (corresponding to the complete solubility of $LiNbO_3$ in $NaNbO_3$) were determined in [1, 2]. According to the data for $X = 0.13$ reported in [1], the phases change from monoclinic (0–100°C) to tetragonal (100–400°C) and cubic (above 400°C). A different sequence was established in [2], where the stable phases changed from ferroelectric orthorhombic (0–350°C) to paraelectric orthorhombic (350–400°C), tetragonal (400–450°C), "contracted" cubic (450–630°C), and cubic (above 630°C). Thus, there is an obvious discrepancy between the experimental results reported in [1, 2].

In recent years, the phase transitions have been successfully studied, in addition to the traditional methods based on the dilatometric, dielectric, and optical measurements, by the method of acoustic emission (AE). Using this technique, it is possible to determine the Curie temperature (T_C) with sufficient accuracy and estimate the degree of coherency of the adjacent phases [7].

The purpose of this study was to reveal the phase transitions and determine the sequence of phases in $Li_{0.13}Na_{0.87}NbO_3$ crystals using dilatometric, dielectric, optical, and AE measurements.

The experiments were performed on thin plates cut from $Li_{0.13}Na_{0.87}NbO_3$ crystal ingots (kindly provided by Prof. M.F. Kupriyanov), with large faces parallel to (001) crystal faces of the initial setting. Most of the plates were of a milk white color, but there were some exhibiting sufficiently large colorless transparent regions in which the domain structure could be observed.

The relative dilatancy ($\Delta L/L$) and the AE activity ($\dot{N}$) were simultaneously measured in the course of heating the crystal plates to 700°C using a combined method described in [8]. In parallel, the permittivity ε was measured by a bridge technique at a frequency of 20 kHz. The results of these measurements are presented in the figure.

The domain structure was observed in both transmitted and reflected polarized light [9]. The room-temperature domain structure is usually highly involved,

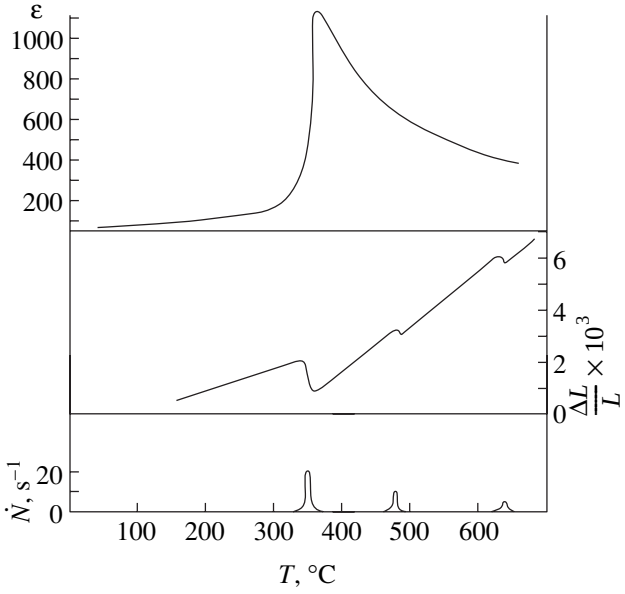

Temperature variation of the permittivity ε, relative dilatancy $\Delta L/L$, and AE activity $\dot{N}$ in $Li_{0.13}Na_{0.87}NbO_3$ crystals heated in the temperature range from 20 to 700°C.

1063-7850/01/2710-0873$21.00 © 2001 MAIK "Nauka/Interperiodica"

representing a large number of small wedge-shaped 90° and 60° twins (characteristic of an orthorhombic phase) randomly distributed over the crystal volume. At room temperature, the coercive field is $E_c = 1.4 \times 10^6$ V Ω^{-1}; the spontaneous polarization exhibits a large scatter within $(3–10) \times 10^{-2}$ K m^2, which can be related to the involved domain structure.

In the course of heating to 350°C, the ferroelectric phase remains stable and the domain structure changes insignificantly. At T = 350°C, the ε value exhibits a characteristic maximum and then falls according to the Curie–Weiss law with a constant of $C = (1.5–2.5) \times 10^5$ K. The maximum in permittivity is accompanied by a jump in the crystal dilatancy (characteristic of the first-order phase transition) and by the acoustic emission. The AE signal measured reflects rearrangement of the domain structure with the formation of a new phase (also orthorhombic, as evidenced by the twin boundary orientation).

As the heating is continued to T = 480°C, another phase transition takes place with the formation of a new phase, which is tetragonal judging by the presence of 90° twins. Upon this phase transition, the twins increase in size (frequently, acquiring a platelike morphology) and the crystals become transparent. Apparently, the initial milk white color of the crystals is due to the light scattering from numerous boundaries of fine orthorhombic twins. The phase transition at 480°C is accompanied by a small dilatancy jump and an acoustic emission related to the corresponding domain structure rearrangement.

On heating to 630°C, the crystal experiences the transition to a cubic phase. During this phase transition, some crystals exhibit moving planar interphase boundaries with an orientation close to (110). The presence of boundaries with this orientation is indicative of an almost coherent matching between phases. For this reason, the accompanying AE signal is weak, while the corresponding dilatancy jump is quite large. It should be noted that the last two transitions lead to no dielectric anomalies and, hence, can be classified as the first-order ferroelectric phase transitions.

Thus, the results of our investigation suggest the following sequence of stable phases in $Li_{0.13}Na_{0.87}NbO_3$ crystals heated in the temperature range from 20 to 700°C: 20–350°C, ferroelectric orthorhombic *Pmm*2; 350–400°C, ferroelectric orthorhombic *Pmmm*; 400–630°C, ferroelectric tetragonal 14/mmm; above 630°C, cubic *Pm*3*m*.

REFERENCES

1. T. Nitta, J. Am. Ceram. Soc. **51**, 626 (1968).
2. L. A. Reznichenko and L. A. Shilkina, Izv. Akad. Nauk SSSR, Ser. Fiz. **39** (5), 1118 (1975).
3. L. Pardo, P. Duran-Marth, I. P. Mercurio, *et al.*, J. Phys. Chem. Solids **9**, 1335 (1997).
4. I. V. Pozdnyakova, L. A. Reznichenko, and V. G. Gavrilyachenko, Pis'ma Zh. Tekh. Fiz. **25** (18), 81 (1999) [Tech. Phys. Lett. **25**, 752 (1999)].
5. P. L. Zhang, W. L. Zhong, H. S. Zhao, *et al.*, Solid State Commun. **67**, 1215 (1988).
6. I. B. Kim and I. N. Kim, J. Appl. Phys. **76**, 1983 (1994).
7. E. A. Dul'kin, Mater. Res. Innovations **2**, 338 (1999).
8. E. A. Dul'kin, Sverkhprovodimost: Fiz., Khim., Tekh. **5** (1), 103 (1992).
9. E. A. Dul'kin, V. G. Gavrilyachenko, and A. F. Semenchev, Fiz. Tverd. Tela (St. Petersburg) **34** (5), 1628 (1992) [Sov. Phys. Solid State **34**, 863 (1992)].

Translated by P. Pozdeev

Technical Physics Letters, Vol. 27, No. 10, 2001, pp. 875–877. Translated from Pis'ma v Zhurnal Tekhnicheskoĭ Fiziki, Vol. 27, No. 20, 2001, pp. 65–71.

Electromagnetic Radiation of a Nonlinearly Oscillating Charged Drop

S. O. Shiryaeva, A. I. Grigor'ev, D. F. Belonozhko, and A. S. Golovanov

Yaroslavl State University, Yaroslavl, 150000 Russia

e-mail: shir@uniyar.ac.ru

Received May 31, 2001

Abstract—Nonlinear oscillations of a charged drop caused by a multimode initial deformation of the equilibrium spherical shape are studied using an asymptotic analytical technique. It is shown that, when the spectrum of modes describing the initial deformation contains two adjacent modes, the center of the drop charge oscillates near the center of mass, which causes the generation of an electromagnetic radiation of the dipole type. © *2001 MAIK "Nauka/Interperiodica".*

1. Investigation of the capillary oscillations and stability of a charged drop is of great interest both in basic research and in numerous technological applications where charged drops play an important role (see, e.g., [1–3] and references therein). In particular, problems related to the generation of an electromagnetic radiation by oscillating charged drops in clouds and rains may be of interest in the radar sounding of meteorological objects [4]. Earlier, the electromagnetic radiation generated by oscillating drops was studied using a linear approximation for the drop deformation [5]. As to the nonlinear approximations, only a general analysis of oscillations of a charged drop has so far been performed (see, e.g., [6–9]) without studying the electromagnetic radiation.

2. Let us consider the time evolution of the surface of a perfect incompressible liquid drop with the density ρ and the surface tension coefficient σ. Assume that the drop with the total charge Q is placed in a vacuum; the drop volume equals that of a sphere of radius R. At the initial time instant $t = 0$, the equilibrium spherical drop is subjected to a virtual axisymmetric perturbation of a fixed amplitude that is substantially smaller than the drop radius.

Since the initial perturbation of the drop surface is axisymmetric and small, we assume that the initial axial symmetry of the drop shape is retained throughout the process and the equation of the drop surface in a polar coordinate system with the origin placed at the drop center is

$$r(\theta, t) = 1 + \xi(\theta, t), \quad |\xi| \ll 1.$$

We use dimensionless variables in which $R = \rho = \sigma = 1$.

Assume that the motion of liquid in the drop is potential and the velocity field of the liquid, $V(\mathbf{r}, t) = \nabla\psi(\mathbf{r}, t)$ is entirely determined by the velocity potential function $\psi(\mathbf{r}, t)$. Mathematically, the problem of electromagnetic radiation of an oscillating drop is formulated as follows:

$$\Delta\psi(\mathbf{r}, t) = 0; \quad \Delta\mathbf{E}(\mathbf{r}, t) = \frac{1}{c^2}\frac{\partial^2\mathbf{E}}{\partial t^2}; \quad \mathrm{div}\mathbf{E} = 0;$$

$$r \longrightarrow 0: \psi(\mathbf{r}, t) \longrightarrow 0;$$

$$r \longrightarrow \infty: \mathbf{E}(\mathbf{r}, t) \longrightarrow 0;$$

$$r = 1 + \xi(\theta, t): \frac{\partial\xi}{\partial t} = \frac{\partial\psi}{\partial r} - \frac{1}{r^2}\frac{\partial\xi}{\partial\theta}\frac{\partial\psi}{\partial\theta};$$

$$\Delta p - \frac{\partial\psi}{\partial t} - \frac{1}{2}(\nabla\psi)^2 + \frac{1}{8\pi}(\mathbf{E})^2 = \nabla\cdot\mathbf{n}.$$

In order to complete this system, we add the conditions of conservation of the total drop charge and the drop volume as well as the condition of immobility of the drop center of mass:

$$-\frac{1}{4\pi}\oint_S(\mathbf{n}\cdot\nabla\Phi)ds = Q,$$

$$S = [r = 1 + \xi(\theta, t), 0 \le \theta \le \pi, 0 \le \phi \le 2\pi];$$

$$\int_V r^2 dr\sin\theta d\theta d\phi = \frac{4}{3}\pi,$$

$$V = [0 \le r \le 1 + \xi(\theta, t), 0 \le \theta \le \pi, 0 \le \phi \le 2\pi];$$

$$\int_V \mathbf{e}_r\cdot r^3 dr\sin\theta d\theta d\phi = 0,$$

$$V = [0 \le r \le 1 + \xi(\theta, t), 0 \le \theta \le \pi, 0 \le \phi \le 2\pi].$$

The initial conditions are specified in the form of an

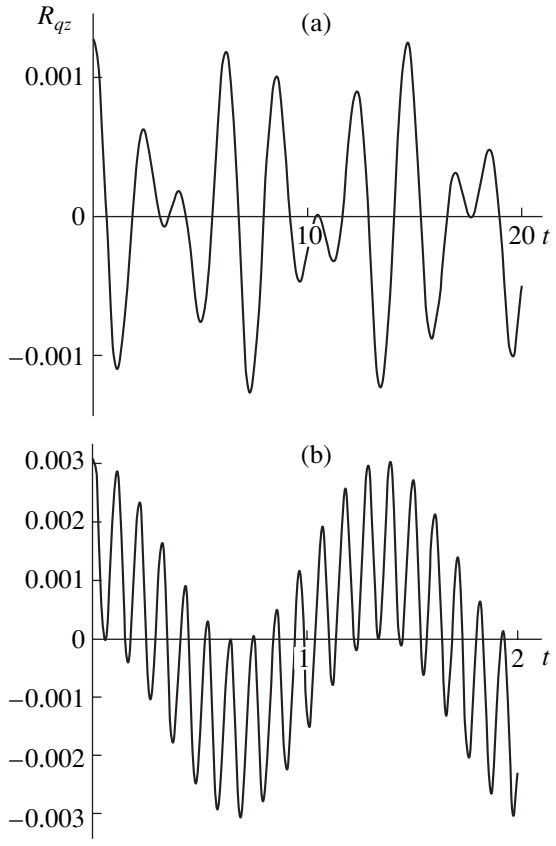

Fig. 1. The dimensionless shift of the center of charge of an oscillating drop with the radius R_{qz} caused by the excitation of translation mode ($j = 1$) vs. dimensionless time t. The initial deformations of the equilibrium spherical drop are specified as (a) $0.5\varepsilon(P_3(\mu) + P_4(\mu))$ and (b) $0.5\varepsilon(P_{10}(\mu) + P_{11}(\mu))$.

initial deformation of the equilibrium spherical drop and zero value of the initial velocity of the drop surface:

$$t = 0: \xi_0 P_0(\mu) + \xi_1 P_1(\mu) + \xi \sum_{j \in \Xi} h_j P_j(\mu);$$

$$\sum_{j \in \Xi} h_j = 1; \quad \frac{\partial \xi(\theta)}{\partial t} = 0;$$

where $\mu \equiv \cos\theta$, h_j are the dimensionless coefficients determining the contribution from various oscillation modes to the initial deformation of the drop surface, Ξ is the set of indices of excited modes, Δp is the difference of constant pressures inside and outside the equilibrium drop, **n** is the unit vector of the outer normal to the drop surface, $\mathbf{e}_r$ is the radial unit vector in the spherical coordinate system, **E** is the electric field of the intrinsic charge, ε is the amplitude of initial perturbation of the drop surface, $P_j(\mu)$ are the Legendre polynomials of order j, and ξ_0 and ξ_1 are the constants determined from the conditions of constant drop volume and immobile center of mass at the initial instant. The latter quantities can be expressed, to within terms of the second order of smallness in the amplitude ε, as

$$\xi_0 \approx -\varepsilon^2 \sum_{j \in \Xi} \frac{h_j^2}{(2j+1)} + O(\varepsilon^3);$$

$$\xi_1 \approx -\varepsilon^2 \sum_{j \in \Xi} \frac{9 j h_{j-1} h_j}{(2j-1)(2j+1)} + O(\varepsilon^3).$$

3. The problem formulated in Section 2 was solved in [5] using a linear approximation for the function $\xi(\theta, t)/R$. In this case, the problem reduces to the following dimensional dispersion relation for the system under study:

$$\omega_j^2 \equiv \frac{\sigma}{\rho R^3} j(j-1)\left[(j+2) - \frac{Q^2}{4\pi\sigma R^3}\right] + 2i\omega_j \frac{Q^2 (j-1)^2}{8\pi\rho c R^5},$$

where i is the imaginary unit. The imaginary part of the frequency obtained from the dispersion relation determines the decay of capillary oscillations in the drop related to the radiation of electromagnetic waves. An expression for the power radiated at the frequency ω_j can be written as [5]

$$I = -\frac{dW_j}{dt} \equiv W_j \frac{Q^2 (j-1)^2}{4\pi\rho c R^5}, \qquad (1)$$

where W_j is the energy of the jth surface oscillation mode.

In [5], it was assumed that principal radiators in a cloud are the free falling strongly charged drops with $R = 1$ mm which coagulate with smaller drops and, therefore, oscillate. The intensity of the integral multipole radiation (starting with the quadrupole radiation, because the dipole radiation cannot be detected in the linear approximation) estimated under this assumption at a frequency of 120 kHz for a 5-km-diameter cloud is about 30 mW. This figure seems to be a substantial overestimate since experimental values of the concentration and charge of large drops are significantly smaller than those used in [5] (see [10]).

4. Here, the problem is solved using the asymptotic multiscale method (application of this method to the analysis of stability of charged drops is detailed, e.g., in [6, 7, 9]) and retaining the terms of the second order of smallness in the function $\xi(\theta, t)/R$. The solution indicates that, when the spectrum excited at the initial instant contains two adjacent modes, the capillary oscillations of the drop give rise to a mode with $n = 1$ (the translation mode) and the center of the drop charge begins to oscillate about the center of mass. The dimensional time dependence of the amplitude of these oscillations is given by

$$R_q \equiv \varepsilon^2 R \sum_{k \in \Xi} \frac{3i(i-2)}{(2j-1)(2j+1)} h_j h_{j-1}$$

$$\times [\cos[(\omega_j + \omega_{j-1})t] + \cos[(\omega_j - \omega_{j-1})t]]; \quad (1)$$

$$\omega_j^2 \equiv \frac{\sigma}{\rho R^3} j(j-1)\left[(j+2) - \frac{Q^2}{4\pi\sigma R^3}\right].$$

The time variation of the position of the center of charge of an oscillating drop for different initial perturbations is shown in the figure.

Oscillations of the charge center make the drop a dipolelike radiator of electromagnetic waves. In accordance with the well-known expression [11], the intensity I_e of electromagnetic radiation of an isolated drop can be written in the form

$$I_e = \frac{4}{3c^3}\{\left|d_{\omega_j + \omega_{j+1}}\right|^2(\omega_j + \omega_{j+1})^4 + \left|d_{\omega_{j+1} - \omega_j}\right|^2(\omega_{j+1} + \omega_j)^4\}, \quad (2)$$

where c is the speed of light in vacuum and d_{ω_j} is the dipole moment of a drop oscillating with the frequency ω_j. In the case under study,

$$d_{\omega_j + \omega_{j+1}} \equiv d_{\omega_{j+1} - \omega_j} \equiv Q|R_q|$$

$$\equiv Q\varepsilon^2 R \sum_{j \in \Xi} \frac{3j(j-2)}{(2j-1)(2j+1)} h_j h_{j-1}$$

and expression (3) can be written as

$$I_e = \frac{4Q\varepsilon^2 R}{c^3} \sum_{j \in \Xi} \frac{j(j-2)h_j h_{j+1}}{(2j-1)(2j+1)} \times \{(\omega_j + \omega_{j+1})^4 + (\omega_{j+1} - \omega_j)^4\}. \quad (3)$$

Let us use formula (4) to estimate the intensity of a background electromagnetic radiation in the case when the appearance of a translation mode is related to the excitation of only two adjacent modes with $j = 100$ in a drop with the medium parameters $R = 30$ μm and $Q = 2.5 \times 10^5$ CGSE. According to the reference data [6], the concentration n of drops in a cumulus cloud approximately equals 10^3 cm^{-3}. Assume also that $\varepsilon^2 = 0.1$, $h_{100} = h_{101} = 0.5$, $\sigma = 73$ dyn/cm, and $\rho_1 = 1$ g/cm^3. Then, for a 5-km-diameter cloud, the intensity of the dipole electromagnetic radiation generated when the drop oscillations are caused by microphysical processes (coagulation with smaller drops, evaporation, condensation, and hydrodynamic and electric interaction of adjacent drops) running in the cloud equals

$$I \approx 10^{-6} W.$$

This electromagnetic radiation arises at frequencies of about several megahertz.

If we assume that the oscillations contain all modes with indices ranging from j to $j + m$, the integral radiation intensity increases approximately m times.

5. In conclusion, the background dipole electromagnetic radiation of natural and artificial clouds can be related to a nonlinear effect associated with terms of the second order of smallness: excitation of the translation mode in an oscillating charged drop in the case when the spectrum of oscillatory modes describing the initial deformation of the drop contains two adjacent modes.

Acknowledgments. This work was supported by the grant of the President of Russian Federation no. 00-15-9925.

REFERENCES

1. A. I. Grigor'ev and S. O. Shiryaeva, Izv. Akad. Nauk, Mekh. Zhidk. Gaza, No. 3, 3 (1994).
2. A. I. Grigor'ev, Zh. Tekh. Fiz. **70** (5), 22 (2000) [Tech. Phys. **45**, 543 (2000)].
3. D. F. Belonozhko and A. I. Grigor'ev, Élektrokhim. Obrab. Met., No. 4, 17 (2000).
4. L. G. Kachurin, *Physical Principles of Influence on Atmospheric Processes* (Gidrometeoizdat, Leningrad, 1990).
5. V. I. Kalechits, I. E. Nakhutin, and P. P. Poluéktov, Dokl. Akad. Nauk SSSR **262** (6), 1344 (1982).
6. N. A. Pelekasis, J. A. Tsamopoulos, and G. D. Manolis, Phys. Fluids A **2** (8), 1328 (1990).
7. Z. C. Feng, J. Fluid Mech. **333**, 1 (1997).
8. D. F. Belonozhko and A. I. Grigor'ev, Zh. Tekh. Fiz. **70** (8), 45 (2000) [Tech. Phys. **45**, 1001 (2000)].
9. S. O. Shiryaeva, Zh. Tekh. Fiz. **71** (2), 27 (2001) [Tech. Phys. **46**, 158 (2001)].
10. *Clouds and Cloud Atmosphere: Handbook*, Ed. by I. P. Mazin and A. Kh. Khrgian (Gidrometeoizdat, Leningrad, 1989).
11. L. D. Landau and E. M. Lifshitz, *The Classical Theory of Fields* (Nauka, Moscow, 1967; Pergamon, Oxford, 1975).

Translated by A. Kondrat'ev

Technical Physics Letters, Vol. 27, No. 10, 2001, pp. 878–880. Translated from Pis'ma v Zhurnal Tekhnicheskoĭ Fiziki, Vol. 27, No. 20, 2001, pp. 72–78.

The Effect of Centrifugal Phase Separation in Heterogeneous Systems of Immiscible Components under the Action of Scanning Laser Pulses

V. S. Golubev and F. Kh. Mirzoev

Institute for Problems of Laser and Information Technologies, Russian Academy of Sciences, Shatura, Russia
e-mail: mirzo@lazer.nictl.msk.su

Received May 4, 2001

Abstract—A gasdynamic model is proposed to describe the phase separation in heterogeneous systems of immiscible components under the action of scanning laser pulses in the channeled penetration mode. The model takes into account the motion of immiscible components in vortex flows of the melt under the action of centrifugal forces. The characteristic time of the process development and the size of separated microparticles are estimated. The analytical conditions for the appearance of the concentration separation are determined. © *2001 MAIK "Nauka/Interperiodica".*

As is known [1], the action of a high-power laser radiation on heterogeneous materials (in particular, composites) under certain conditions leads to the phase separation of components in the liquid phase (melt), which is retained during crystallization after termination of the laser action. The phase-separated regions, representing a kind of defect, significantly influences the physical and mechanical properties of the laser-processed heterogeneous material.

During solidification of the melted zone formed in a target as a result of the penetration of a high-power laser radiation forming a vapor–gas channel (e.g., in the course of laser welding), the melt features intensive vortex flows. The liquid velocities in these vortices may reach up to 10^2–10^3 cm/s [2–5].

There are several factors that can be responsible for the development of flows in the melt: (i) a thermocapillary drag of the surface layer of the liquid [5–7] followed by closing of the stream via the liquid volume (with the vortex formation); (ii) entrainment of the surface layer by the tangent momentum of a condensing vapor flow [5]; (iii) injection of a stream from the melt formed at the frontal wall of a vapor–gas channel into the melt bath, with a "step" (generated by a three-dimensional thermal field in the frontal zone on this wall [2–5]) moving along this stream from entrance to bottom of the channel [3, 5]; (iv) injection of a stream from the frontal wall of a vapor–gas channel into the melt bath, which is driven by momentum pulses of vapor pressure [5] arising in the vapor–gas channel under the action of microscopic droplets dropping into the channel from the melt surface [4, 5]. If the melt formed under the laser action is multicomponent, the solidified vapor–gas channel may contain the structures corresponding to such vortices existed in the melt.

The purpose of this study was (i) to elucidate a mechanism of the liquid-phase separation in heterogeneous materials based on immiscible components under the action of scanning laser beam and (ii) to develop a qualitative physical model of this phenomenon.

Let us consider a medium containing immiscible components A and B, representing a matrix (e.g., of the light component A) with dispersed microparticles (e.g., of the heavier component B), exposed to a high-power laser beam. The microparticles may possess the shape of droplets formed as a result of the cluster formation in the melt, followed by the diffusion coalescence of these droplets, so that the dimensions of such microparticles may range from 10^{-4} to 10^{-2} cm [1]. An example is offered by Pb microparticles in a Fe matrix [1]. Alternatively, the microparticles may represent solid species of the same dimensions composed of a more refractory material than the matrix (e.g., W in Fe).

If a melt containing the microparticles of insoluble impurity features vortex motions, the microparticles will be entrained (accelerated) first along the current lines (by the kinetic head of the flow of the main component A) and then toward the periphery of the vortex (by the centrifugal force). A stationary radial (relative to the vortex center) motion of the microparticles relative to the matrix A must be established within a sufficiently short time, the velocity of this motion being determined by a balance between the centrifugal force and a viscous hydrodynamic drag of the medium. The maximum size of entrained particles is determined by a relationship between the dynamic pressure of the matrix moving relative to the droplet and the Laplace pressure determined by the surface tension of the impurity droplet occurring in the matrix.

1063-7850/01/2710-0878$21.00

In the regions of contact between two adjacent vortices, the concentration of microparticles must increase, which would result (after the solidification) in the appearance of layers enriched with the impurity component B.

Now, we will obtain estimates for the characteristic times and velocities of the centrifugal phase separation of microparticles in the zones of vortex motion. Let v_m be the azimuthal velocity of the vortex motion of the main liquid component A; r_W, the characteristic vortex size; v_φ and v_p, the azimuthal and radial components of the microparticle, respectively; r_p, the characteristic particle size; ρ_L and ρ_p, the densities of liquid A and particle B, respectively; and ν, the kinematic viscosity of liquid A. The motion of an isolated microparticle in the radial direction is described by the equation

$$\frac{4}{3}\pi r_p^3 \rho_p \frac{dv_p}{dt} = F_r + \frac{4}{3}\pi r_p^3 \frac{(\rho_p - \rho_L)v_\varphi^2}{r}; \qquad (1)$$

the first term in the right-hand part of Eq. (1) describes the hydrodynamic drag of the spherical particle for the radial motion and the second term takes into account the effect of centrifugal forces.

The particle drag in the melt can be expressed as

$$F_r \cong \frac{1}{2}C_f^{(r)}\pi r_p^2 \rho_L |v_L - v_p|(v_L - v_p), \qquad (2)$$

where $C_f^{(r)}$ is the particle drag coefficient and v_L is the local radial velocity of the carrying liquid phase. For a Reynolds number $\mathrm{Re}_p = 2r_p|v_L - v_p|/\nu$ in the interval $1 < \mathrm{Re}_p < 500$, $C_f^{(r)}$ is given by the formula [8]

$$C_f^{(r)} = \frac{48}{\mathrm{Re}_p}\left(1 - \frac{2.2}{\sqrt{\mathrm{Re}_p}}\right) \approx 48\mathrm{Re}_p^{-1}. \qquad (3)$$

Since the concentration and size of the particles are sufficiently small, the motion of the melt under the action of particles is ignored. In addition, we neglect the gravity forces in comparison to the other forces acting in the system. Using formulas (2) and (3), Eq. (1) can be written in the following form:

$$\frac{dv_p}{dt} = \frac{(\rho_p - \rho_L)v_\varphi^2}{\rho_p r} + \frac{9\rho_L \nu (v_L - v_p)}{\rho_p r_p^2}. \qquad (4)$$

Below, we will consider the radial motion of a microparticle in a stationary regime, that is, for the time $t \gg \tau_\varphi$, where τ_φ is a characteristic time for the particle motion in the azimuthal direction. Assuming $v_\varphi \cong v_m$ in Eq. (4), we obtain

$$\frac{d}{dt}\left(\frac{v_p}{v_m}\right) = -\frac{1}{\tau_s}\left(\frac{v_p - v_L}{v_m}\right) + \frac{1}{\tau_m}, \qquad (5)$$

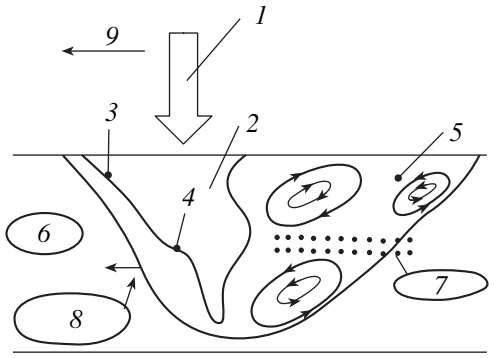

A schematic diagram illustrating the geometry of a vapor–gas channel and a melt bath formed under the action of scanning laser beam: (*1*) laser beam; (*2*) vapor–gas channel; (*3*) frontal melt layer; (*4*) step; (*5*) melt; (*6*) sold phase; (*7*) a layer of particles; (*8*) directed front motion; (*9*) laser beam scan direction.

where $\tau_s = r_p^2 \rho_p / 9\nu\rho_L$ is the characteristic time of the viscous relaxation of particles and $\tau_m^{-1} = (\rho_p - \rho_L)r_w / v_m \rho_p$.

For $v_L = \mathrm{const}$, Eq. (5) has the following solution:

$$\frac{v_p}{v_m} = \left(\frac{\tau_s}{\tau_m} + \frac{v_L}{v_m}\right)\left(1 - \exp\left(-\frac{t}{\tau_s}\right)\right).$$

In a stationary regime (for $t \gg \tau_s$), this yields

$$v_p^{(cm)} = v_m \frac{\tau_s}{\tau_m} + v_L \approx \frac{(\rho_p - \rho_L)r_p^2 v_m^2}{9\rho_L \nu r_w} + v_L. \qquad (6)$$

For the parameters $\rho_L = 8$ g/cm^3 (Fe), $\rho_p = 11$ g/cm^3 (Pb), $r_p = 3 \times 10^{-3}$ cm, $\nu = 3 \times 10^{-3}$ cm^2/s, $v_m = 10^2$ cm/s [3], and $r_w = 10^{-1}$ cm, the values of the characteristic times and the radial velocity are as follows: $\tau_s \cong 2 \times 10^{-5}$ s; $\tau_m \cong 10^{-3}$ s; $v_p^{(cm)} \cong 10$ cm/s.

Let h be the height of the melt bath. The characteristic vortex radius is $r_w \approx h/4$. For a sufficiently large laser beam scan velocity, the length of the melt bath exceeds the height. In this case, the characteristic geometry of the melt velocity field corresponds to two vortices, with the vortex velocity directions coinciding in the central part of the melted zone (see the figure). If the melt contains insoluble particles with dimensions $r_p \approx 10^{-3}$–10^{-2} cm, which are heavier than the matrix, their centrifugal velocity (for $h \sim 0.5$ cm) would amount to $v_p \cong 1$–10^2 cm/s.

If the heavy microparticles move toward the middle part of the melt bath (i.e., toward the vortex periphery) by a characteristic distance of $h/4$ during the solidification time r_f, the central zone will contain a solidified layer of the impurity. Light particles (in the case of two vortices with the bath height) will gather at a distance of $h/4$ from the melt bath top and bottom (along the vor-

tex center trajectory). A condition for the formation of such layers can be written in the following form:

$$v_p \tau_f > \frac{h}{4}. \quad (7)$$

The time of the melt solidification equals, on the order of magnitude, to $\tau_f \cong 2r_0^2/\chi$, where r_0 is the vapor–gas channel radius and χ is the thermal diffusivity of the melt.

In this case, condition (7) can be written as $(\rho_p/\rho_L - 1)(r_p r_0 v_m/n)^2(\chi\nu)^{-1} \geq 0.3$. Using this relationship for a typical system with $v_m \cong 10^2$ cm/s [3], $r_0 \cong 2 \times 10^{-2}$ cm, $\nu \cong 3 \times 10^{-3}$ cm^2/s, $\chi \cong 10^{-1}$ cm^2/s, and $h \cong 0.5$ cm, we obtain an estimate of the characteristic size r_p of microparticles that can participate in the formation of layers: $r_p \geq 6 \times 10^{-3}$ cm. Thus, microparticles with dimensions in the region of ~10^{-3}–10^{-2} cm may form layers of the corresponding insoluble impurity upon solidification of the melt formed by the scanning laser beam producing deep fusion of the processed heterogeneous material.

Now, let us consider the role of some ignored factors. In the above estimates, we neglected a change in the radial coordinate r of the microparticle during the motion, which was acceptable for the times $t \ll r/v_p \cong 10^{-2}$–$10^{-1}$ s since we believe that microparticles of the component B are not disintegrated under the action of the kinetic head $\pi r_p^2(\rho_L v_m^2/2)$ while moving relative to the liquid component A, the particle size correspond to the Weber number $\mathrm{We} = \rho_L v_m^2 r_p/\sigma < \mathrm{We}_{cr} \cong 12$ (where σ is the microparticle surface tension. $\sigma \cong 4 \times 10^2$ dyn/cm for Pb). This implies that the microparticle size cannot exceed $r_p = r_{p(cr)} \cong \sigma \mathrm{We}_{cr}/\rho_L v_m^2 \cong 5 \times 10^{-2}$ cm.

Equation (1) was written neglecting the gravity force $\Delta m g$ ($\Delta m = m(\rho_p - \rho_L)/\rho_L$, $m = 4\pi r_p^3 \rho_p/3$ is the particle mass) in comparison to the centrifugal force $\Delta m v_\varphi^2 r^{-1}$. Indeed, the ratio of the gravity and the centrifugal forces is $gr/v_\varphi^2 \cong 10^{-4} \ll 1$. For the motion in the azimuthal vortex direction in the case when the vortex velocity vector coincides in direction with the gravity force, the ratio of the gravity force to the kinetic head is $\sim(\rho_p - \rho_L)g\tau_\varphi/\rho_p v_m \cong 3 \times 10^{-4} \ll 1$.

If the density of the impurity B microparticles is smaller than that of the liquid component A (i.e., $\rho_p < \rho_L$), the light microparticles will float toward the vortex center (in contrast to the heavier particles with $\rho_p > \rho_L$, which would "sink" toward the vortex periphery).

Conclusion. Thus, we have considered a qualitative model describing the formation of layer structures of components of a heterogeneous material in a melt solidifying after the action of a high-power laser pulse producing deep fusion of the material. The model explains the formation of layers by the centrifugal recession or gathering of the impurity microparticles with dimensions ~10^{-4}–10^{-3} cm (heavier or lighter compared to the main liquid component). The centrifugal effect is manifested in the vortex flows developed in the melt with a velocity of ~10^2 cm/s under the action of hydrodynamic instabilities of a certain nature. In the case of a continuous laser irradiation, with a laser beam scanning over the material surface, the melt may feature nonstationary periodically repeated three-dimensional vortex flows explained by injection of the submerged melt flows from the front wall of a vapor–gas channel, related to the step of the melted material moving along the wall.

After solidification of the heterogeneous melt behind the moving vapor–gas channel, the layers of insoluble impurity in the form of bands perpendicular to the laser beam axis are fixed in the solidified zones. Such band structures were experimentally observed in some heterogeneous systems irradiated by high-power scanning laser beams, for example in Fe–(Cu–Pb), where the upper and lower layers represented virtually pure iron (phase A) and the middle layers contained a copper–lead alloy (phase B).

Acknowledgments. This study was supported by the Russian Foundation for Basic Research, project no. 00-02-17664.

REFERENCES

1. I. N. Shiganov, Vestn. Mosk. Gos. Tekh. Univ., No. 3, 25 (1998); Proc. SPIE **3688**, 211 (1999).
2. A. Matsunawa, N. Seto, M. Mizutani, and S. Katayama, in *Proceedings of the International Congress on Applications of Lasers and Electro-Optics, ICALEO'98, 1998* (Laser Inst. of America, Orlando, 1998), p. 151.
3. A. Matsunawa, N. Seto, J. Kim, *et al.*, Proc. SPIE **3888**, 34 (2000).
4. V. S. Golubev, Proc. SPIE **3888**, 244 (2000).
5. V. S. Golubev, Preprint No. 83, IPLIT RAN (1999).
6. G. Gaillibotte, D. Kechemair, and L. Sabatier, Proc. SPIE **1502**, 50 (1991).
7. F. Kh. Mirzoev, V. Ya. Panchenko, and L. A. Shelepin, Usp. Fiz. Nauk **166** (1), 3 (1996) [Phys. Usp. **39**, 1 (1996)].
8. V. V. Likhanskiĭ and A. I. Loboĭko, Kvantovaya Élektron. (Moscow) **30** (9), 827 (2000).

Translated by P. Pozdeev

Technical Physics Letters, Vol. 27, No. 10, 2001, pp. 881–882. Translated from Pis'ma v Zhurnal Tekhnicheskoĭ Fiziki, Vol. 27, No. 20, 2001, pp. 79–82.

The Geometric and Parametric Control of Gas Flow in a Gasdynamic Window

L. N. Orlikov and N. L. Orlikov

Tomsk State University of Control Systems and Radioelectronics, Tomsk, 634050 Russia

e-mail: ufo@muma.tusur.ru

Received May 24, 2001

Abstract—It is reported for the first time that the gas flow in a differentially pumped gasdynamic window can be deviated by varying a local profile of the output element or by changing local parameters of the gas. © *2001 MAIK "Nauka/Interperiodica".*

The extraction of low-energy (100 eV and below) electron beams through gasdynamic windows encounters the problem of minimizing the beam transport distance and the capacity of pumping facilities. This task was traditionally solved by using window elements of complicated shapes or by deviating the extracted beam from the aperture axis [1, 2]. Below, we consider alternative methods based on changing the profile of an output element from which the gas is supplied to the window and on varying the local flow temperature with the aid of an electric discharge. Using this approach, it is possible to deviate the gas flow from the output aperture of the electron source, thus minimizing both the beam transport length and the required pumping efficiency.

A schematic diagram of the gas flow pattern in a gasdynamic window and the output element section is presented in the figure. If the gas output element is cut at an angle, the gas flow Q expands on reaching the vacuum first at point a and eventually at point b. This gives rise to a pressure gradient across the flow direction, which deviates the gas flow from the axis (geometric control). The static pressure P_1 established between elements of the gasdynamic window is 5–6 times lower than the total flow head P^*. The gas pressure P_3 in the vicinity of point a outside the flow expansion zone is comparable with P_1. As a result, the pressure drop P_k/P_2 across the gasdynamic window, geometrically controlled by the distance between elements ($h > 2d$), is independent of the shape of element *2* and the efficiency of a pump evacuating the gas from the space between elements *1* and *2* sharply increases. The cut angle ϕ of the gas output element is determined as complementary to the limiting angle of deviation δ of the flow expanding into the vacuum [3]:

$$\varphi = \pi - \{[(k+1)/(k-1)]^{0.5} - 1\}\pi/2, \qquad (1)$$

where k is the gas adiabat exponent (for air with $k = 1.4$ and the limiting angle $\delta = 130°27'$, the cut angle is $\varphi = 49°33' \approx 50°$).

The flow can also be affected (parametric control) by changing the pressure P_k in front of the gasdynamic window or by a varying the local gas temperature in the flow at point a with the aid of a electric discharge initiated in the flow [4]. The discharge operation is accompanied by a thermobaric effect, whereby a change in the temperature gives rise to a pressure difference. The magnitude of the pressure difference across the flow (P_1/P_3) can be evaluated using the following relationship between parameters derived for a stationary thermal process in the gas flow [3]:

$$P_1/P_3 = 1 + k(\lambda^2 - 1)/(\lambda^2 + 1). \qquad (2)$$

Here, λ is the tabulated flow velocity coefficient [3] equal to the ratio of the flow velocity to the velocity of sound in the immobile gas flow (in air, $P_1/P_k = 1$ and $\lambda = 0$ corresponds to the immobile gas; $P_1/P_k = 0.528$ and $\lambda = 1$ corresponds the air flowing at a velocity of sound; $P_1/P_k = 0$ and $\lambda = 2.45$ corresponds to the theoretical limit of the flow velocity). In the known gasdynamic

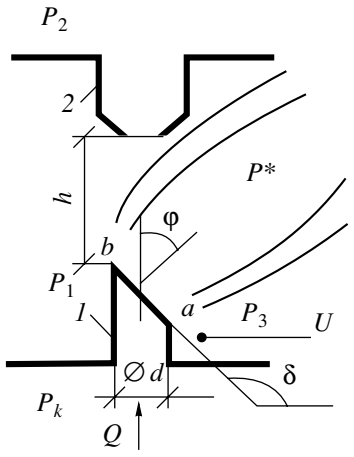

A schematic diagram of the gas flow in a gasdynamic window.

1063-7850/01/2710-0881$21.00 © 2001 MAIK "Nauka/Interperiodica"

window schemes, the pressure drop on element *1* does not exceed (for the energy considerations) two–three orders of magnitude. For the theoretically possible air flow velocity coefficient (not exceeding 2.45), the limiting value of the pressure drop determined from formula (2) is $P_1/P_3 \approx 2$.

An electric discharge initiated immediately at the output element *2* creates a zone of local change in the flow parameters, which is equivalent to modification of the geometric shape of the element. This decreases the influence of the shape of element *2* on the pressure drop across the gasdynamic window.

The possibility of the proposed geometric and parametric flow control was experimentally verified using a system [5] of the electron beam extraction from a three-channel electron source into the atmosphere. The output elements had the form of tubes with a beam transmit aperture diameter of 1 mm. The gas output element was cut at an angle of 50°. The gasdynamic window was pumped to a pressure of 10 kPa with a circular water-jet pump of the VVN-3 type; the electron source was pumped to 50 Pa with a VN-7 mechanical pump. Under these conditions, the gas flow deviation angle was 25° as measured on the aerosol trace pattern.

An electrode introduced into a region in the vicinity of point *a* was capable of initiating the electric discharge at a voltage of $U = 3000$ V (with a discharge current of up to 1 A), which allowed the pressure in the electron source to be reduced from 150 to 50 Pa. Owing to the gas flow deviation, the distance between the window elements can be made as small as twice the output tube diameter (for the same minimum pressure in the electron source). At lower pressures, the electric-discharge system of creating the pressure drop is preferred over the system employing gasdynamic effects. The total power of the pumping facilities necessary for the system operation decreases from 5 to 1.2 kW per mm^2 of the output cross section area. In gasdynamic windows with restricted beam transport length, the method of gas flow deviation offers more promising results as compared to the beam deviation.

REFERENCES

1. B. W. Schumacher, in *Transactions of the 8th National Vacuum Symposium and 2nd International Congress on Vacuum Science and Technology, 1961* (Pergamon, New York, 1962), p. 1192.
2. L. N. Orlikov, Prib. Tekh. Éksp. **1**, 137 (2001).
3. G. N. Abramovich, *Applied Gas Dynamics* (Nauka, Moscow, 1976).
4. L. N. Orlikov, in *Proceedings of the 4th International Scientific and Practical Conference "Natural and Intellectual Resources of Siberia, SIBRESURS-98, Barnaul, 1998* (Tomsk. Gos. Univ. Sistem Upravleniya i Radioélektroniki, Tomsk, 1998), p. 227.
5. Yu. I. Bychkov, Yu. D. Korolev, G. A. Mesyats, *et al.*, Pis'ma Zh. Tekh. Fiz. **4** (9), 515 (1978) [Sov. Tech. Phys. Lett. **4**, 206 (1978)].

Translated by P. Pozdeev

Technical Physics Letters, Vol. 27, No. 10, 2001, pp. 883–885. Translated from Pis'ma v Zhurnal Tekhnicheskoĭ Fiziki, Vol. 27, No. 20, 2001, pp. 83–88.

Autooscillations Generated during a Diaphragm Discharge in an Electrolyte

V. S. Teslenko, A. P. Drozhzhin, and A. M. Kartashov

Lavrentiev Institute of Hydrodynamics, Siberian Division, Russian Academy of Sciences, Novosibirsk, Russia

e-mail: teslenko@hydro.nsc.ru

Received May 10, 2001

Abstract—The electrohydrodynamic autooscillations of a vapor–gas bubble and electric current accompanying a diaphragm electric discharge in an electrolyte were studied for a capacitor voltage from 200 to 900 V and a diaphragm hole diameter of 0.3–0.9 mm. The upper region of stable relaxation current oscillations was determined. *© 2001 MAIK "Nauka/Interperiodica".*

Up to the present, only a few papers reported on the properties of a diaphragm electric discharge. For example, the investigations described in [1, 2] aimed at obtaining a dense plasma in a condensed medium at a storage bank energy of up to 7.5 kJ and a capacitor voltage up to 10 kV. Our study has pursued different purposes: exciting stable autooscillations of a vapor–gas bubble in an electric circuit by means of a diaphragm electric discharge in an electrolyte, finding the region of stable relaxation current oscillations, and determining the frequency characteristics of the autooscillating system.

Below, we present the results on the generation of autooscillations of the relaxation current and the vapor-gas bubble size in diaphragms with a hole diameter of d = 0.3–0.9 mm. The diaphragms, made of a Lavsan (Dacron) film with a thickness of h = 50 μm, were mounted vertically. The electrolyte was an aqueous sodium chloride solution with a concentration of k = 1–5 wt %. Two flat stainless steel electrodes were placed in different compartments of a cell filled with the electrolyte and separated by the polymeric diaphragm with a hole. The distance from electrodes to the hole in the diaphragm was $H > 10d$. The electrode area exceeded the hole area by more than one order of magnitude. The experiments were performed with a capacitive energy storage unit composed of replaceable capacitors (C = 2–100 μF) and a contact current commutator with an electromagnetic drive system. The current in a sample circuit was measured with the aid of a low-inductance Parker shunt (R = 0.148 Ω). The hydrodynamic processes were monitored by shadowing techniques using high-speed photoregistration systems of the SFR and ZhFR types.

Experimental results. The current oscillograms presented in Fig. 1 illustrate the dynamics of the transient process development into the relaxation current oscillations for various initial capacitor voltages in the range U = 100–400 V and the diaphragm with a hole diameter of d = 0.5 mm. As can be seen from these patterns, the development of the regime of stable autooscillations has a threshold character with respect to voltage.

Figure 2 shows, on a common time scale, an oscillogram of the current variation $I(t)$ and a pattern of the bubble boundary pulsations $D(t)$ (a photoregistrogram processed and plotted in a dimensionless form of D/d for d = 0.5 mm) observed for U = 500 V and an electrolyte concentration of k = 1 wt %. Both visual observations and the photo and video records showed that the initial stage of the electrohydrodynamic process corresponds to the corona discharge development on the perimeter of the diaphragm hole. The initial bubble has a toroidal shape. During the first pulsation, the toroidal bubble transforms into a spherical one. Subsequent radial pulsations of the spherical bubble proceed relative to the center of the diaphragm. The bubble pulsation kinetics is close to the Rayleigh law. As the bubble size grows to approach $D/d \approx 2.4$, the current halts so that the bubble performs the function of a current interrupter. When the bubble collapses to D/d = 1.2–1.4, the current circuit is closed again. This cyclic process repeats as long as the stored energy is consumed. Figure 1d clearly displays the dynamics of current commutation and shows variation of the current pulse duration and repetition period accompanying a decrease in the stored energy.

As can be seen from Fig. 2, the minimum (maximum) bubble size corresponds to the maximum (minimum) current. The minimum bubble size is always greater than the hole diameter. The energy lost during the bubble pulsation is compensated by the electric discharge initiated in the bubble along the hole perimeter at $D/d \approx$ 1.2–1.4.

The results of these experiments showed that the period of relaxation current oscillations in the stable regime depends but weakly on the electrolyte concentration and capacitor voltage. The most pronounced and

1063-7850/01/2710-0883$21.00

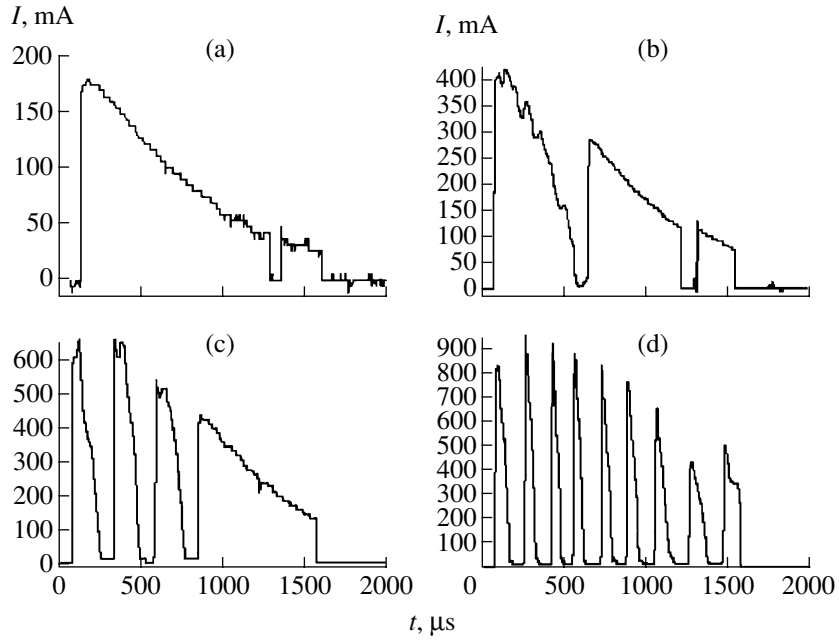

Fig. 1. The dynamics of a transient (threshold) process development into a stable regime of the relaxation current oscillations in a system with the diaphragm hole diameter $d = 0.5$ mm and a capacitor of $C = 2$ μF charged to various initial voltages $U = 100$ (a); 200 (b); 300 (c); 400 V (d).

important dependence of the self-oscillation process on the system parameters is the relationship between the period T of the relaxation current oscillations and the diaphragm hole diameter d, which can be approximately described as $T \approx 390d$ μs (with T in microseconds and d in millimeters).

In the range of parameters (d and U) studied, the current pulses are unipolar, exhibit a steep leading front, and decay within a time of $t \sim (0.2–0.5)T$. The current pulse decay dynamics depends on the capacitor voltage (Fig. 1).

The experiments showed that a stable regime of autooscillations is attained in a limited region of the capacitor voltages U and diaphragm hole diameters d. We determined the upper limiting values of the hole diameter and the capacitor voltage for which the autooscillations may take place. A minimum voltage at which the autooscillations begin to develop are referred to as the lower "threshold," while a voltage at which the instabilities are developed is called the upper "boundary."

Figure 3 shows a diagram of the upper domain of existence of the electrohydrodynamic autooscillations.

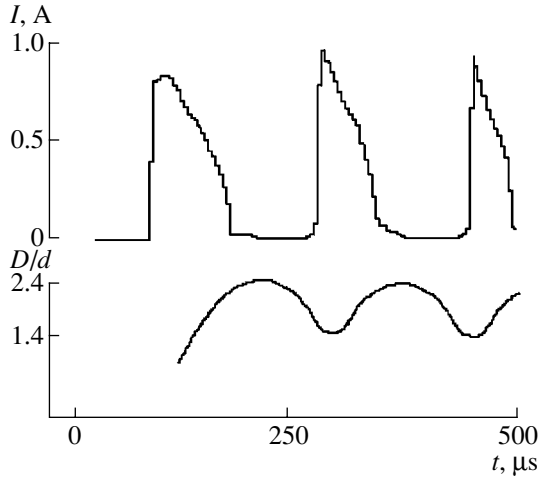

Fig. 2. Synchronous registration of the current I and the bubble size (presented in the dimensionless form of D/d) pulsations in a common time scale for a system with $d = 0.5$ mm, $U = 500$ V, and $k = 1$ wt %.

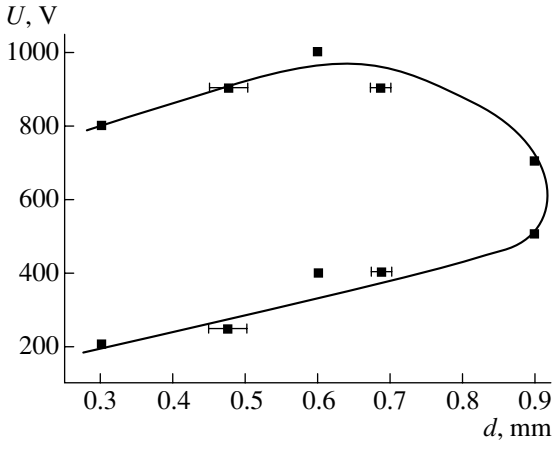

Fig. 3. A diagram of the domain of existence of the electrohydrodynamic autooscillations. No stable self-oscillation regime is possible in the right-hand region outside the domain depicted by the solid curve.

No stable autooscillations take place in the right-hand region outside the domain. Increasing the voltage leads to instability of the self-oscillation processes, a sharp increase in the current, a corona discharge development over the whole diaphragm cross section, and the bubble size growth up to $D > 3d$.

The breakage of a stable self-oscillation process may be related to several factors such as the bubble center displacement off the diaphragm center, instability development on the bubble surface during collapse from $D > 3$ mm, etc. The dynamics of processes developed in a diaphragm discharge at still higher voltages (i.e., for $D > 5d$) is described elsewhere [1, 2].

Conclusion. An analysis of the results of our experiments leads to the following conclusions:

(i) Using the diaphragm discharge in an electrolyte, it is possible to generate autooscillations of the current and the vapor-gas bubble. A nonlinear element in the electric chain is a cell with the diaphragm, which plays the role of a nonlinear resistor in the circuit [3]. The nonlinear resistance depends on the current density in the diaphragm hole and the minimum and maximum bubble size.

(ii) The experiments showed that the current is switched by the oscillating bubble. The current is interrupted when the bubble grows to a maximum size of $D = 2.4d$. Upon the hydrodynamic collapse to $D = (1.2–1.4)d$, the current is switched on and the corona discharge initiated over the perimeter of the diaphragm hole. This is accompanied by the supply of an additional electric energy providing for the continued pulsation of the bubble. Thus, the electrohydrodynamic current commutation with the cyclic energy supply and loss in the diaphragm hole is repeated in the form of a self-sustained oscillation process.

(iii) Important parameters of the self-sustained oscillation process in the system under consideration are the period (T) of pulsations of the bubble and current involving the energy conversion from one to another type in the form of electromagnetic radiation, light, heat, hydrodynamic pulses, and acoustic waves. The experimental results obtained for diaphragms with the hole diameter ranging from 0.3 to 0.9 mm showed that the period of pulsations obeys the relationship $T \sim Kd$ with $K = 380$ μs/mm. The current pulses are unipolar, exhibit a steep leading front, and decay within a time of $t \sim (0.2–0.5)T$.

(iv) The process of autooscillations in the system studied can be implemented in acoustics, hydrodynamics, electrodynamics, biophysics, and in a number of other applications related to modeling and development of the self-oscillating systems employing phase transitions in liquid media.

Acknowledgments. The authors are grateful to V. V. Mitrofanov and A. P. Ershov for fruitful discussions.

This study was supported by the Russian Foundation for Basic Research, project nos. 00-02-17992 and 01-02-06443.

REFERENCES

1. É. M. Drobyshevskiĭ, Yu. A. Dunaev, and S. I. Rozov, Zh. Tekh. Fiz. **43** (6), 1217 (1973) [Sov. Phys. Tech. Phys. **18**, 772 (1973)].
2. B. I. Reznikov, B. G. Zhukov, and F. V. Sosnovskiĭ, Zh. Tekh. Fiz. **47** (12), 2487 (1977) [Sov. Phys. Tech. Phys. **22**, 1443 (1977)].
3. A. A. Andronov, A. A. Vitt, and S. É. Khaikin, *Theory of Oscillators* (Fizmatgiz, Moscow, 1959; Pergamon, Oxford, 1966).

Translated by P. Pozdeev

Technical Physics Letters, Vol. 27, No. 10, 2001, pp. 886–888. Translated from Pis'ma v Zhurnal Tekhnicheskoĭ Fiziki, Vol. 27, No. 20, 2001, pp. 89–94.

The Effect of an Electric Field on the Surface Energy Anisotropy in Alkali Metal Alloys

V. Z. Kanchukoev, A. Z. Kashezhev, A. Kh. Mambetov, and V. A. Sozaev

Kabardino-Balkarian State University, Nal'chik, Kabardino-Balkaria, Russia

e-mail: exp@kbsu.ru

Received April 3, 2001

Abstract—The effect of an electric field on the surface energy anisotropy in alloys is considered for the first time with an allowance for the surface segregation. © *2001 MAIK "Nauka/Interperiodica".*

The effect of an electric field on the surface properties of pure metals was extensively studied [1–4]. The influence of this factor on the surface energy and surface segregation in metal alloys is known to a lesser extent [5, 6]. It was demonstrated that a significant change in the surface properties such as the segregation of components, electron density distribution at the interphase boundary, surface energy, etc., takes place in the fields of considerable strength $E \sim 10^8$ V/cm.

In this paper, we will consider, within the framework of the electron density functional method, the effect of an electric field on the surface energy anisotropy in alkali metal alloys of the A_xB_{1-x} type. The alloy is modeled in the virtual crystal approximation [5, 7]. In this model, the surface segregation is taken into account in terms of the function characterizing a stepwise change in the charge density at the alloy–vacuum interface:

$$n_+(z) = n\theta(-z) + n_s\theta(z)\theta(D-z), \qquad (1)$$

where $\theta(z)$ is the Heaviside step function; $n = [x\Omega_A + (1-x)\Omega_B]^{-1}$ is the average positive charge density in the bulk of the alloy; Ω_A and Ω_B are the atomic volumes of the alloy components A and B, respectively; $n_s = [x_s\Omega_A + (1-x_s)\Omega_B]^{-1}$ is the average positive charge density in the surface (segregated) layer; D is the segregated layer thickness; and x and x_s are the concentrations of component A in the bulk and in the surface layer, respectively. Both the composition (x_s) and charging (n_s) of the segregated layer depend on the electric field strength E ($E > 0$ for the field directed along outward normal to the alloy surface).

The electron density distribution will be described in terms of a two-parametric trial function, which is preferred to single-parametric functions [1] for more adequately describing the symmetry violation in the electron density distribution under the action of the electric field inside and outside the alloy:

$$n(z) = n\left[1 - \frac{\beta}{\alpha+\beta}\exp(\alpha(z-Z_G))\right]\theta(Z_G - z) + n\frac{\alpha}{\alpha+\beta}\exp[\beta(Z_G - z)]\theta(z - Z_G). \qquad (2)$$

Here, α and β are the variation parameters determined from the condition of minimum surface energy $\sigma = \min_{\alpha,\beta,n_s}(\alpha, \beta, n_s)$; z is the coordinate along the normal to the sample surface, measured from the inner boundary of the segregated layer; and Z_G is the coordinate of the Gibbs interface determined from the condition of electroneutrality of the system

$$Z_G = 1/\alpha - 1/\beta + (n_s/n)D \pm E/4\pi n. \qquad (3)$$

In formula (3), the variation parameters α and β depend on the field strength E and characterize the reciprocal lengths of the "tail" of the electron density distribution inside and outside the alloy. The last term in formula (3) reflects the fact that the center-of-gravity of the electron density distribution shifts by $z_0 = \pm E/4\pi n$ under the action of the applied electric field. The electrostatic potential $\varphi(z)$on the alloy–vacuum interface is determined from the Poisson equation

$$\Delta\varphi(z) = -4\pi[n_-(z) - n_+(z)]. \qquad (4)$$

Once the distribution of $n_+(z)$, $n_-(z)$, and $\varphi(z)$ at the interface is known, the total surface energy can be calculated by the formula

$$\sigma = \sigma_j + \delta\sigma_{ps} + \delta\sigma_{cl}. \qquad (5)$$

1063-7850/01/2710-0886$21.00

Here, the first term

$$\sigma_j = \int_{-\infty}^{\infty} \{w[n_-(z)] - w[n_+(z)]\}dz + \frac{1}{2}\int_{-\infty}^{\infty} \varphi(z)[n_-(z) - n_+(z)]dz \quad (6)$$

is the homogeneous background contribution, $w[n(z)]$ being the kinetic energy density of a noninteracting gas (with a correction for the field inhomogeneity in the Weizsäcker–Kirzhnits approximation) and the exchange–correlation interaction energy (with a nonlocal correction in the Geldart–Rasolt approximation). The second term ($\delta\sigma_{ps}$) in Eq. (5) is a correction to the "jelly" model due to the electron–electron interaction, and the third term ($\delta\sigma_{cl}$) is the surface Madelung energy related to the ion–ion interaction [7].

The second term in formula (6) characterizes the energy of electrostatic interaction $\delta\sigma_{es}(E)$ of the electron gas with the "jelly" charge and the positive charge of segregated layer. An expression for calculating this energy can be presented as a sum of two terms:

$$\sigma_{es}(E) = (1/2)\int \varphi(z)[n_-(z) - n_+(z)]dz = \sigma^0_{es}(\alpha, \beta) + \sigma^E_{es}(\alpha, \beta, E), \quad (7)$$

where $\sigma^0_{es}(\alpha, \beta)$ is determined by the formulas derived for alloys in the absence of the field [7], involving the variation parameters $\alpha(E)$ and $\beta(E)$. For $Z_G > D$, the $\sigma^E_{es}(\alpha, \beta, E)$ value is described by the expression

$$\sigma^E_{es} = (EDn_s/n + E^2/8\pi n) \times (n_sD/2 - nZ_G/2 + n\beta/(2\alpha(\alpha + \beta))) + ED^2(n - n_s)/2 + nE(Z_G^2 - D^2)/4 - (En/2\alpha^2)[Z_G\alpha - 1 + \exp(\alpha(D - Z_G))]. \quad (8)$$

All other contributions to the surface energy entering into (5) and (6) are calculated using the relationships analogous to those derived for $E = 0$ [7], with the variation parameters $\alpha(E)$ and $\beta(E)$ and the positive charge density $n_s(E)$ in the segregated layer determined as functions of the applied field E.

Thus, we describe the influence of an applied field on the interfacial characteristics with an allowance for the following effects: (i) displacement of the center-of-gravity of the induced charge, (ii) a change in the length of the electron density distribution "tail" inside and outside the alloy, and (iii) a change in the positive charge density n_s in the segregated layer (and, hence, in the thickness D of this layer).

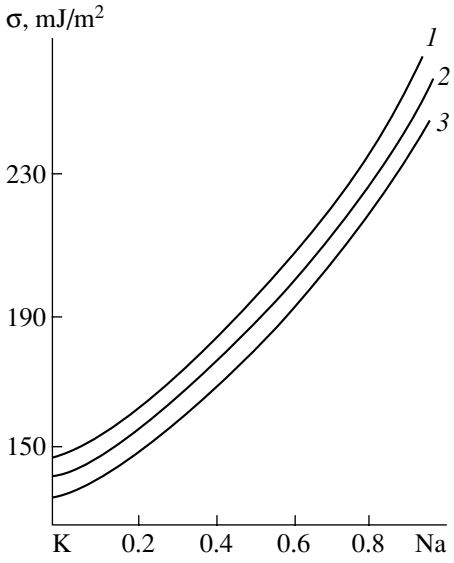

Fig. 1. The plots of σ versus atomic fraction of Na in Na– K alloys calculated for the field strength $E = -2.6 \times 10^7$ (*1*), 0 (*2*), 2.6×10^7 V/cm (*3*).

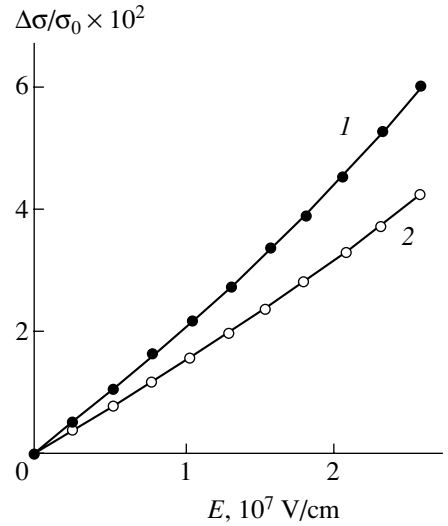

Fig. 2. Plots of a relative change in the surface energy versus field strength ($E > 0$) for (*1*) (100) and (*2*) (110) crystal faces of the $Na_{0.5}K_{0.5}$ alloy.

The total surface energy $\sigma(E)$ was calculated for alkali metal alloys of the Na–K system. The results of these calculations are presented in Figs. 1 and 2. Figure 1 shows the plots of σ versus the alloy concentration (atomic fraction of Na) for the (110) crystal face in the absence of an applied field ($E = 0$) and for a field strength of $\pm 2.6 \times 10^7$ V/cm. As can be seen from these data, the negative fields increase the surface energy while the positive fields decrease this energy equally in the entire concentration range.

Figure 2 shows a relative change in the surface energy as a function of the field strength (for $E > 0$) cal-

culated for the alloy crystal faces (100) and (110). These plots indicate that a difference in the field effect on the surface energy of the two faces increases with the field strength. This is evidence that the electric field influences anisotropy in the surface energy of crystal faces in metal alloys.

REFERENCES

1. V. F. Ukhov, R. M. Kobeleva, G. V. Dedkov, and A. I. Temrokov, *Electron-Statistical Theory of Metals and Ionic Crystals* (Nauka, Moscow, 1982).
2. A. Kiejna, Solid State Commun. **50** (4), 349 (1984).
3. H. J. Kreuzer, Surf. Sci. **246**, 336 (1991).
4. A. M. Shabalin, Prikl. Mekh. Tekh. Fiz., No. 1, 15 (1992).
5. R. M. Digilov and V. A. Sozaev, Poverkhnost', No. 10, 138 (1990).
6. I. N. Aliev and P. P. Poluéktov, Pis'ma Zh. Tekh. Fiz. **18** (7), 7 (1992) [Sov. Tech. Phys. Lett. **18**, 209 (1992)].
7. R. M. Digilov and V. A. Sozaev, Poverkhnost', No. 7, 42 (1988).

Translated by P. Pozdeev